Battery States Monitoring and its Application in Energy Optimization of Hybrid Electric Vehicles

Politecnico di Torino

ScuDo
Scuola di Dottorato ~ Doctoral School
WHAT YOU ARE, TAKES YOU FAR

Doctoral Dissertation
Doctoral Program in Energy Engineering (34th Cycle)

Battery States Monitoring and its Application in Energy Optimization of Hybrid Electric Vehicles

By

Ezemobi Ethelbert

******

Supervisor(s):
Prof. Andrea Tonoli

Doctoral Examination Committee:
Prof. A.B. , Referee, University of….
Prof. C.D. , Referee, University of…
Prof. E.F. , Referee, University of….
Prof. G.H. , Referee, University of…
Prof. I.J. , Referee, University of….

Politecnico di Torino
2022

Declaration

I hereby declare that the contents and organization of this dissertation constitute my original work and do not compromise in any way the rights of third parties, including those relating to the security of personal data.

Ezemobi Ethelbert
2022

* This dissertation is presented in partial fulfilment of the requirements for a **Ph.D. degree** in the Graduate School of Politecnico di Torino (ScuDo).

Dedication

I dedicate this work to God by whose grace this work is realised.

Acknowledgement

This work communicates the willingness of the stakeholders to invest in solutions to the pressing global needs and their commitment to realising impactful and sustainable projects. Optimum credits go to my supervisor, Prof. Andrea Tonoli, Politecnico di Torino, Italy for his tenacity and unwavering support in realizing this piece of work. The quality of this work may be hard to realise without the support from his wealth of experience and his adamant to accept but the best. A special appreciation is reserved for Prof. Amir Khajepour, University of Waterloo, Canada for his resourceful supervision and for extending to us his platform for international research through the exchange mobility program.

The experimental validation of the algorithms reported in this work was possible with the support of Mario Silvagni who played a major role in realizing the test bench used for experimental data collection. This contribution is well appreciated. I also acknowledge the host of reviewers, especially, Prof. Ehsan Hashemi and Prof. Eshkabilov Sulaymon. Their insightful feedback helped to enhance the structure and completeness of this work, and also minimise error.

The strength of teamwork is never underestimated and I acknowledge the team of the Interdepartmental Laboratory for Mechatronics (LIM) and the mechatronics team at the University of Waterloo. Many thanks to Sanjar Ruzimov, Luis Miguel Castellanos and Ahmad Mozaffari for the useful ideas and support.

Finally, special gratitude goes to my family and friends. Thank you for letting me see myself through you and for subconsciously keeping me accountable.

Abstract

The hybrid electric vehicle aims to minimise energy consumption and CO_2 emission. This goal should be achieved without compromising battery operating limits to avoid the risk of thermal runaway and to minimise ageing. Accurate state of charge (SOC) estimation plays a crucial role in reducing this risk and in decelerating battery ageing. A model-based SOC estimator is designed with a sigma point Kalman filter (SPKF) and experimentally validated under dynamic load conditions with an estimation root means square error (RMSE) of 2.2%.

The state of health (SOH) of the battery is monitored at regular intervals to keep track of the battery health status and to improve SOC estimation accuracy across the battery cycle life. As a starting point, SOH estimation is experimentally analysed under constant load conditions using the parallel layer extreme learning machine (PL-ELM) at room temperature. This solution demonstrates an improved generalisation of SOH estimation for the set of cells in a battery pack. Optimum RMSE of 0.064% to 0.473%, and the mean absolute error of 0.034% to 0.355% are verified. The algorithm was tested on a Texas F28379D microcontroller unit (MCU) board with an average execution speed of 93 µs in real-time, and 0.9305% CPU occupation.

Furthermore, SOH estimation is analysed under dynamic load conditions using the ANN-based classifier at room temperature. The classifier is validated experimentally under dynamic varying load, constant load, and step load conditions. The model accuracies for validation data are 96.2%, 96.6%, and 93.8% for the respective load conditions. It is further demonstrated that the model can be applied to multiple cell types of similar specifications with an accuracy of about 96.7%. The classifier was tested on a Texas F28379D microcontroller unit board. The result shows that an average real-time execution speed of 8.34 µs is possible with a negligible memory occupation.

Finally, to achieve the HEV goal of minimising energy consumption and CO_2 emission, an electro-thermal model of a lithium-ion battery is developed for energy storage and for defining the battery operating constraints. Energy optimization is performed in presence of these constraints for P2 HEVs using an adaptive model predictive control (MPC) strategy. The simulation results of the HEV SUV (Mazda CX9 2016) demonstrate that, by applying thermal constraints, energy consumption for a 0.9 kWh battery capacity can be reduced by 11.3% relative to the conventional vehicle. However, by increasing the battery capacity to 1.5 kWh (14s10p battery configuration), it is possible to reduce the energy consumption by 15.7%. Additional benefits associated with the predictive capability of MPC are reported in terms of thermal improvement.

Contents

List of Figures

List of Tables

Chapter 1. Introduction

The main design goal of hybrid electric vehicles (HEVs) is to minimise energy consumption and CO_2 emission. This has to be achieved without compromising the battery life and avoiding the risk of thermal runaway. The choice of lithium-ion batteries for application in HEVs is mainly influenced by the high energy density per weight. In addition, its large number of charge/discharge cycles, and reduced memory effect enhance this choice [1]. However, ageing affects the lithium-ion battery's operational life and the amount of energy that it can deliver. The battery capacity of HEV is often in the range of 0.5 to 2 kWh [2]. Considering such low capacity, ageing is accelerated by the high peak current and the consequent high operating temperature that is associated with the HEV. Monitoring the state of health (SOH) and the state of charge (SOC) of the battery is essential to keep track of the battery ageing status, and to avoid the risk of thermal runaway. Therefore, energy optimization in HEVs should be performed, applying the necessary constraints.

Energy management in HEV powertrain requires accurate measurement of the battery SOC. Also, accurate SOC measurement is essential for proper energy balancing and reliability in energy distribution [3,4]. Many authors have demonstrated alternative procedures for SOC estimation employing direct method, traditional method, fuzzy logic, model-based and data-based approaches. Reviews of such procedures are given in [5,6]. The direct method takes advantage of the relationship that exists between the SOC and measured variables such as OCV, terminal voltage and impedance under different conditions. The traditional approaches include; ampere-hour integration or charge counting, open-circuit voltage (OCV) and internal resistance. The charge counting method performs poorly with inaccurate initialization. The OCV measurement is non-trivial and time-consuming. The internal resistance approach has limited application since internal resistance has low sensitivity at high SOC for many battery technologies and almost no sensitivity for some battery technologies. More information about these traditional approaches can be found in [7].

The model-based approaches include the use of filters and observers while the data-based approaches are dominated by the application of artificial intelligence for SOC estimation. The artificial intelligence approach is often limited by the training data size and quality. On the other hand, filtering and observer methods are limited by the accuracy of the base model. Also, the nonlinearity of SOC for different operating conditions increases the problem complexity. These issues can be

minimised using nonlinear filters that are equipped with feedback mechanisms for adaptation. The extended Kalman filter (EKF) is the most widely used nonlinear Kalman filter. This filter however has some flaws that limit its performance. The primary issue is how the EKF propagates the mean and covariance of a random vector through a static nonlinear function to estimate the mean and covariance of the output random vector. This flaw is further explained in [8]. Other limitations associated with the use of EKF are reported in [9,10]. Using the SPKF, the analytic linearization of the EKF is replaced by an efficient empirical or statistical linearization using a small number of function evaluations [11,12]. Such an approach eliminates the need to compute derivatives, hence the original function does not need to be differentiable. Better covariance approximations are achievable with SPKF with comparable computation complexity.

One major challenge encountered in SOC estimation is the limitation imposed by battery ageing. The adaptation ability of the SPKF is also limited by this effect. As a solution, SOH is estimated and used as a correction factor for SOC enhancement. In [13], a method is demonstrated for correcting the SOC based on combined SOC and SOH estimation using the neural network backpropagation algorithm. The performance obtainable with this method is as good as the quality and size of the data used in the training.

Regarding the SOH estimation, data-based approaches are being adopted more and more. Support Vector Regression (SVR) in [14] is used to estimate the battery SOH based on equivalent internal resistance (EIR). In [15], an AC impedance measurement is applied with fuzzy logic data analysis for the online estimation of SOH. The authors of [16] demonstrate a data-based estimation of SOH by fusion of an open circuit voltage model with a noise-free incremental capacity curve. Estimation of SOH with a multilayer perceptron algorithm is investigated in [17]. Training some of these algorithms require feature extraction from the training dataset. Useful features for SOH estimation must show some relevant correlation with battery ageing. Many algorithms exist in the literature for feature extraction. In [18], the authors demonstrate that partial constant-voltage capacity information shows a good correlation with SOH. In [19], SOH is characterised using the importance sampling (IS) strategy. The drawback is that it requires the battery charges or discharges to be sufficient for the feature variables to be extracted. ICA [20–22] and differential voltage analysis (DVA) are other common strategies, but their sensitivity to noise limits their application [23]. Alternative feature extraction is demonstrated in [24], where the relative battery internal resistance and voltage are used as features in a time-series momentum backpropagation neural network.

The production process of the lithium-ion battery is not fully mature. This results in a cell-to-cell variation of the parameters of the cells within a battery pack [25]. This variation influences the pattern of ageing of each cell. A SOH estimation model should accurately predict the SOH of the cells in the battery pack over the range of this variation. However, it is often the case that many trained SOH

prediction models experience deviation or drift when applied to the unobserved cell of similar specification. Given this variation, some authors adopt complex transfer learning approaches [19] with domain adaptation [26] to share knowledge across the distribution of the observed cells and the unobserved cells. Also, a less complex model based on ICA is proposed by [27] for enhancing generalization across cells of similar specifications. The high prediction accuracy and learning speed of PL-ELM make it an elegant alternative for applications where computational resources are a constraint.

SOH estimation under constant conditions is a good starting point as will be seen with PL-ELM. However, it has very limited applications in HEV. Many authors have demonstrated several alternative strategies for SOH estimation. However, only a few have attempted to analyse SOH estimation under dynamic load conditions that are obtainable in real-life practice. One reason for this is the enormous time required for battery ageing, especially under such conditions. Many authors have proposed time series regression approach in the literature [28–30]. The authors of [31] estimated the SOH under dynamic load conditions with a time-series independent recursive neural network model. The major problem with the time series approach is the fact that it is almost impracticable to keep track of the time history of the entire ageing process. The performance of time series models is hindered by time discontinuity that may result from the loss of data points. A classifier model is a viable option to minimise time dependency and avoid the need for continuous initialisation. Some methods for estimating the SOH of lithium-ion cells by classification are presented in [13,32]. To demonstrate the SOH estimation using a classification approach under dynamic load conditions, the classifiers reported in [13,32] are trained with a synthetic battery dataset in the discharge phase. Although the classifiers used in [13,32] demonstrate the potential for real-life application, the model has been validated under dynamic load conditions only in the discharge phase.

The aggressive dynamic operating load conditions of the HEVs expose the batteries to the risk of thermal runaway. To reduce this risk while minimising energy consumption, the energy management strategy (EMS) has to implement constraints to respect battery operating conditions such as the current request, voltage and temperature. To apply these constraints and to understand the impact of temperature on energy minimisation of HEV, an electro-thermal model of the battery pack is needed. Barcellona and Piegari propose a model that can predict the thermal behaviour of a pouch lithium-ion battery based on its current input and ambient conditions [33]. The model only takes the effect of the OCV and internal resistance into account. The resistive-capacitive (RC) parallel branches are not

included in the model of the battery considering that the thermal time constant greatly outweighs the electrical one. Such approximation simplifies the model with a compromise of increases in the model uncertainty. Madani et al. in [34] review the determination of thermal parameters of a single cell, such as internal resistance, specific heat capacity, entropic heat coefficient, and thermal conductivity. These parameters are then used for the design of a suitable thermal management system. A lumped-parameter thermal model of a cylindrical LiFePO4/graphite lithium-ion battery is developed in [35] to compute the internal temperature.

One way to prevent the risk of thermal runaway is to incorporate an adequate cooling mechanism in the battery thermal management system. Many of the electro-thermal models in the literature are designed for active cooling. The common active cooling medium includes liquid cooling, air cooling and the use of refrigerant. Passive cooling, on the other hand, includes phase change material (PCM) and heat pipe techniques. Some cooling strategies are reviewed and compared in [36,37]. On the basis of complexity and cost, these cooling systems are however not justified for 48 V HEV applications as in the current work. A simple passive cooling that dissipates heat from the battery surface by natural convection is assumed.

Various EMS strategies have been explored by researchers and they are generally grouped into rule-based and optimization strategies [38–41]. Rule-based strategies decide the operation modes and energy distribution scheme of power sources according to the characteristics of each source component [42]. Rule-based controls can be designed based on deterministic strategies [43] or according to fuzzy logic that requires expert knowledge [44]. Such control algorithms can ensure stability, robustness and computational efficiency with low memory consumption. However, the complex powertrain structure of the HEVs and inadequate knowledge of the driving information leads to sub-optimum results.

Optimization-based strategies can minimise CO_2 emission or energy consumption within a defined time horizon while respecting the system constraints. A local time horizon optimisation determines the optimum energy distribution for minimising fuel consumption instantaneously or within a short time horizon [45]. Energy consumption minimisation strategy (ECMS) [46] is one of the approaches for local energy optimisation. At each time step, ECMS evaluates the instantaneous cost function as a sum of the fuel consumption and the equivalent fuel cost of electric energy [47,48]. The ECMS is causal and offers a fast computation. However, the results are not globally optimum [49] since the optimization is non-predictively solved at each time instant [4,50,51]. Tuning the ECMS can be a complex task since the weighting parameters are determined heuristically. The

ECMS strategy can be applied online as a closed-loop controller. However, the decisions are non-predictive, and the plant model dynamics are not fully exploited.

When the entire driving conditions represented by a drive cycle are known a priori, the energy management can be treated as an optimal control problem and solved by global optimization strategies. Some strategies for global optimisation adopted in the literature include dynamic programming (DP) [41,52], Pontryagin's minimum principle (PMP) [53] and quadratic programming [54]. These approaches are sufficient for theoretical analysis and serve as a benchmark. However, it lacks practicability since the results are dependent on the knowledge of the entire drive cycle. The results of the DP are a global optimum, but the procedure is computationally expensive and non-causal. On the other hand, the ECMS procedure is causal and results in a fast computation but optimum only at a given time instance and, hence, suboptimum in a global context. As a compromise that extracts the best features from these two approaches, the model predictive control (MPC) performs optimization over a moving finite horizon [55–57]. The MPC strategy may not be as fast as ECMS or as optimum as DP, but it is causal, fast enough and optimum over a practical range of a prediction horizon.

As nonlinearity grows as in the HEVs, the controlling capability of linear MPC shrinks. Nonlinear MPCs are efficient in handling nonlinear prediction problems. In [58,59], nonlinear MPC is adopted for power splitting and energy optimisation of HEVs. However, nonlinear MPCs are computationally expensive and have limited online applications, especially in the case of HEVs. An adaptive MPC is a viable option that offers a solution to nonlinear problems with moderate computation demand [60,61]. An adaptive MPC strategy applied in iterative tasks is reported in [61]. Such a strategy is an improvement on the linear MPC with the advantage that the internal prediction model parameters can be modified at every time step. The benefits of future prediction as a means of improving fuel economy in the presence of thermal constraints are still an open topic for research.

As a contribution, the starting point of this work is the estimation of the SOH of the cell experimentally under constant load conditions with PL-ELM at room temperature of the cell. The analysed deterministic PL-ELM algorithm provides an alternative solution for improving generalization in SOH estimation of the cells in a battery pack. Furthermore, SOH estimation is analysed under dynamic load conditions at room temperature taking advantage of the time-independent ANN-based classifier. Relevant features are extracted for the training and validation of the models. A SOC estimation model is designed with an SPKF and the model is experimentally validated. The estimator is built on a developed cell model and experimentally validated under dynamic load conditions. The developed SOH

estimator is then integrated with the SPKF to improve the accuracy of SOC estimation as the cell ages across the cycle life. This approach takes advantage of the adaptability of the SPKF and the time-independent ANN-based SOH classifier to enhance SOC prediction. Finally, the work investigates the influence of the battery pack capacity on the thermal behaviour and the fuel consumption of the HEV using an adaptive MPC strategy. The information from the prediction horizon of the MPC helps to minimise overdesign by reducing the minimum battery capacity that prevents thermal runaway. Hence, a minimum battery capacity that allows battery use without thermal implications is defined.

Chapter 2. State of Health Estimation with Parallel Layer Extreme Learning Machine (PL-ELM)

This work begins with designing a SOH estimation algorithm with the objective to enhance the generalisation of the estimation for all the cells in a battery pack. The analysis was experimentally conducted with the PL-ELM algorithm under constant load conditions. The advantages in terms of its low complexity and computational efficiency, especially for SOH estimation make it attractive for industrial applications and research purposes. As a contribution, this section demonstrates the application of a deterministic PL-ELM algorithm as an alternative solution for improved generalization of SOH estimation of the set of cells in a battery pack. A set of suitable feature variables that provide significant correlations with the SOH are derived for training the algorithm. The PL-ELM model was trained with an experimental battery dataset collected at room temperature under a constant current load condition at the discharge phase. Model validation was performed with a dataset of other cells of similar specifications that were aged under a constant load condition.

2.1. Methodology

2.1.1 Deterministic Extreme Learning Machine

The ELM is a building block for developing the PL-ELM. The ELM is a method for developing a single hidden layer feedforward artificial neural network [62]. Contrary to the traditional neural network that solves optimization problems with a slow iterative training process, the ELM model implements a non-iterative least square regression and local minima is not a concern.

According to [63], the weights and biases of a single-layer feedforward network (SLFN) can be assigned randomly given that the activation function is infinitely differentiable. ELM can also be used to train SLFN with non-differentiable activation functions [64]. If the number of neurons on the hidden layer is less than the number of measurements, input weights can be randomly assigned. The output weights, which form the only unknown parameter, can then be determined analytically. ELM computes the estimated model output, y_k by solving Equation 2.1.

$$y_k = \sum_{j=1}^{m} \Phi_{j,k} \ \gamma\left(\sum_{i=1}^{n} \omega_{i,j} x_i + b_j\right) \tag{2.1}$$

where $\omega_{i,j}$ and b_j are the input weight and bias, respectively; i and n are the respective index and number of neurons on the input layer. The number of neurons corresponds to the number of feature variables, j and m are the respective index and number of neurons on the hidden layer, and k is the sample index. $\gamma()$ is a sigmoid activation function and $\Phi_{j,k}$ is the output weight.

Many activation functions including; hyperbolic and cosine activation functions exist in the literature. With an equal number of input neurons, a sigmoid activation function (SAF) returns an enhanced dataset discrepancy or separation when compared with a host of existing activation functions according to [64]. Also, increasing the number of input neurons (independent characterising feature variables) improves the discrepancy of the dataset.

Equation 2.1 can be re-written as Equation 2.2 given the hidden layer matrix, $H = \gamma(\omega_{i,j} x_i + b_j)$.

$$\mathrm{H}\Phi = y \tag{2.2}$$

It is necessary to compute $\widehat{\Phi}$ to approximate Φ such that an estimated value $\hat{y}$ approximates the true y. The work of [64] highlights the variants of ELM defined based on the output weight $\widehat{\Phi}$, including backpropagation tuning ELM (tELM) and regression-based ELM (rELM). In this work, $\widehat{\Phi}$ is computed least square approximation based on the generalized Moore–Penrose inverse method to minimise the estimation error.

$$\widehat{\Phi} = H^{+} y \tag{2.3}$$

where H^{+} is the generalized Moore–Penrose inverse matrix.

In the original ELM, the weights and biases of the hidden layer are assigned randomly. Although the estimated result may occasionally track the reference, the learning process is not deterministic and lacks repeatability.

The resulting model can be unstable [64] under certain conditions. This is based on the fact that the randomly assigned input weights and biases have infinite possibilities. In addition, it has been shown that the input weights and the hidden layer biases do not necessarily have to be tuned when assigned and that the output layer matrix can remain unchanged [63]. Therefore, a deterministic ELM is designed by assigning the weights and biases using Equation 2.4. This increases the likelihood of having different values of H_j while limiting the weight within the distribution range of 0 to 1 [64]. The bias is distributed within the range of 0 to 1. By assigning the weights and biases deterministically, a stable PL-ELM model is obtained.

$$\omega_{i,j} = \frac{1}{2}\left[\left(-1 + \frac{2}{n}i\right) + \left(-1 + \frac{2}{m}j\right)\right]; \qquad b_j = \frac{j}{m} \tag{2.4}$$

2.1.2 Deterministic Parallel Layer Extreme Learning Machine

PL-ELM is developed from the building blocks of ELM. The PL-ELM provides independent projection into the feature space with a two-parallel layer network. Each of the projections is nonlinearly activated and they combine through a product. This generates a more powerful nonlinear mapping than just a single activation function, and the prediction capacity is enhanced [65–68]. Since ELM is based on adjusting only the linear parameters using the least squares estimate (LSE), the PL-ELM network provides more freedom for proper adjustment [66].

To develop the PL-ELM model, a second nonlinear layer is introduced in parallel with the hidden layer of the deterministic ELM. The additional parallel layer helps to improve the nonlinearity handling. Adopting PL-ELM is justifiable since it is possible to achieve model improvement in terms of accuracy with only a little increase in model complexity.

The weights of the second component of the PL-ELM are also assigned deterministically but with a low-discrepancy sequence (LDS) [65,69]. Some families of LDS have been developed to efficiently generate a sequence of points deterministically [65]. An LDS tries to maintain the discrepancy of the resulting points within $[0, 1]^n$ as small as possible, and provides a favourable asymptotical rate of convergence of the discrepancy itself. The weights and biases of the first component of PL-ELM are assigned with Equation 2.4, while the weight of the second component is assigned with Halton's LDS [65] but with zero bias. The structure of PL-ELM is shown in Figure 2.1.

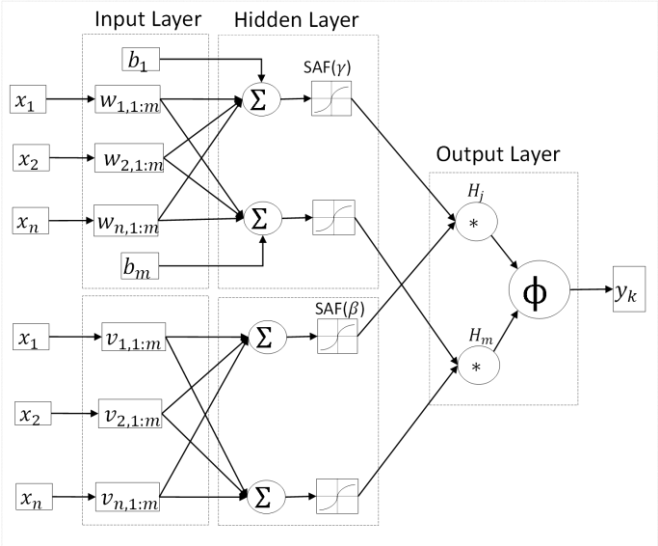

Figure 2.1: Parallel layer extreme learning machine architecture [65]. The weights and biases of the upper layer are assigned with Equation 2.4. The lower layer is weighted with Halton's low-discrepancy sequence (LDS) and zero-biased.

By introducing a parallel layer, Equation 2.1 is modified for PL-ELM as Equation 2.5.

$$y_k = \sum_{j=1}^{m} \Phi_j \left(\gamma(\omega_j x_k + b_j) \otimes \beta(v_j x_k)\right) \tag{2.5}$$

β and γ are the nonlinear SAF of the two parallel ELM layers; v_j and ω_j are the weight matrices for the respective parallel input layers; and b_j is the bias; $x_k \in \mathbb{R}^{1\times n}$. Equation 2.5 can then be written compactly in form of Equation 2.2 such that the overall hidden layer matrix, H is computed as the element-wise product ($\otimes$) of the individual parallel hidden layer matrices in Equation 2.6.

$$H = H_\gamma \otimes H_\beta \tag{2.6}$$

The parallel layer matrices H_γ and H_β are expressed in Equations 2.7 and 2.8 respectively for N distinct samples of (x_k, y_k).

$$H_\gamma = \begin{pmatrix} \gamma(\omega_1 x_1 + b_1) & \dots & \gamma(\omega_m x_1 + b_m) \\ \vdots & \vdots & \vdots \\ \gamma(\omega_1 x_N + b_1) & \dots & \gamma(\omega_m x_N + b_m) \end{pmatrix} \in \mathbb{R}^{N\times m} \tag{2.7}$$

$$H_{\beta} = \begin{pmatrix} \beta(v_1 x_1) & \dots & \beta(v_m x_1) \\ \vdots & \vdots & \vdots \\ \beta(v_1 x_N) & \cdots & \beta(v_m x_N) \end{pmatrix} \in \mathbb{R}^{N \times m} \tag{2.8}$$

It is desired to compute $\widehat{\Phi}$ as in Equation 2.3 such that the error between the estimated and the measured output is minimised as in Equation 2.9.

$$\left\| H\widehat{\Phi} - Y \right\| = \min_{\Phi} \|H\Phi - Y\| \tag{2.9}$$

2.1.3 Experimental Dataset Description

The analysis was conducted with the dataset of a set of 2 Ah capacity 18650 lithium-ion cells provided by the prognostic centre of excellence (PCoE) at NASA's Ames Research Centre for fault prediction and diagnostic studies [70]. The experiment was conducted at room temperature, completely cycling different batteries until their end-of-life (EOL). Each cycle involved a complete charging and discharge of the cell. Charging was carried out in a constant current (CC) mode of 1.5 A (about 0.75 C-rate) until the cell voltage reached 4.2 V and then continued in a constant voltage (CV) mode until the charge current dropped to 20 mA. Discharge of cells B0005, B0006, B0007, and B0018 was done at a constant current (CC) load of 2 A (that is a 1 C-rate) until the cell voltage reached the minimum allowable voltage.

2.1.4 State of Health (SOH)

The health of a lithium-ion cell is affected by cycle life ageing due to usage, and calendar ageing due to storage time. Since the cell has been cycled until the end of life (EOL) with negligible storage time, the calendar ageing is neglected in this work. SOH as a health state index is computed based on the capacity measurement over the cycle life of a cell to account for the capacity fading. When a cell is fully charged, it has a maximum releasable capacity, C_{max}. This capacity can change relative to the capacity at the beginning of life (BOL), C_{bol} which is assumed to be the maximum cell capacity when newly installed. C_{max} decays with storage time and usage. The computation of SOH in Equation 2.10 is based on capacity fading SOH [71].

$$\text{SOH} = \frac{C_{max}}{C_{bol}} \times 100\ \% \tag{2.10}$$

Considering one of the datasets (B0005), the EOL of the battery was reached after 170 cycles. The SOH that describes the ageing of the battery until the EOL is shown in Figure 2.2 for the charge and discharge phases.

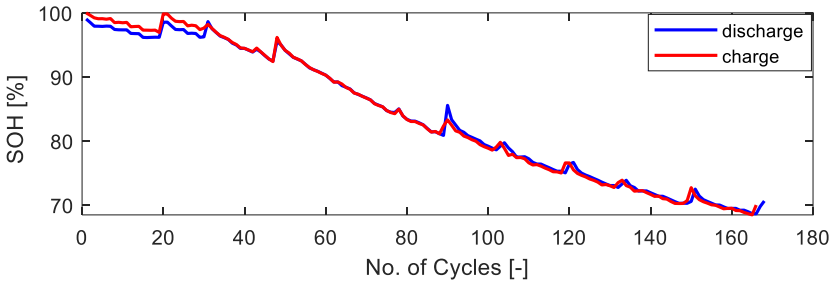

Figure 2.2: Similarity of state of health (SOH) in the charge and discharge phases. SOH of B0005 is shown to decrease with the number of cycles.

The slight mismatch at the BOL of the cell is attributed to a measurement error which was corrected over the rest of the cycle life of the cell.

2.1.5 Characterisation and Feature Selection

The training of the PL-ELM requires suitable inputs or feature variables obtained from the characterisation of the SOH of the cells. The characterising variables are the combination of the internal states and an operational variable. The internal states are often not measurable. These states are estimated and they include the SOC and the state of energy (SOE). The operational variable such as terminal voltage can be measured directly by the management system (BMS). The feature variables used in this model are the discrete variation of the characterising variables captured in a buffer of 90 seconds time length. This variation of the characterising variables (ΔV, ΔSOC, ΔE) helps to capture the ageing dynamics of the cell. Hence they are adopted for training the SOH estimation algorithm. The features and the characterising variables are listed in Table 2.1.

Table 2.1: Model feature and output variables.

#	Characterising Variable	Model Train Features	Unit
		Training Feature	
1	Voltage (V)	Δv	[V]
2	State of Charge (SOC)	ΔSOC	[%]
3	Energy (E)	ΔSOE	[Wh]
		Model Output	
1	State of Health (SOH)		[%]

The variation of the discrete points of the indicator variables are acquired with a buffer of 90 seconds time length and was used as input to the SOH

estimation model. The choice of the discrete point variation interval was based on model tuning for accuracy.

The experimental dataset consists of the measured cell terminal voltage and the corresponding current delivered based on request. Theoretically, the measured terminal voltage is a contribution of open-circuit voltage (v_{oc}), polarization voltage (v_p) and the Ohmic voltage (v_{ohm}) according to Equation 2.11.

$$v(t) = v_{oc}\big(\mathrm{SOC}(t)\big) + v_p(t) + v_{ohm}(t) \tag{2.11}$$

The v_{oc} is the equilibrium voltage and it is a function of SOC. The v_p models the transient of the voltage dynamics. The presence of the v_{ohm} implies that the energy state is not conserved and hence with usage, the energy capacity of the cell reduces and ageing occurs. To demonstrate the capacity fading/ageing, a two-dimensional voltage–capacity plot of the experimental dataset is shown in Figure 2.3. Each curve represents a single cycle.

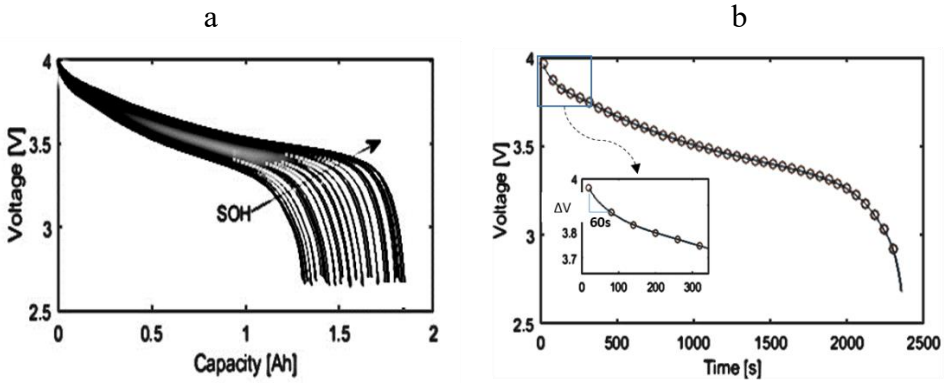

Figure 2.3: Voltage characterisation and feature extraction. a: voltage - capacity for a constant current discharge profile. The arrow is the reverse direction of ageing across cycles. b: The data points are taken with a buffer of 90 seconds time length for computing the variation of voltage used as the feature variable.

As the lithium-ion cells age, the maximum and minimum voltages of the cells are reached quicker during charge and discharge respectively, as a consequence of the degraded charge/energy capacity. Cell SOC is an important battery parameter upon which many variables and other parameters are dependent. SOC is commonly defined as the percentage of the maximum possible charge that is present inside a rechargeable battery. Thus, the SOC serves as the fuel gauge for batteries. SOC can be expressed as the ratio of current capacity and the capacity releasable at the end of discharge. It is computed in Equation 2.12. Equation (2.13) computes the relative state of charge, $\Delta\mathrm{SOC}$ across a buffer of defined time length t_b with respect to the initial time t_0.

$$\mathrm{SOC}(t) = \mathrm{SOC}(t_0) + \frac{\int_{t_0}^{t_b} \eta_c \, i(t)dt}{C_{max}} \tag{2.12}$$

$$\Delta\mathrm{SOC}(t) = \mathrm{SOC}(t_b) - \mathrm{SOC}(t_0) \tag{2.13}$$

The total amount of charge deposited in the cell in the charge phase is often not completely recoverable in the discharge phase [72,73]. This could result in an offset of SOH between the charge and discharge phases. To compensate for this offset, the charge current is weighted with a Coulombic efficiency η_c. This value is chosen such that the error between the SOH in the charge and discharge phases is minimized. The low offset between the charge and discharge phases in Figure 2.2 is an indication of very high cell Coulombic efficiency. For this reason, a Coulombic efficiency $\eta_c = 100\%$ is assumed. C_{max} is the maximum capacity of the cell for a given cycle. It is updated at each cycle as the cell ages such that the SOC is always in the range of 0% - 100% but the slope varies.

The SOE provides information about the integrated power that can be released from the battery. A large SOE error may lead to over-charging or over-discharging, consequently accelerating ageing life, and increasing safety hazards. Therefore, SOE is a critical index for energy optimization and management. The SOE is computed by integration of the product of voltage and current over time. For a constant discharge current, the equation for SOE computation is shown in Equation 2.14.

$$\mathrm{SOE}(t) = \int_{t_0}^{t_b} \eta_e v(t) i(t) dt \tag{2.14}$$

In a similar way, the energy efficiency η_e is computed as the best fit comparison between the maximum absolute SOE distributions across the ageing cycles [73] and applied to the charge phase. An energy efficiency $\eta_e = 100\%$ is assumed. Figure 2.4a shows a three-dimensional plot of SOC, voltage, and energy, while Figure 2.4b shows the variations in voltage, SOC, and SOE. It can be seen from Figure 2.4a that the total amount of energy that can be delivered by the cell significantly reduces as the cell ages.

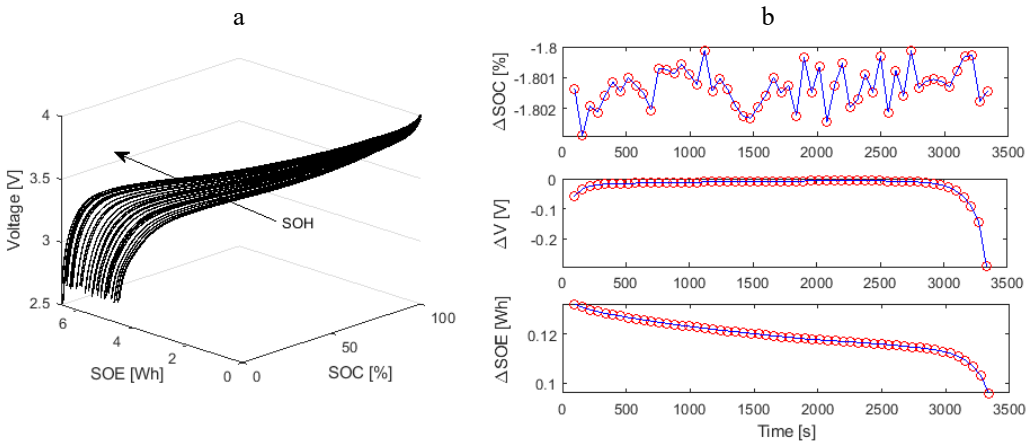

Figure 2.4: three-dimensional characterisation and feature extraction. a: SOC–SOE–voltage characterisation for a constant current discharge profile. The arrow points in the reverse direction of ageing across cycles. b: Feature variables obtained as variations of voltage, SOC, and SOE.

From Figure 2.4b, it can be seen that the variation of voltage between 300–3000s (90–10% SOC) is almost constant. For this reason, SOH discrimination in this zone is poor with only voltage and SOC. On the other hand, the variation of energy does not show this behaviour. The energy variable thus provides an additional feature for characterising SOH.

2.1.6 Summary of Scheme Setup Procedure

The SOH estimation scheme using the PL-ELM algorithm as proposed in this paper is summarized below.

Model Input:	$\boldsymbol{x} = [\Delta \boldsymbol{v}, \Delta \mathbf{SOC}, \Delta \mathbf{E}] \in \mathbb{R}^{\mathbf{3\times N}}$
Model Output:	$\boldsymbol{y} = \mathbf{SOH} \in \mathbb{R}^{\mathbf{1\times N}}$

- The dataset consists of voltage that is acquired by ageing the battery with a constant current profile;
- The input of the PL-ELM model is computed as a discrete point variation of the voltage, SOC, and energy at a 90 seconds interval, as in Figure 2.4b;
- The discrete point output is computed as the mean SOH within the same interval;
- The discretized input and output data are used to train the model, to determine the parameters (weight and bias) of the PL-ELM model;

- The number of hidden layer neurons is adjusted to obtain an optimum model, allowing for a compromise between performance and complexity;
- The designed SOH estimation model is then validated using the dataset of other cells of the same type that have been aged under the same current load conditions as in the training.

2.2. Results and Discussion

2.2.1 PL-ELM Model Training

The results shown in this section demonstrate the estimation of SOH with deterministic PL-ELM to enhance generalization over a set of batteries of similar specifications. The result demonstrates that although each cell used in the test had a distinct distribution, the estimation algorithm performance was optimum over the entire set. In other words, the designed model is not affected significantly by the drift problem. The PL-ELM estimation model performance is compared with other methods, including the deterministic ELM algorithm and an ICA-based algorithm reported in [27]. The performance evaluation was computed with root mean square error (RMSE) and mean absolute error (MAE) indices, considering a 99% confidence interval of the errors. This consideration helps to provide information about the percentage of errors outside the defined error bound. The difference between RMSE and MAE is useful for understanding the error variations in the predictions. The small difference between the RMSE and the MAE errors indicates low error variance in the prediction set. The root mean square error (RMSE) and mean average error (MAE) indices were computed using Equations 2.14 and 2.15, respectively.

$$\mathrm{RMSE} = \sqrt{\frac{1}{\mathrm{N}}\sum_{i=1}^{\mathrm{N}}(y_i - \hat{y}_i)^2} \tag{2.15}$$

The quadratic scoring RMSE is desirable to amplify large errors while diminishing small ones. A linear scoring MAE is defined as

$$\mathrm{MAE} = \frac{1}{\mathrm{N}}\sum_{i=1}^{\mathrm{N}}|y_i - \hat{y}_i| \tag{2.16}$$

The inputs to the PL-ELM network are the model training features derived as the discrete variation of the characterising variables in Table 2.1. The structure of the PL-ELM is defined by varying the number of neurons in the training phase. The number of neurons chosen was a compromise

between model complexity and accuracy. To fix the model structure, the number of neurons was varied from 1 to 20, as seen in Figure 2.5c. It may be sufficient to use about twelve (12) neurons to obtain an optimal model in terms of complexity. However, by increasing the number of neurons sufficiently (20 neurons in this case), the estimation accuracy of the model was improved. The scheme was designed and simulated with Matlab software, and the total number of 5523 data samples from the B0007 dataset was used to train the model. Figure 2.5a shows the result of the training phase of PL-ELM while Figure 2.5b shows the normal distribution of the error. Figure 2.5c shows the performance based on model complexity when the number of neurons varied.

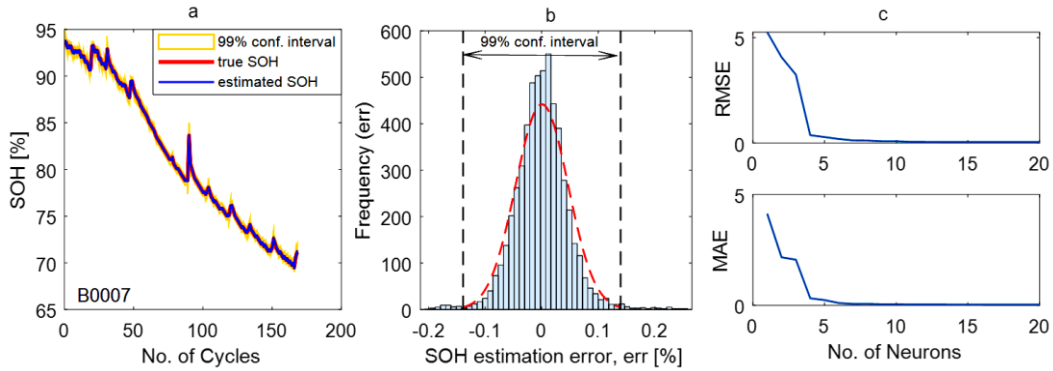

Figure 2.5: The result of parallel layer extreme learning machine (PL-ELM) model trained with B0007 dataset and consideration of a 99% confidence interval on the error. a: the result of SOH estimation with 20 neurons; b: normal distribution of the error for 99% confidence interval; c: performance versus model complexity over 20 neurons.

The RMSE of the trained model performance was computed as 0.046, while the mean average error (MAE) is 0.034 using 20 neurons in the parallel layer network. Error estimation was obtained for a 99% confidence interval. The resulting model error is an approximation of natural distribution. The percentage out of bound error $\%E_{OB}$ indicates the percentage of the error that is outside the 99% confidence interval. In the training phase, $\%E_{OB}$ is about 1.57% of the training data points were outside the 99% confidence interval. The $\%E_{OB}$ for the training and validation phases are reported together with the performance result in Table 2.2. The number of data points used in the training and validation is also tabulated.

Table 2.2: SOH estimation performance comparison between PL-ELM and incremental capacity analysis (ICA) model in training and validation. and out of bound error ($\%E_{OB}$) information are also provided.

		PL-ELM				**ICA Model** [27]
		Data Point	**RMSE**	**MAE**	**$\%E_{OB}$**	**RMSE**
Training	B0007	5523	0.046	0.034	1.570	0.66
Validation	B0005	5154	0.362	0.345	2.037	0.87
	B0006	5115	0.473	0.355	3.240	2.49
	B0018	4021	0.170	0.158	0.250	-

The model performance is influenced by the choice of the discrete point variation interval of the input features. The choice of the interval was based on model tuning for accuracy. The results of the interval variation are not fully reported in this work. However, it can be shown that extremely short intervals result in noisy feature variable points, while extremely large intervals result in loss of information. In both extreme cases, the model accuracy is impacted adversely. In this work, a sampling interval of 90 seconds is believed to be optimum. Using a 60 seconds interval increased the training RMSE from 0.046% to 0.053%. On the other hand, with a 120 seconds interval, the training RMSE was reduced to 0.043%. However, the maximum validation RMSE increased from 0.473% to 1.089%.

2.2.2 PL-ELM Model Validation

The training of the estimation model was done with the battery B0007 dataset. The model was validated with other batteries of the same type: B0005, B0006, and B0018. All the batteries were aged with a constant current profile of 2 A. The performance of the designed model was compared with the result obtained with the ICA-based model using the same dataset as reported in [27]. The performance results are reported in Table 2.2. From the comparison, the proposed model shows relatively improved performance.

The variation of RMSE, as shown in Table 2.2, is in the range of 0.170–0.4736 in the validation phase. Moreover, the variation of the MAE range is in the range of 0.158–0.355. Figure 2.6 shows the validation of the PL-ELM model with batteries B0005, B0006, and B00018.

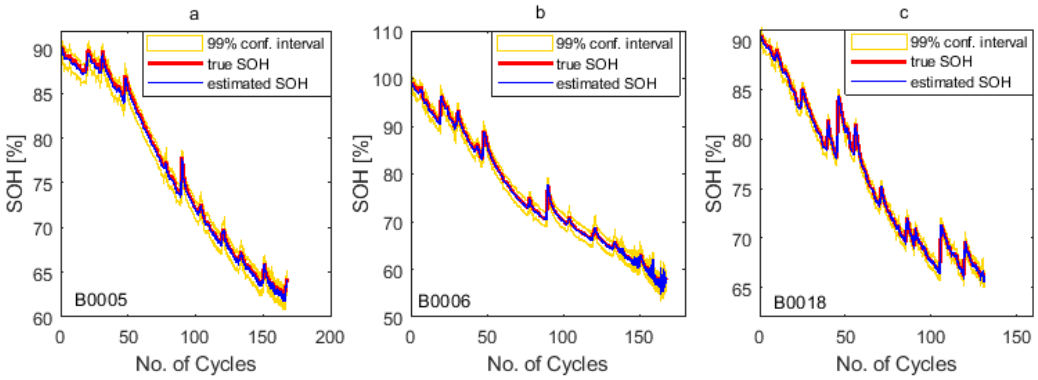

Figure 2.6: PL-ELM model validation. a–c: model validation with B0005, B0006, and B0018 dataset, respectively.

It can be seen from Figures 2.5 and 2.6 that the ageing pattern is different for the individual batteries even though they were aged under the same load condition. This difference results from cell-to-cell parameter variation due to production tolerance [25]. From the results, the PL-ELM model can cope with the nonlinearity of SOH for all the cells with reasonable accuracy.

To evaluate the limitation of this model, it is important to account for uncertainties that result from sensor noise and model inaccuracy. Input data is affected by noise which interacts with the model inaccuracy to increase the model uncertainty. The PL-ELM model has been designed considering the influence of this noise. In this work, only the current sensor noise has been analysed since the information about the voltage sensor is not available at the time of publication. The analysis of the sensor noise gives an idea of the quality of the sensor that should be adopted in practice. SOH estimation models can be integrated as a subsystem to improve SOC estimation results. In our case, SOC is estimated with SPKF, and it is important to analyse the valid operating range of the PL-ELM model based on the noise distribution. Such information helps to define limits that guarantee the stability of SPKF. Figure 2.7 shows the distribution of the input sensor noise and model uncertainty in the validation phase.

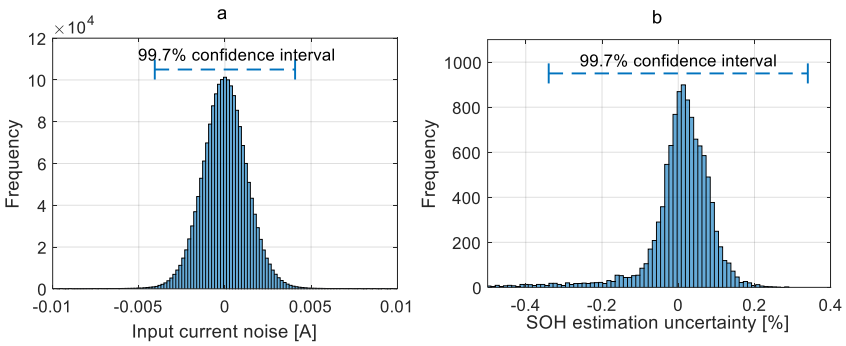

Figure 2.7: Distributions of noise and model uncertainty of PL-ELM; a: input current sensor noise distribution, b: model uncertainty distribution.

From Figure 2.7a, the input data is corrupt with a noise of 0.0014 A standard deviation (SD), corresponding to ± 0.0042 A (3×SD) within a 99.7% confidence interval. The frequency of the current sensor noise is in the range of 3.5×10^{-6} to 3.1 rad/s. With such a range of input current noise in consideration, the model can be trusted to estimate SOH with an uncertainty of ± 0.113% SD as seen in Figure 2.7b.

2.2.3 Model Comparison with Deterministic ELM and Demonstration of the Drift Problem

Although ELM is the building block of PL-ELM, it does not have as much nonlinearity handling capacity as PL-ELM. ELM may be suitable for systems with fairly low nonlinear behaviour. Like many machine learning algorithms, the ELM model often experiences a drift when the level of dissimilarity between the distribution of the training and the validation dataset is high. To compare results between ELM and PL-ELM, the experiment was repeated as summarized in Section 2.1.6, replacing the PL-ELM with the deterministic ELM single-layer model. The results of SOH estimation using the ELM model are shown in Figure 2.8. As in the PL-ELM, the ELM model was trained with the battery B0007 dataset and validated with the B0005, B0006, and B0018 datasets. The training RMSE performance of the battery is 0.245, while the MAE was 0.191. In the validation, the RMSE is in the range of 0.501–1.563, while the MAE is in the range of 0.361–0.907. The ELM model performance is reported in Table 2.3.

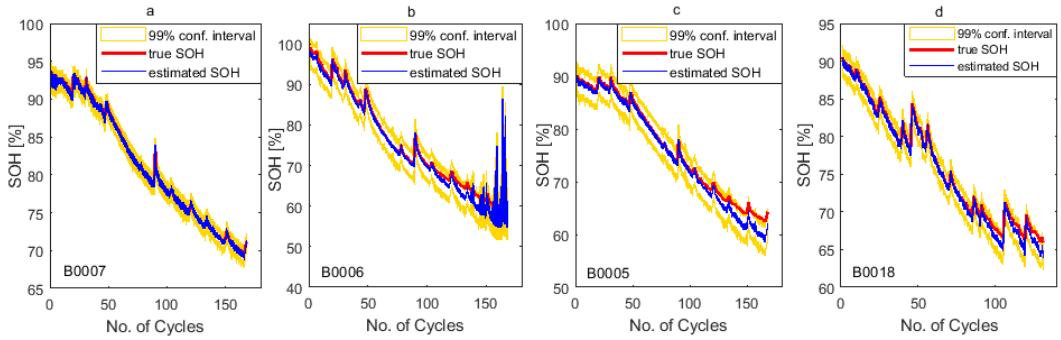

Figure 2.8: Extreme learning machine (ELM) model training and validation. a: model trained with the B0007 dataset; b–d: Model validated using the B0005, B0006, and B0018 datasets, respectively.

The model estimation tends to drift away from the true SOH across the entire cycle. Although the model results shown here were obtained for twenty (20) neurons, the drift problem never disappears regardless of the number of neurons used.

Table 2.3: SOH estimation performance of deterministic ELM model for training and validation. The $\%E_{OB}$ information are also provided

		Data Point	RMSE	MAE	$\%E_{OB}$
Training	B0007	5523	0.245	0.191	0.615
Validation	B0005	5154	1.117	0.762	1.24
	B0006	5115	1.563	0.907	0.19
	B0018	4021	0.501	0.361	0.89

From the results of Tables 2.2 and 2.3, the PL-ELM and the ELM can be compared based on performance. The training RMSE of the deterministic ELM relative to PL-ELM increased from 0.046% to 0.245%. The MAE increased from 0.034% to 0.191%. The maximum validation RMSE of the ELM increased from 0.473% to 1.563%, while the maximum MAE increased from 0.355% to 0.907%. These highlight the improvement in the performance of the PL-ELM as compared with the ELM. The poor performance of the deterministic ELM model is evident in the SOH estimation results. The model drifting that affects the ELM becomes more pronounced as the battery ages.

The model was set up, simulated, and validated using Matlab and Simulink software, version 2020b. To understand the real-time performance of the model in terms of computational cost and memory consumption, the algorithm was deployed to a Texas Instruments Delfino™ F28379D device. The 32-bit duo core MCU was connected to Simulink via serial connection and a processor-in-the-loop (PIL) model simulation was performed. On the basis of the simulation, an average execution speed of 93 µs was recorded with 0.9305% average CPU utilization. This suggests that the model is suitable for online applications.

2.3. Summary and Conclusions

The SOH estimation of lithium-ion cells is analysed under constant load conditions using the regressive PL-ELM algorithm. The work demonstrates the possibility of using a single model to estimate the SOH of a set of similar cells in the battery pack. This is possible due to the improved nonlinearity handling capability of the PL-ELM.

SOH was experimentally characterised using voltage, SOC, and SOE of the cell. The PL-ELM model was trained and validated for SOH estimation using the discrete variation of the characterising variables captured in a buffer of 90 seconds time length. The RMSE of the validated model varies from

0.046% to 0.473% and the MAE error from 0.034% to 0.355% with low error deviation beyond the 99% confidence interval for the set of cells tested. An improved relative performance was obtained for the proposed model in comparison with the other highlighted algorithms.

The model was tested on an MCU board with PIL simulation. An execution time of 93μseconds in real-time is recorded with 0.9305% CPU occupation. On the basis of the low model complexity, performance, and computation efficiency, the model is suggested as being suitable for online applications.

Chapter 3. State of Health Estimation under Dynamic Load Conditions

In electric vehicle (EV) applications, accurate SOH estimation minimises failure risk and improves reliability by predicting battery health conditions. The challenge of accurate estimation of SOH is based on the uncertain dynamic operating condition of the EVs and the complex non-linear electrochemical characteristics exhibited by the lithium-ion battery. This section presents an artificial neural network (ANN) classifier, designed and experimentally validated for the SOH estimation of lithium-ion batteries under dynamic load conditions.

As the main contributions, a set of suitable feature variables that provide significant correlations with the SOH are derived. An artificial neural network classifier is designed and trained experimentally with these features under dynamic load conditions at room temperature of the battery. Furthermore, the classifier model is experimentally validated under different load scenarios, including dynamic load, constant load, and step load conditions. Finally, the classifier is validated for use in multiple cells of similar specifications under dynamic load conditions.

3.1. Methodology

3.1.1 System Description and Experiment

The system-level application architecture for SOH estimation is shown in Figure 3.1. Given a load request from the cell, the measured current and the corresponding voltage are acquired from the cell. The SOC and SOE are computed with suitable functions that are embedded in the Battery Management System (BMS). The SOH estimation algorithm is executed periodically with no dependence on the data log of previous estimations. When the algorithm is triggered, the feature extraction algorithm extracts the relative voltage, SOC and SOE within a buffer of 40 seconds time length. The discrete instantaneous values of the SOC and SOE are also acquired at this time interval. These contribute to the training features that are given as input to the ANN-based classifier. Considering the slow dynamics of SOH, the algorithm can be triggered on an hourly basis.

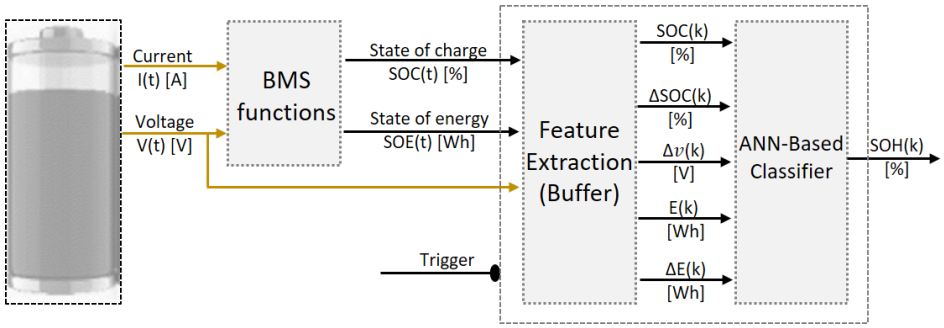

Figure 3.1: Architecture for SOH estimation using ANN-based classifier. The yellow signals are measurements from the cell.

The proposed method aims at estimating the SOH of a lithium-ion cell under dynamic varying load conditions. In the present analysis, the SOC and SOE are computed analytically. The analysis is conducted with a single cell in a module consisting of six (6) individual LG MJI 18650 lithium-ion cells of 3500mAh capacity connected in series. The characteristics of the cells are shown in Table 3.1. The procedure has been designed for a single cell. The SOH of a battery pack can be developed by series and parallel connection of cells, putting into consideration the capacity variations in the cells and the error introduced by the interconnection resistance [17].

Table 3.1: Nominal characteristics of cylindrical LG 18650 MJ1 lithium-ion cell [74]

Cell chemistry		$LiNiMnCoO_2$
Nominal capacity (@ 0.2C, 4.2V-2.5V, 23°C)		3500mAh
Nominal voltage		3.635V
Cut-off voltage		2.5V
Max. discharge current		10A
Cycle life (charge@1.5A, discharge@4A)		> 400 cycles
Charge Condition	Max. current	1C (3400mA)
	Max. voltage	4.2 ± 0.05 V
Operating Condition	Charge	0 - 45°C
	Discharge	-20 - 60°C
Mass		49.0g
Dimension	Diameter	18.5mm
	Height	65mm

The data used for the experiment was acquired from a test bench that is developed in-house. The test bench shown in Figure 3.2 consists of a module of six cells connected in a series and the cell voltages are measured with Elithion standard generic cell boards 1PR0000. Two LM35 Texas Instrument temperature sensors measure the cell surface temperature. An Elithion (Lithulmate) BMS is installed on

the test bench to enhance the safety of the acquisition process. An Arduino Mega board connected via LAN to a dedicated PC is used to acquire the measured data. As an extra safety measure, the system is equipped with an emergency stop device.

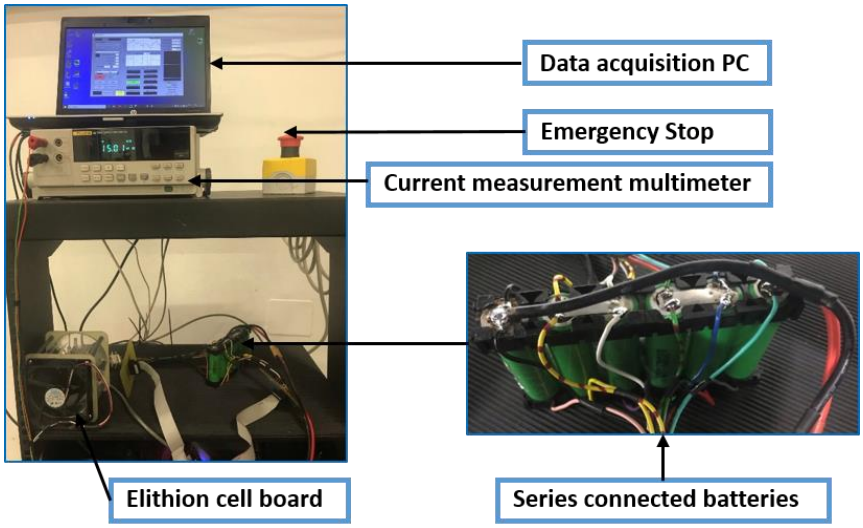

Figure 3.2: Experimental setup for data acquisition of lithium-ion batteries connected in series.

The experiment is conducted in a controlled ambient room temperature condition. The cells are cooled by natural convection with proper air circulation, and it is ensured that the room temperature is unaffected by the heat from the cells. The two temperature sensors are mounted on the surface of the cells to ensure measurement consistency and the information is fed to the BMS for detecting overheating.

The model is trained and validated with ageing profiles that are comparable to standard automotive drive cycles. To age the cell, a major cycle consisting of seventeen (17) profiles is repeated fourteen (14) times corresponding to about 470 cycles. The ageing profiles are either charge or discharge phases or a sequence of charge and discharge phases as in the dynamic load profile. The profiles include constant current (1.75 A) charge, constant current (0.7 A) discharge, step current (0 A to 4.23 A) charge, constant power discharge, step current (0 A to -10 A) discharge, and dynamic current profile. The distribution of the dynamic profile is comparable to that of the standard dynamic stress test (DST) drive cycle. Each charge or discharge phase is completed with the respective SOC of 100% or 0% and followed by a rest period. The choice of these ageing profiles is to create the possibility to validate the cells under different load conditions. The profiles are shown in Figure 3.3. The entire ageing process lasted for about 77 days.

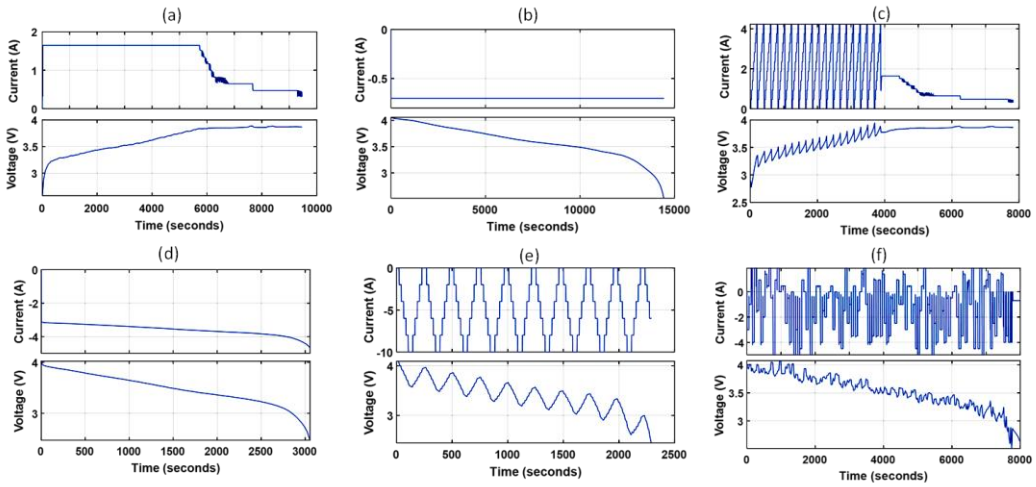

Figure 3.3: Characteristics of the major profiles used for cell ageing. a: constant current constant voltage charge (1.75 A); b: constant current (0.7 A) discharge; c: step current (0 A to 4.23 A) charge; d: cell module constant power discharge (75 W); e: step current (0 A to -10 A) discharge; f: dynamic current profile.

3.1.2 State of Health (SOH)

The SOH of an energy storage system is defined in Section 2.1.4. The experiment for SOH estimation was conducted at room temperature, cycling the cell with the sequence of different load profiles until the EOL is reached. According to the standard adopted by the automotive industry, the EOL of a cell is reached after 20% capacity fading. Therefore, the useful life of the cell is considered between 100% to 80% SOH [75]. To benchmark the SOH, a constant current discharge profile of 0.7A (0.2C) is applied at the intervals in-between the sequence of profiles to compute the SOH. With such a low C-rate, the internal resistance of the cell is low, and the approximate value of SOH with minimum load stress can be obtained. With this current profile, the cell is completely discharged in 238 minutes in the first cycle when the cell is new. When the cell gets aged, as represented by the last cycle, it gets completely discharged in 166 minutes. The SOH of the lithium-ion cell is plotted in Figure 3.4 computed according to Equation 2.10 for the ageing cycles from 100% to 70% SOH.

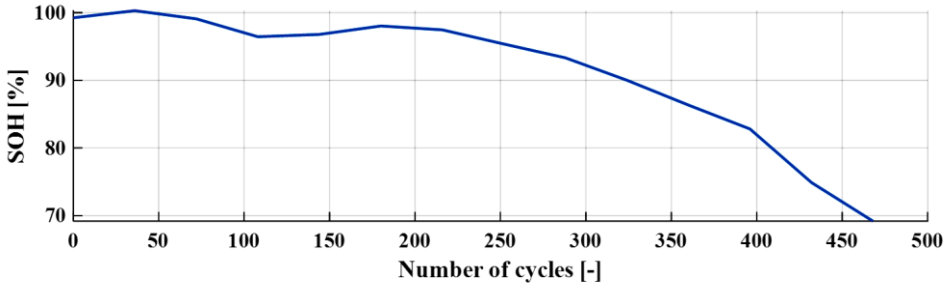

Figure 3.4: SOH of cylindrical LG MJI 18650 lithium-ion cell across the ageing cycles

To design a classifier, SOH is categorized into five (5) classes. Class 1 to Class 4 represent the range of 100% to 80% SOH, where each class corresponds to an interval of a length of 5%. Class 5 represents the SOH below 80%. These classes will be the output of the classification algorithm. The conservative interval of 5% used in this analysis is within the range of acceptance for similar applications.

3.1.3 SOH Characterisation and Feature Extraction

The cell variables that influence the SOH have been defined in Section 2.1.5. The variables include voltage [V], SOC [%], and SOE [Wh]. It is important to clarify the distinction between SOC and SOE. While SOC is the percentage of the Ampere-hour (Ah) in the cell, SOE is the area under the Ah-voltage curve. Clear distinctions also exist in the time variation of these variables as will be seen subsequently. Although SOH estimation is also influenced by environmental temperature, the analysis here is considered only for room temperature.

The SOH characterization for LG 18650 MJ1 lithium-ion cell is shown in Figure 3.5 for a constant discharge current of 0.7 A profile is applied to discharge the cell to a minimum cut-off voltage of 2.5 V. As the cell ages, the capacity and SOE depreciates and the voltage gradient becomes steeper.

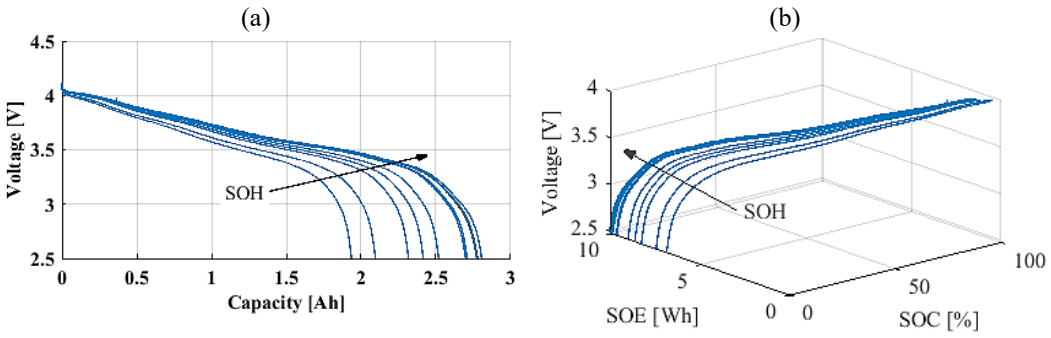

Figure 3.5: Characterisation of the SOH based on the cell at ambient environmental temperature; a: characterisation based on voltage and capacity; b: characterisation based on voltage, SOC and SOE.

Cell Coulombic efficiency is influenced by temperature and C-rate. The cell SOH across the cycle life of the cell in the charge and discharge phases is shown in Figure 3.6a for the dynamic load profile. The clear offset between these phases is an indication of relatively low cell Coulombic efficiency due to the high C-rate. The value $\eta_c = 94\%$ is chosen such that the error between the SOH across the cycle life in charge and discharge phase is minimised. The SOH of the charge and discharge phases become comparable when $\eta_c = 94\%$ is applied as in Figure 3.6b.

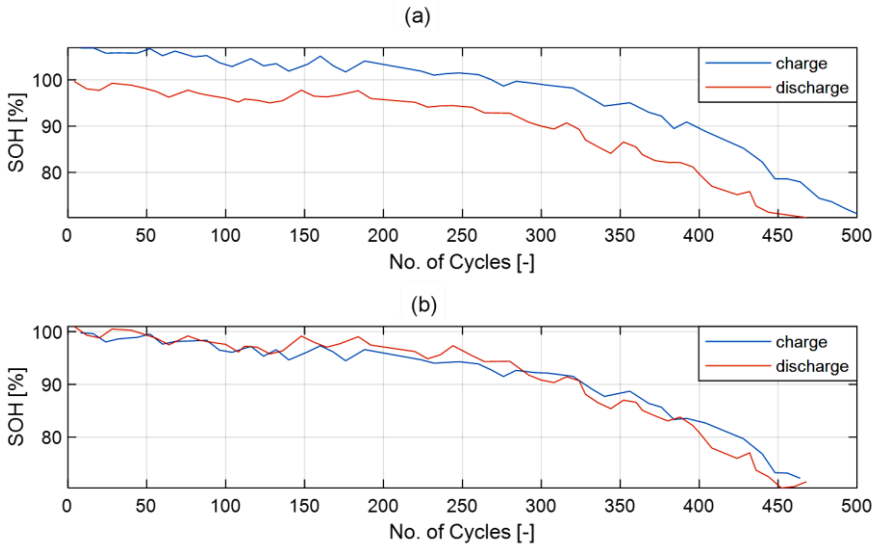

Figure 3.6: SOH of the cell computed with the dynamic profile across the cycle life of the cell. a: the charge-biased phase is not corrected with the Coulombic efficiency. b: the charge-biased phase is corrected with the Coulombic efficiency.

Similarly, the energy efficiency $\eta_e = 88\%$ is computed as the best fit comparison between the maximum absolute SOE distributions across the ageing cycles [73]. As in the SOC computation, to compensate for the energy difference between the charge and discharges phases, η_e is applied as a weighting factor to the computed energy of the charge phase.

The feature extraction block in Figure 3.1 consisting of a buffer of 40 seconds time length is designed to acquire the feature variables for training the classifier. The buffer size is chosen as a good compromise to minimise the impact of measurement noise and loss of data points. The relative values of voltage, SOC, and SOE in the buffer are computed at the interval of this buffer length. Also, the instantaneous values of both SOC and SOE are recorded. The classifier input and outputs are listed in Table 3.2.

Table 3.2: Dataset characterisation: the input and output of the ANN-based algorithm. The input features are computed on a buffer with a time length of 40 seconds.

Model Input				**Model Output Classes**	
#	**Variable**	**Feature**	**Unit**	**Class**	**Range [%]**
1.	Voltage	Δv	[V]	1	100 – 95
2.	State of charge	SOC	[%]	2	95 – 90
		ΔSOC	[%]	3	90 – 85
3.	State of energy	SOE	[Wh]	4	85 – 80
		ΔSOE	[Wh]	5	< 80

The outputs of the feature extraction block are given as input to the classifier. Figure 3.7 shows the relative values of voltage, SOC and SOE taken at intervals that correspond to the buffer time length of 40 seconds. Figures 8a and 8b show the values against time for BOL and EOL respectively. As mentioned earlier, the complete discharge of the cell lasted for 238 minutes in the first cycle when the cell is new. When aged, in the last cycle, the discharge lasted for 166 minutes.

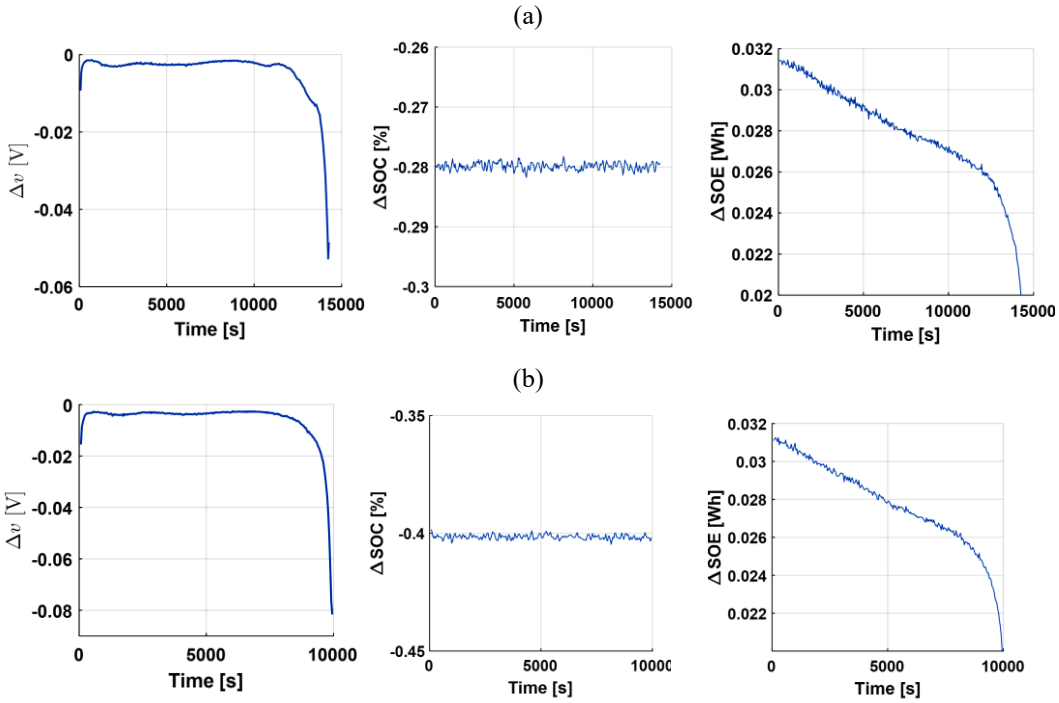

Figure 3.7: Feature extraction across buffer of time length of 40 seconds. a: Relative values of voltage, SOC, and SOE for BOL. b: Relative values of voltage, SOC, and SOE for EOL.

Information provided by the feature variables is learned by the classifier during the training. The magnitude of the variation of voltage, SOC and SOE can be seen to change significantly as the cell ages from the first to the last cycle. The Δv magnitude doubled from the original value of -0.0015V. The ΔSOC changed from -0.28% to -0.4%. The gradient of ΔSOE increases as the cell ages.

In estimating the SOH under constant load conditions, it is sufficient to train the model with Δv, ΔSOC and ΔSOE as can be seen with PL-ELM in Section 2. However, under dynamic load conditions, the instantaneous values of SOC and SOE are needed to enhance the model accuracy.

3.1.4 Design of the Classifier Model

The choice of a classification method for SOH estimation is considered suitable since it eliminates the need of staying consistent with the time history of the cell ageing and eliminates the need for model initialisation. The architecture of

the neural network classifier is shown in Figure 3.8. The network consists of the input layer, two hidden layers with ten neurons each, and the output layer. The input layer has five (5) neurons that correspond to the number of feature variables while the output layer has five (5) neurons that correspond to the number of classes. The number and the size of the hidden layers and the hidden layer neurons are determined heuristically.

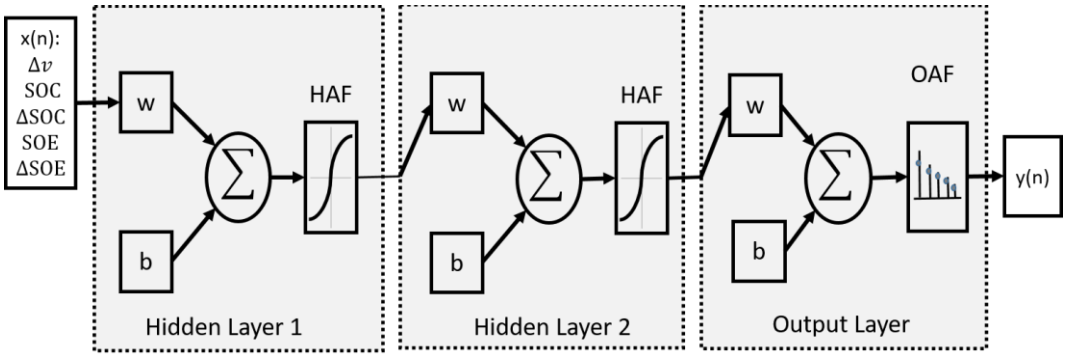

Figure 3.8: Architecture for pattern recognition feed-forward artificial neural network (ANN) for SOH classification. x(n): input, w: weight of layer neurons, b: bias of the layers, HAF: hidden layer activation function, OAF: output layer activation function.

The classifier is designed with a network training function that updates the weights w and bias b values according to Levenberg-Marquardt (*trainlm*) [76,77]. The Levenberg-Marquardt algorithm is a higher-order adaptive algorithm that minimises the mean square error (MSE) e of a neural network output layer. To minimises the error, a second order algorithm uses the Hessian to determine the weight and biases update as in Equation 3.1. The error gradient $\nabla e(\beta)$ is computed from Equation 3.2. Refer to [77] for more information.

$$\min_{\beta} e(\beta) = \frac{1}{2}\sum e_i(\beta)^2 = \frac{1}{2}e(\beta)^T e(\beta) \tag{3.1}$$

$$\nabla e(\beta) = J(\beta)^T e(\beta) \tag{3.2}$$

where $J(\beta)$ is the Jacobian matrix; β is the weight and bias parameters obtained by least-square; $e(\beta)$ is a vector of the sample point errors. The hidden layer activation function (HAF) is the hyperbolic tangent sigmoid, and the output activation function (OAF) is the softmax function. The parameters of the neural network classifier are reported in Table 3.

Table 3.3: Parameters of the neural network classifier

Parameter	Value
Number of inputs	5
Number outputs	5 classes
Training data sampling time	1 second
Number of Hidden layers	2
Number of neurons per hidden layer	10
Performance goal	0
Minimum performance gradient	1×10^{-20}
Adaptive factor, mu	0.001
Maximum validation fails	50

With the training dataset sampled at 1 second interval, the classifier model is trained once and the cross-entropy cost function is used to evaluate the performance. The training processes ended after 821 epochs using a personal computer that has an Intel(R) Core (TM) i5-2450M CPU @ 2.50GHz dual-core processor. The cross-entropy returns a low MSE performance value of 0.01035 based on Equations 3.1 and 3.2. The MSE plot is shown in Figure 3.9.

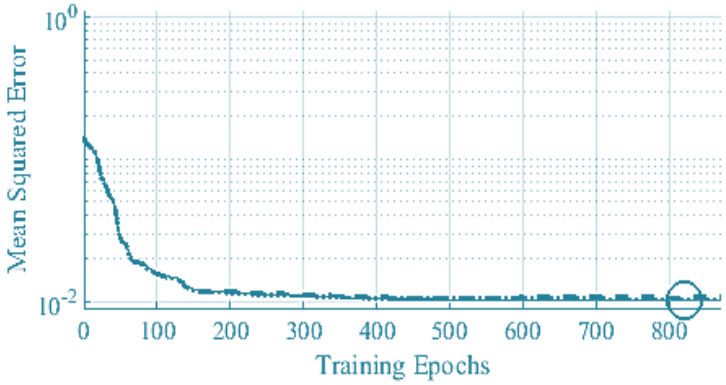

Figure 3.9: Mean square error performance result for ANN-based classifier training using Levenberg-Marquardt function.

3.2. Results and Discussion

The training and validation results are discussed in this section. The classifier is trained with the dynamic load profile whose maximum current amplitude is 5A in both charge and discharge phases. At room temperature, the model is validated with the dynamic load profile, a constant load profile, and a step load profile. The dynamic load distribution is in the frequency range of 5.8×10^{-6} to 2.9 rad/s.

Finally, the model is validated for applicability in multiple cells under dynamic load conditions.

3.2.1 Training and Validation with the dynamic load profile

The dynamic load profile consists of a total number of 130 profiles of which 118 profiles are used for the training while the rest are used for the validation. Figure 3.10 shows the first two dynamic load profiles from the set of the ageing profiles used in the model training and validation.

a:

b:

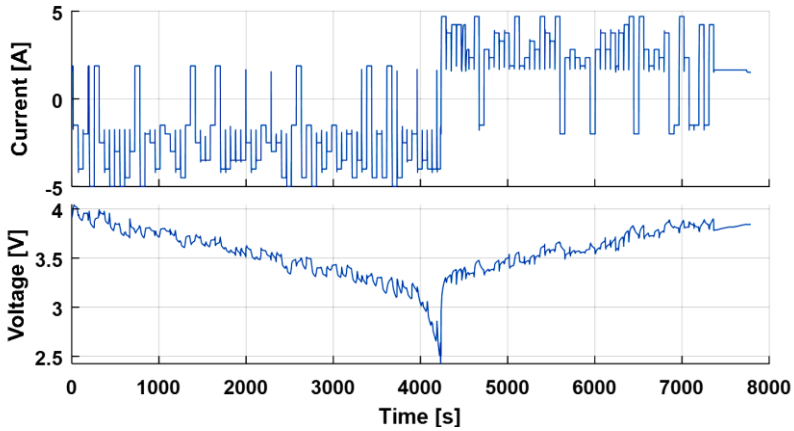

Figure 3.10: First-two dynamic load profiles of the ageing cycles applied for model training and validation. a: dynamic current profile; b: measured voltage

The measured voltage of the dynamic varying load profile is corrupted by some high-frequency noise of the order of 2mV and irregular spikes of up to 80mV that result from a rapid change of the load input. To avoid the impact of this noise on the classifier, the measured voltage data is smoothened using the moving average function with a smoothing factor of 0.01.

The training dataset consists of the $X(n) \in \mathcal{R}^{5\times N}$ feature variables and $Y(n) \in \mathcal{R}^{5\times N}$ output. The matrix rows correspond to the five (5) features and the five (5) classes respectively. N corresponds to the number of training data points which is the number of buffers. The original dataset is sampled at 1 second rate while the buffer has a time length of 40 seconds. Some information may be lost in the long timespan between the buffer intervals. Also, the initial SOC of a cell may vary in practice. Considering these limitations, the model training is enhanced by repeating each ageing cycle with a moving window that is shifted at an interval of 10 seconds.

The 118 dynamic profiles were used for the model training. That results in 77608 buffers, which is 90% of the entire buffers extracted from the profile. The dynamic load profiles are polarised to either charge or discharge the cell for each given cycle.

The training and validation results are analysed with the help of the confusion matrix. Figure 3.11 shows the confusion matrix of the trained model. The columns

of the matrix are the five (5) target or true classes. The rows are the predicted classes. The diagonal cell corresponds to the buffers that are correctly classified. The off-diagonal cells are the misclassified buffers. The number of observations is shown in each cell. The last column shows the precision of prediction per class. In other words, it shows the percentage of consistency of prediction with the true value for each class. The last row shows the percentage of each class that is correctly classified. This is also known as the true positive rate, TPR. The total accuracy is shown in the bottom-right cell. The accuracy of the model in the training phase is 98.2%. This corresponds to an error of 1.8% which is equivalent to 1370 misclassified buffers over 77608 total training buffers.

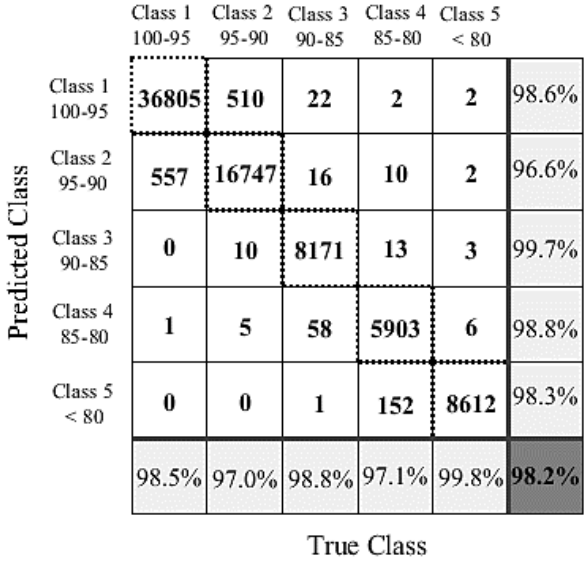

Figure 3.11: Confusion matrix for performance analysis of ANN-based classifier in the trained with LG 18650 MJ1 lithium-ion dataset.

After training the model, the model is validated with buffers from dynamic profiles that the trained model has not yet seen. To do this, the remaining 12 profiles corresponding to 10% of the entire buffers are given as inputs to the trained model. The performance of the model is then analysed with a confusion matrix as in Figure 3.12. The accuracy of the model in the validation phase is 96.2% and results in a total number of 317 misclassified buffers over 8273 buffers.

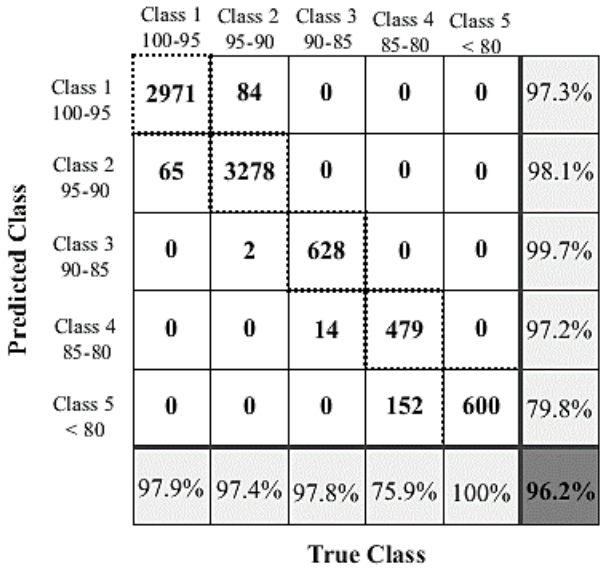

Figure 3.12: Confusion matrix for performance analysis of ANN-based classifier under dynamic changing load profile validation.

From Figure 3.12, it can be seen that the TPR of the classifier at validation is considerably high and in the range of 76% to 100%. This means that the percentage of the number of data points that are correctly classified is high. Also, the model precision is in the range of 80% to 99.7%, indicating that the model can be trusted to this degree.

3.2.2 Validation with the constant current constant voltage (CCCV) load profile

The constant current validation is performed with a CCCV load profile. The cell is charged with a constant current of 1.75 A until the voltage reaches about 3.8 V. The constant voltage mode is then activated until the minimum current of 0.3 A is reached. The consideration of this profile is relevant to provide validation of the model for constant current applications such as in the charging model of the plug-in electric vehicle. A CCCV profile of the first ageing cycle is shown in Figure 3.13.

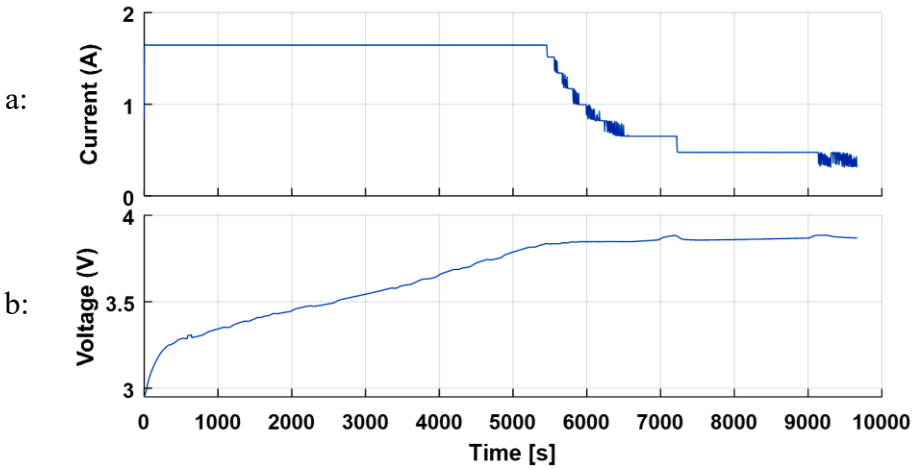

Figure 3.13: Constant load profile of the first ageing cycle for model validation a: constant current profile; b: measured voltage.

The constant current profile consists of 12 charge cycles and the features are extracted into 5879 buffers. The model performance under constant current charge conditions is shown in Figure 3.14 with a confusion matrix.

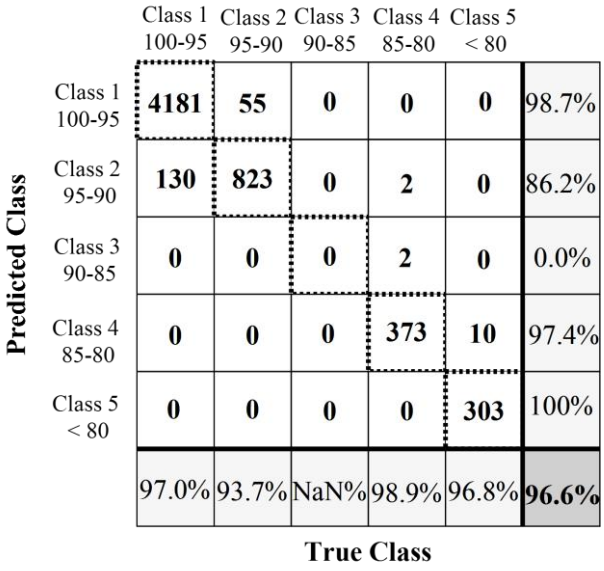

Figure 3.14: Confusion matrix for performance analysis of ANN-based classifier under constant charge current profile validation

The model accuracy under constant current charge condition is 96.6% with 197 misclassified buffers over 5879 total buffers. TPR is in the range of 93.7% to 98.9% while the precision is in the range of 86.2% to 100%. No buffer is in Class 3.

3.2.3 Validation with the step load profile

Here the step current profile is applied to validate the model for aggressive applications. The step current changes at 0.47A interval in the range of 0-4.23A. the step current profile consists of 11 cyclic charge profiles captured within 2700 buffers. The profile with the corresponding voltage is shown in Figure 3.15.

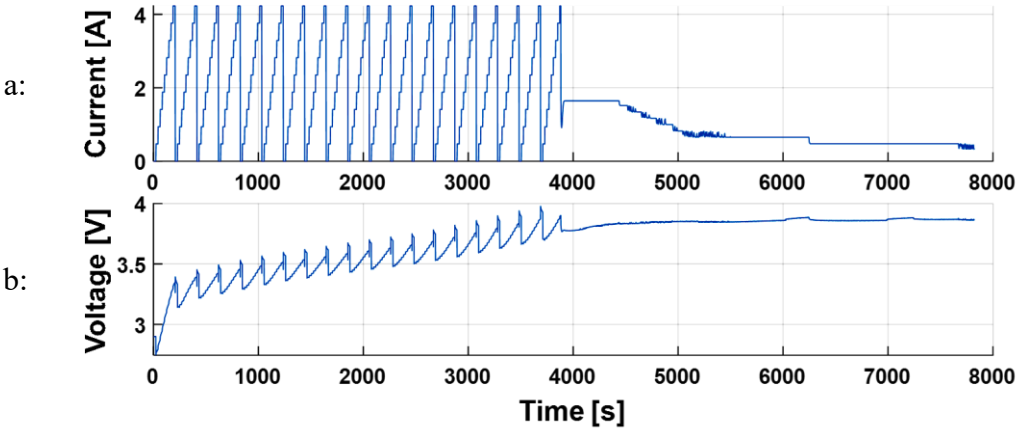

Figure 3.15: Model validation with step current profile of the first ageing cycle. a: step current profile; b: measured voltage.

The confusion matrix-based performance of the classifier under step current charge condition is shown in Figure 3.16. The accuracy of the classifier under step current charge condition is 93.8% with 163 buffers misclassified over 2700 total buffers. TPR is in the range of 82% to 100% while the precision is in the range of 84.8% to 100%.

Predicted Class \ True Class	Class 1 100-95	Class 2 95-90	Class 3 90-85	Class 4 85-80	Class 5 < 80	
Class 1 100-95	**1270**	**17**	**0**	**0**	**0**	98.7%
Class 2 95-90	**84**	**698**	**41**	**0**	**0**	84.8%
Class 3 90-85	**0**	**4**	**185**	**0**	**0**	97.9%
Class 4 85-80	**0**	**0**	**0**	**189**	**0**	100%
Class 5 < 80	**0**	**0**	**0**	**21**	**191**	90.1%
	93.8%	97.1%	81.9%	90.0%	100%	**93.8%**

Figure 3.16: Confusion matrix for performance analysis of ANN-based classifier under the step charging current profile validation.

The validation with the step current profile represents a relatively aggressive validation with respect to the other profiles. For this reason, a relatively lower performance is acceptable.

3.2.4 Model validation with new cell

The final validation of the model is performed with an entirely new cell of slightly similar specification. The experiment and analysis performed above are repeated for a Sanyo NCR 18650 GA Lithium cell. Although the Sanyo NCR cell shares a similar specification with the LG MJ1, their chemistries are different. The characteristics of the cell is given in Table 3.4.

Table 3.4: Nominal characteristics of cylindrical Sanyo NCR 18650 GA lithium-ion cell [78]

Cell chemistry		$LiNiCoAlO_2$
Nominal capacity (@ 0.2C, 4.2V-2.5V, 25°C)		3300mA
Nominal voltage		3.6V
Cut-off voltage		2.5V
Max. discharge current		10A
Cycle life (charge@1.5A, discharge@4A)		> 300 cycles
Charge Condition	Max. current	1C (3350mA)
	Max. voltage	4.2 ± 0.03 V
Operating Condition	Charge	0 - 40°C
	Discharge	-20 - 60°C
Mass		49.0g
Dimension	Diameter	18mm
	Height	65mm

The cell is aged in a similar procedure as demonstrated earlier with similar load profiles in a repeated pattern. The cell reached the SOH of about 70% after about 120 cycles. The SOH of the cell across the ageing cycle is shown in Figure 3.17.

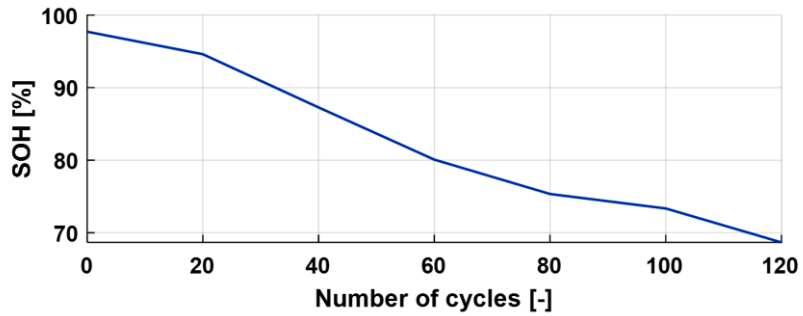

Figure 3.17: SOH of cylindrical Sanyo NCR 18650 GA lithium-ion cell across the ageing cycles

To extract the feature variable data for validating the neural network, the η_c and η_e are computed as 0.91 and 0.83 respectively to obtain the best fit between the charge and discharge SOH across the ageing cycles. This stage of validation applies only to the dynamic load profile. The feature variables are then computed as described earlier and applied as input to the trained classifier. The model performance is again analysed with a confusion matrix as in Figure 3.18. A total number of 4371 buffers are extracted from the dynamic load profile. About 4228 buffers are correctly classified while 143 buffers are wrongly classified. This results in 96.7% total accuracy of the model.

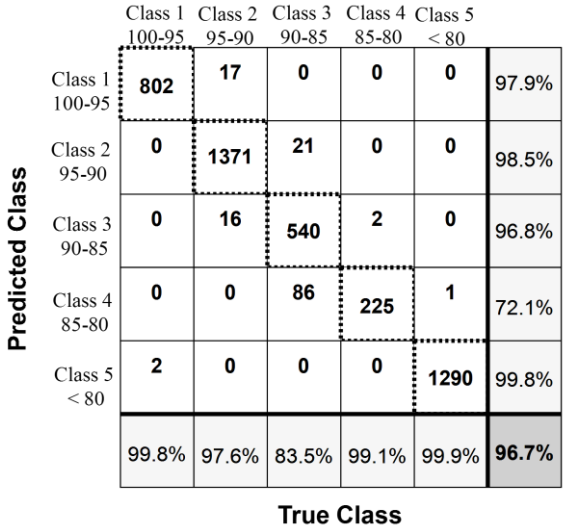

Figure 3.18: Confusion matrix for model validation with NCR 18650 GA lithium-ion cell under dynamic load profile.

These results of the training and the various validations of the classifier model are summarized in Figure 3.19 including information on the model precision, the TPR, and the total accuracy.

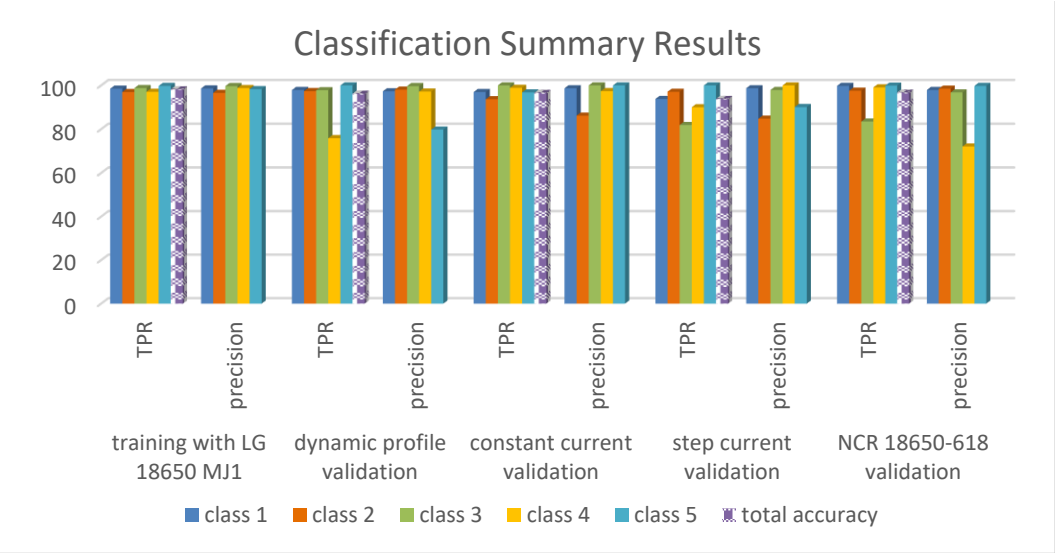

Figure 3.19: Result summary of the training and validation of the classifier indicating the TPR, precision per class and the total accuracy of the classifier according to the confusion matrices.

The analysis of the limitations of the estimation model based on the sensor noise is deferred to the next chapter.

To compare the proposed model with the state of the art, it was observed that only a few authors have reported the SOH estimation under dynamic load conditions employing classification. [13] reported the estimation of SOH under such conditions using a similar classification approach. However, SOH was estimated only in the dynamic discharge modes and with a synthetic dataset. The resulting model offers an accuracy of 97.5%. In the more realistic proposed model designed with a real dataset, the accuracy of 96.2% is obtained when validated under dynamic profiles according to Figure 3.12.

The classifier is designed, trained and validated on Matlab/Simulink 2020b that is equipped with a Neural network toolbox. After the training and validation, the trained classifier is deployed to a Texas F28379D microcontroller unit (MCU) target. The real-time execution speed is estimated by a PIL simulation to verify the model for online applicability. Given some sampling points of the feature variables as input from Simulink software, the model is simulated in the MCU. The model execution speed is verified as 8.34 µs in real-time, and with a negligible CPU occupation. In comparison, the PL-ELM performs a similar operation by regression with an execution speed of 93 µs [79]. In the real implementation, the classification algorithm is periodically triggered to extract the feature variables of the classifier in the buffer using information from an installed battery. These features are then applied as input to the trained classifier for predicting the battery SOH.

3.3. Conclusions and Recommendation

Analysis of battery SOH under dynamic load conditions is essential for the design of high fidelity estimation model. This however has been sparingly addressed in the literature. In this work, the SOH of a lithium-ion cell is analysed and estimated under dynamic load conditions by implementing an ANN-based classifier. This approach minimises the time history dependency and the need for continuous initialization of the model.

The SOH is experimentally characterised by the cell's voltage, SOC, and SOE at room temperature. An ANN-based classifier model is trained using features that are extracted from the characterising variables. These features include the instantaneous values of SOC and SOE, and the relative value of voltage, SOC, and SOE across the buffer of defined time length.

The trained model is validated for application under different scenarios, including dynamic load conditions, constant load conditions and step load conditions. The performance of the resulting validated model is analysed with matrices and the accuracy of the model are 96.2%, 96.6% and 93.8% for the respective load conditions. The model is further validated for use on other cells that have similar specifications. The results show that an accuracy of 96.7% is possible under dynamic load conditions.

Finally, the model is validated for online applicability through PIL simulation. An average execution time of 8.34 μs and a negligible CPU occupation is verified with a Texas F28379D microcontroller unit (MCU) board. This makes the model suitable for online automotive applications where computational resources impose a constraint.

For future work, it was noticed that the model poorly classifies buffers whose SOH are very close to the boundary of two classes. For instance, buffers whose true SOH are close to 95% (say 95.01%) may partly be misclassified as class 2. Improving the precision of the model for such cases will be the focus of future work. Also, SOH is impacted by temperature. However, this model is validated only for ambient room temperature. This limits its application to only such a condition. It will be of useful research interest to further validate the model over a wider range of temperature conditions. Lastly, the model has been validated for the dynamic load of frequency in the range of 5.8×10^{-6} to 2.9 rad/s. It will be interesting to validate the model at higher frequency load conditions.

Chapter 4. Battery and Electro-Thermal Model

The powertrain of the HEVs is equipped with a battery pack to serve as an energy reservoir for electrical energy. A cell model is designed and experimentally validated with a dataset from Sanyo NCR 18650 GA lithium-ion cell which has a nominal capacity of 3.3 Ah and a nominal voltage of 3.6 V. The cell model forms the basis for designing the SPKF. Also, the state information is derived from the cell model and applied in the design of the HEV energy optimization model to ensure that the operating limits of the battery are not violated. A model of the battery pack is obtained by extrapolation of the cell model. The specifications of the cell are provided in [80] as provided in Table 3.4.

4.1. Electro-Thermal Model

Developed according to the enhanced self-correcting (ESC) model procedure [8], the cell electrical model is integrated with the cell thermal model to obtain the electro-thermal cell model. The cell model is then used as a building block for the battery pack model shown in Figure 4.1. The dynamic process of the ESC computes the voltage losses associated with the battery power request P_{bat}. The electric ESC model is developed from the combination of the dynamic process and the v_{oc}. The thermal model is developed from the computed voltage losses. The developed electro-thermal model of the lithium-ion cell is validated experimentally at an ambient environmental temperature of 20°C and extrapolated to obtain a battery pack.

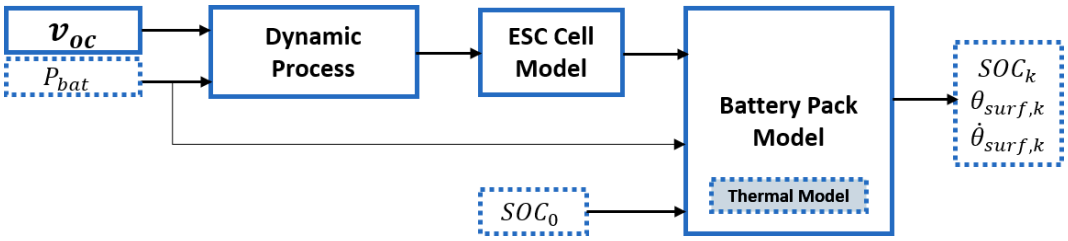

Figure 4.1: Schematic component of the battery pack electro-thermal model. The variables in dotted blue and grey blocks are the inputs and the states of the battery model respectively.

4.1.1 Cell electric model

The electro-thermal model of the lithium cell is developed and validated experimentally at an ambient environmental temperature in [4]. The equivalent circuit of the electric model according to [8] is shown in Figure 4.2. The circuit consists of a single parallel resistor-capacitor (RC) branch connected in series with a resistor and a Warburg impedance. Given a current request i_k (derived from battery power request P_{bat}) to the cell model, the diffusion-resistor current $i_{R1,k}$ passes through the parallel resistor. The single parallel RC branch with R_1 and C_1 model the relatively high frequency diffusion loss due to mass transfer, and the activation loss due to charge transfer. R_0 models the Ohmic internal resistance of the cell. The low frequency Warburg impedance models the hysteresis losses [81].

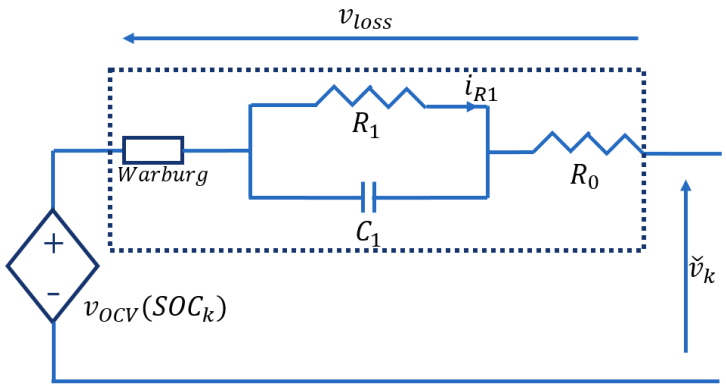

Figure 4.2: Equivalent circuit that describes the dynamic model designed for terminal voltage and voltage loss prediction [8].

The v_{oc} is known to be a function of temperature and SOC. However, it is considered here only as a function of SOC assuming ambient environmental temperature. The v_{oc} of the cell under consideration is provided on the datasheet [80]. Figure 4.3 shows the voltage variation across SOC under open and closed-circuit conditions.

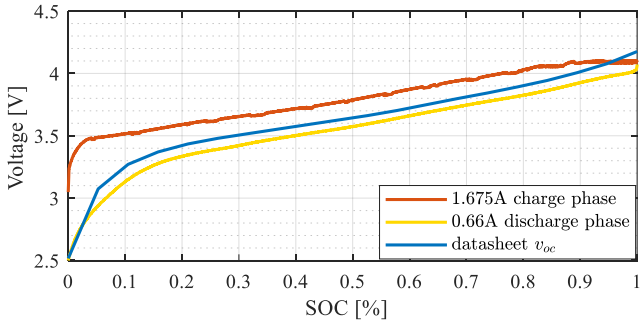

Figure 4.3: The open-circuit and closed-circuit voltages across SOC in charge and discharge phases. The open-circuit voltage from the datasheet is between the measured terminal voltage in the charge and discharge phases.

The middle blue curve shows the v_{oc} as a function of SOC, as acquired from the datasheet. The red curve is the closed-circuit voltage at a constant charge load of 1.675 A. The yellow curve is the closed-circuit voltage at a constant discharge load of 0.66 A. It can be seen that the v_{oc} taken from the datasheet approximates the true v_{oc} at the mean of the closed-circuit voltages of the charge and discharge phases. The larger deviation of the charge phase results from the relative higher C-rate with respect to the discharge phase.

The cell electric model computes the state of the charge (SOC) at every time step k by Coulomb counting as in Equation 4.1.

$$SOC_{k+1} = SOC_k - \frac{\eta_c \, i_k T_s}{C_{max}} \tag{4.1}$$

where i_k is the requested current – positive at discharge; A sampling time $T_s = 0.5$ seconds is applied to the model; C_{max} [Ah] is the maximum releasable capacity when the cell is fully charged and η_c is the cell Coulombic efficiency in the charge phase [72,73].

Other states of the cell model include the diffusion-resistor current i_{Rj} and the hysteresis voltage h. i_{Rj} expressed in Equation 4.2 and h in Equation 4.3 [8].

$$i_{R_1,k+1} = \; exp\left(\frac{-T_s}{\tau_{RC}}\right) i_{R_1,k} + \left(1 - exp\left(\frac{-T_s}{\tau_{RC}}\right)\right) i_k \tag{4.2}$$

where $\tau_{RC} = R_1 C_1$ is the time constant of the RC circuit shown in Figure 4.2.

$$h_{k+1} = exp\left(-\left|\frac{\eta \, i_k \, \gamma T_s}{C_{max}}\right|\right) h_k + \left(exp\left(-\left|\frac{\eta \, i_k \, \gamma T_s}{C_{max}}\right|\right) - 1\right) sgn_k \tag{4.3}$$

The non-dimensional parameter γ determines how quickly the hysteresis state changes with the SOC. sgn_k is a sign function, i.e. 1 for positive current input, –1 for negative input and zero otherwise.

The predicted cell terminal voltage $\check{v}$ results from the summation of the open circuit voltage v_{OC} and the voltage loss contributions v_{loss} as in Equation 4.4.

$$\check{v}_k = v_{OC}(SOC_k) \; + \; v_{loss,k} \tag{4.4}$$

The v_{OC} is a function of SOC. The $\check{v}$ is the cell terminal voltage predicted from an electric model. The v_{loss} models the voltage losses that result from the contributions of the cell's internal resistance, diffusion resistance and hysteresis. The v_{loss} contributions are expressed in Equation 4.5.

$$v_{loss,k} = M_a h_k + M_0 \, sgn_k \; - \; \sum\nolimits_j R_j i_{Rj,k} \; - R_0 i_k \tag{4.5}$$

M_a is the maximum absolute analog hysteresis voltage at ambient temperature; M_0 is the instantaneous hysteresis voltage; h is the hysteresis voltage; R_j is the parallel branch resistance. The parameters of the model M_a, M_0, R_j, and R_0 appear linearly according to Equation 4.6 and are computed by least square approximation.

$$\begin{bmatrix} v_{loss,1} \\ v_{loss,2} \\ \vdots \\ v_{loss,N} \end{bmatrix} = \begin{bmatrix} h_1 & sgn_1 & -i_{R_j,1}^T & -i_1 \\ h_2 & sgn_2 & -i_{R_j,2}^T & -i_2 \\ & & \vdots & \\ h_N & sgn_N & -i_{R_j,N}^T & -i_N \end{bmatrix} \begin{bmatrix} M_a \\ M_0 \\ R_j \\ R_0 \end{bmatrix} \tag{4.6}$$

where N is the number of data points of the experimental dataset. Refer to Table 4.1 for the electro-thermal model parameters.

M_0 can be assumed to be negligible. However, this is not often the case for all SOH of the cell as will be seen in the next chapter.

Table 4.1: List of electrical and thermal model parameters with the estimated values

	Variable	Units	Value
Electric Model	Max absolute analogue hysteresis voltage at ambient temperature, M_a	-	0.017
	Instantaneous hysteresis height, M_0	-	1.0×10^{-8}
	Instantaneous series resistor, R_0	Ohms	0.024
	Parallel branch resistance, R_j	Ohms	0.018
Thermal Model	Specific heat capacity, c_p	J/kg K	1200
	Thermal resistance, R_{conv}	K/W	14.6
	Cell mass, m_{cell}	kg	48.5×10^{-3}

The dynamic current profile used for data collection during the experiment is applied as input to the model to compute v_{loss} according to Equation 4.5. This profile consists of a sequence of random charge and discharge current values applied in the range of -4.5 [A] and +4.5 [A]. The current profile and v_{loss} are shown in Figure 4.4.

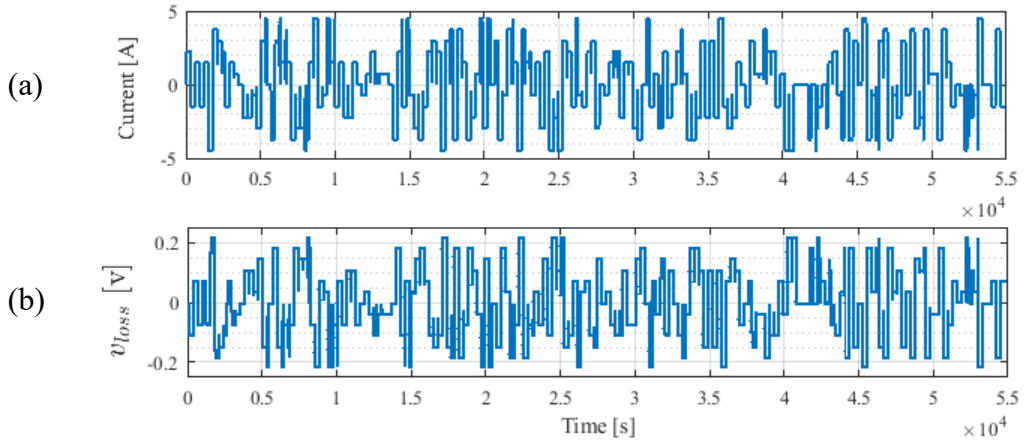

Figure 4.4: Simulation of cell electro-thermal model. a: dynamic current profile b: dynamic voltage loss.

4.1.2 Cell thermal model

When the v_{loss} is computed, the thermal component of the electro-thermal model is computed by lumped parameter approach. The dynamic thermal model is designed considering only the heat transfer by convention while neglecting the conductive component. The heat source, P_{loss} of the thermal model is derived from v_{loss}, and a thermal model is derived from an energy balance equation of a lumped capacity model [82]. Using a forward Euler discretization, θ_{surf} of the cell is computed according to Equation 4.7. It is assumed that the cell is cooled by natural convection without active cooling system.

$$\theta_{surf,k+1} = \theta_{surf,k} + \frac{T_s}{c_p \cdot m_{cell}} \left(P_{loss,k} - \frac{\theta_{surf,k} - \theta_{amb}}{R_{conv}} \right) \tag{4.7}$$

T_s is the sampling time; c_p is the cell's specific heat capacity; m_{cell} is the cell mass; θ_{amb} is the ambient temperature; $R_{conv} = (h_{conv} \times A_{cell})^{-1}$ is the thermal resistance by convection; h_{conv} is the thermal convention coefficient; and A_{cell} is the cell surface area. The thermal model parameters are highlighted in Table 4.1.

4.2. Cell Model Validation

The experiment setup for the battery model validation is described in Section 3.1.1. The experimental data consisting of current input, battery surface temperature [°C] and voltage [V] outputs were collected at room temperature from NCR 18650 GA cell. The model is validated under different load conditions, including constant

current discharge, step current discharge and dynamic charge-discharge load conditions.

A constant current of 10 A corresponding to 3 C-rate is applied to completely discharge the cell. The estimated and the measured voltages under constant load conditions are compared as in Figure 4.5b. The model temperature is equally validated in Figure 4.5c.

(a)

(b)

(c)

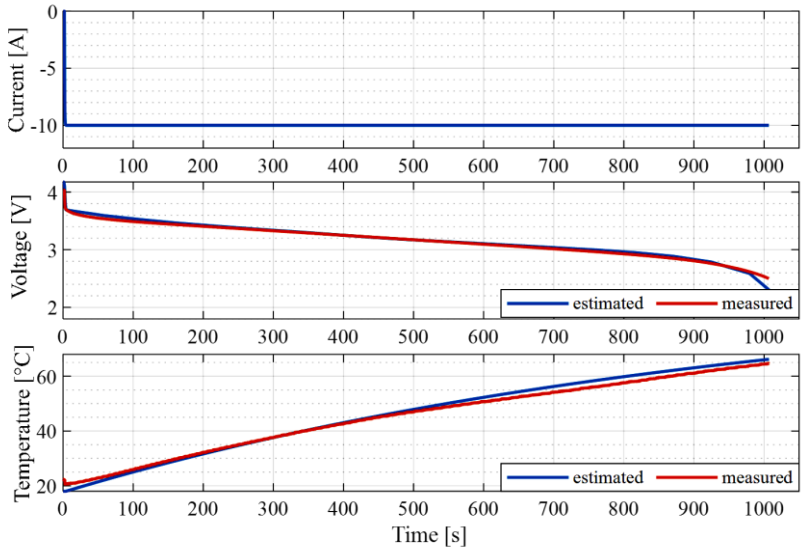

Figure 4.5: Electro-thermal model experimental validation under constant current load condition. a: the constant current profile; b: estimated and measured voltage compared; c: estimated and measured temperature compared.

The model is further validated under step discharge load conditions. A sequence of current steps is applied to span a range of 0 A to 10 A in 5 steps. This sequence is repeated periodically to completely discharge the cell. The estimated and the measured voltages under discharge step load conditions are compared as in Figure 4.6b. The model temperature is validated as in Figure 4.6c.

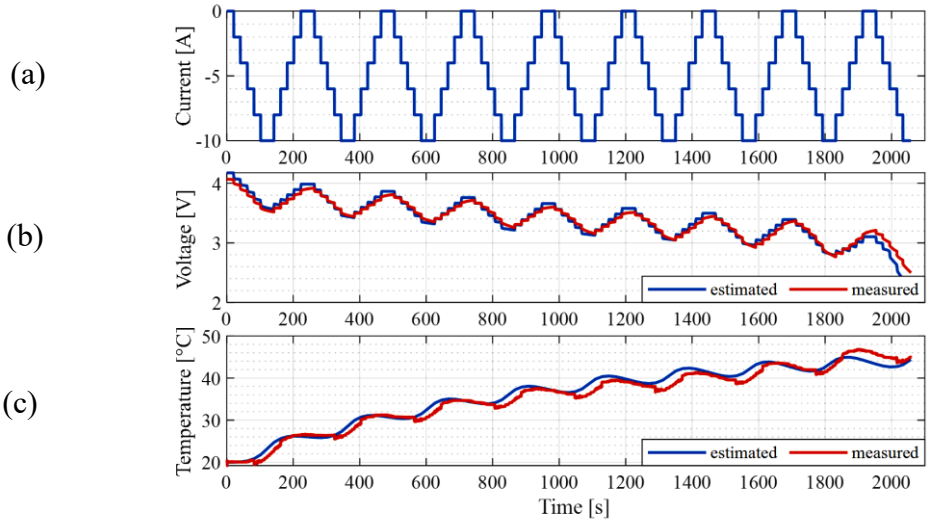

Figure 4.6: Electro-thermal model experimental validation under discharge step load condition. a: the step current profile; b: estimated and measured voltage compared; c: estimated and measured temperature compared.

Finally, the model is validated under dynamic load conditions. The dynamic current profile is composed of a sequence of charge and discharge current in the range of -4.5 to 4.5 [A]. The estimated and the measured voltages are compared as in Figure 4.7b. The thermal model was equally validated and the result is shown in Figure 4.7c.

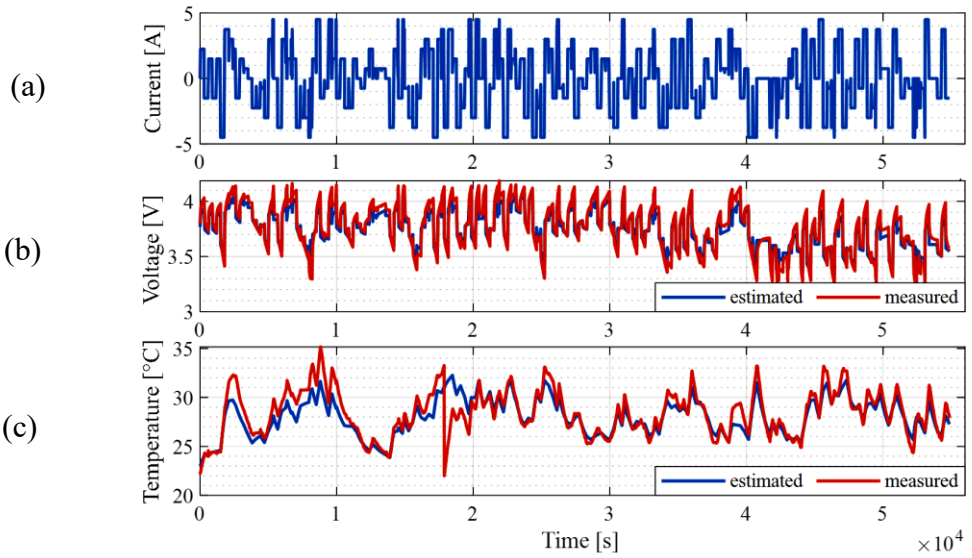

Figure 4.7: Electro-thermal model experimental validation under dynamic load condition. a: the dynamic current profile; b: estimated and measured voltage compared; c: estimated and measured temperature compared.

The limitation of the developed cell model is analysed here based on the input noise and the model uncertainty. The input noise analysis can be extended to the SOH estimation described in Chapter 3 since the same current measurement device has been used in both cases. Two different multimeters were used for input current acquisition. Figures 4.8a and 4.8b show the distribution of noise from the two multimeters. The Fluke multimeter offers improved precision and has been adopted to minimise the model uncertainty. The noise distribution of the current measurement with the Fluke multimeter is shown in Figure 4.8b. By using this multimeter, the 99.7% confidence interval (3×standard deviation) of the noise distribution was improved from ± 0.06 A to ± 0.0172 A with fewer outliers in the lower and upper fences. The lower fence is computed as $Q_1 - 1.5 \times$ interquartile range (IQR) while the upper fence $Q_3 + 1.5 \times$ IQR. The model performance and uncertainty are analysed with the current input measured with the Fluke multimeter. Figure 4.8c shows the distribution of voltage estimation uncertainty while Figure 4.8d shows the distribution of temperature estimation uncertainty.

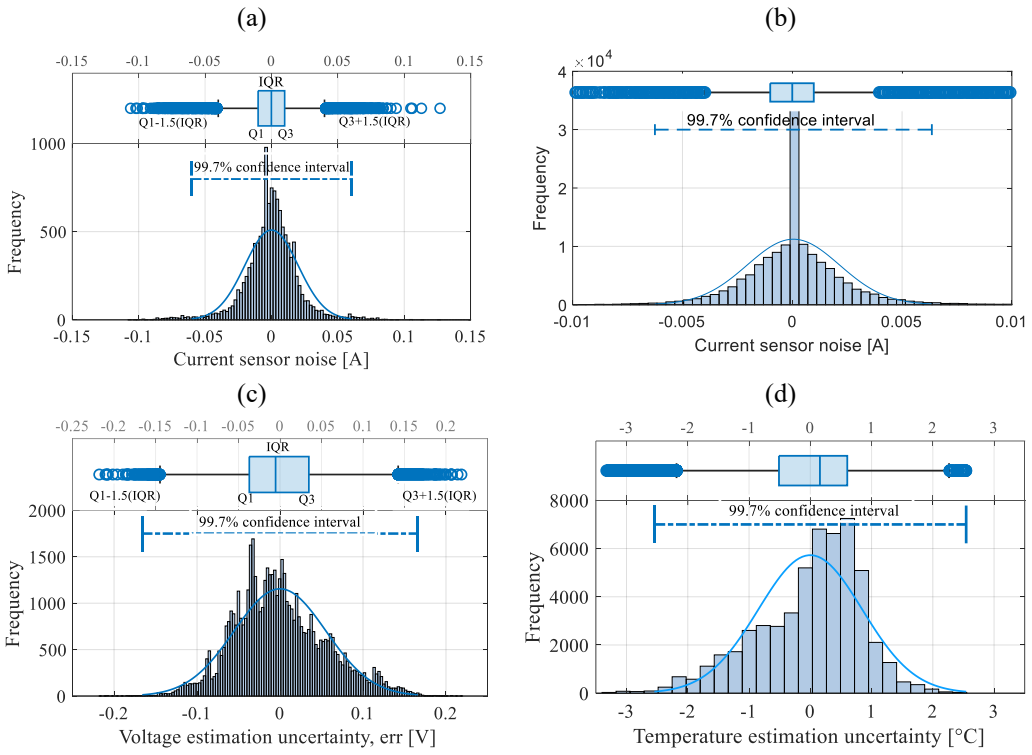

Figure 4.8: Input current noise distribution and model uncertainty (a) low precision current noise distribution; (b) Fluke multimeter current noise distribution; (c) voltage estimation uncertainty from model deviation and measurement noise; (d) temperature estimation uncertainty from model deviation and measurement noise.

Putting into consideration the sensor noise and the model inaccuracy, the model can be trusted to estimate voltage with uncertainty in the range of ± 0.165 V within a 99.7% confidence interval. The voltage measurement cell board has a maximum accuracy of ±15mV. On the other hand, temperature estimation can be trusted with an uncertainty of ± 2.5 °C within a 99.7% confidence interval.

4.3. Battery pack

The configurable battery pack model is developed from the building block of the electro-thermal model of a single cell according to the work of [8]. The pack is a series module pack (SMP) composed of modules that are connected in series. Each of the modules consists of cells connected in parallel modules, otherwise known as parallel cell modules (PCM). To design a 1.9 kWh battery, a 14s6p configuration is used. This configuration consists of 6 parallel cells in each of the 14 modules that are connected in series.

4.3.1 Parallel Cell Module (PCM)

With the single-cell model designed and validated, the model forms a building block for developing the PCM and the SMP for further integration in a complete vehicle model. A battery PCM consists of cells that are connected in parallel while the SMP consists of battery modules that are connected in series to make a battery pack. A 14s6p battery pack configuration entails 14 SMP and 6 PCM. The parallel cell configuration is often useful for increasing the energy capacity of the battery pack, especially for various high-energy applications.

The current i_k through each cell in a PCM can be computed from Equation 4.8 if the module voltage v can be derived. By Kirchhoff's law, the sum of all the individual current $I_{j,k}$ that passes through a module is equal to the pack's current I_k. Also, the voltages at the terminal of all the cells in the module are equal. The cell voltage in Equation 4.8 has two contributions: the instantaneous voltage that changes instantly with the current and the non-instantaneous state voltages v_f.

$$v_k = v_{f,j,k} - i_k R_{0,j} \tag{4.8}$$

R_0 is the instantaneous resistance modified to accommodate the losses of the cell connection terminals. The sum of the current in each module $I_{j,k}$ can be computed from Equation 4.9.

$$I_{j,k} = I_k = \sum_{j}^{p} \left(\frac{v_{f,j,k} - v_k}{R_{0,j}} \right) \tag{4.9}$$

p is the number of parallel branches in the module and j is the branch (module) index. By simultaneous computation of Equations 4.8 and 4.9, the current through each cell in the module and the voltage can be derived. The modules are connected in series to develop an SMP. To analyse a 48V, 0.9 kWh battery pack, a 14s6p configuration is used.

The temperature distribution within the battery pack was evaluated based on the variation of the SOC and the capacity of the cells within the battery pack. The battery pack was simulated to show these variations. Figure 4.9a shows the variation of temperature when the initial SOC varies from 0.85 to 0.95, assuming an equal capacity of 3.0Ah for the individual cells. Figure 4.9b shows the variation of temperature when the cell capacity varies from 2.7Ah to 3.0Ah, assuming equal initial SOC of 0.95 for all cells.

(a)

(b)

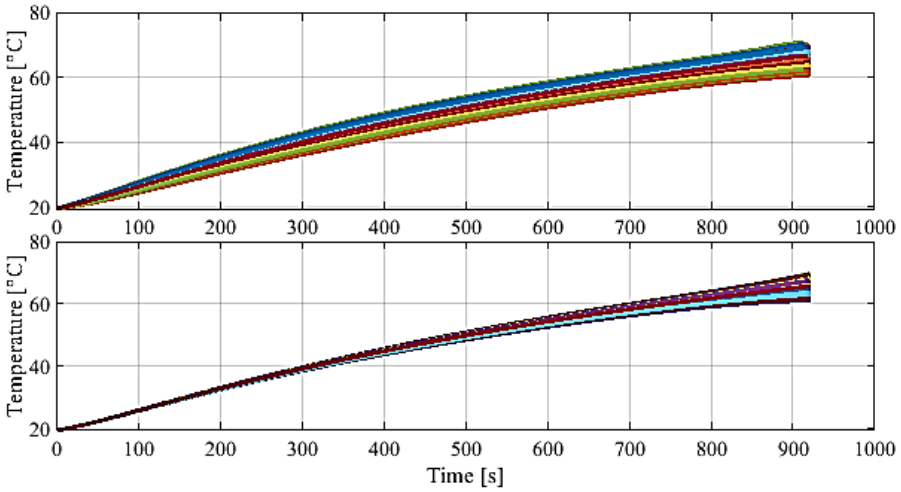

Figure 4.9: Surface temperature variation of the cells in the 14s6p battery pack configuration. a: initial SOC variation between 0.85 - 0.95, b: capacity variation between 2.7Ah – 3.0Ah.

Based on the result of the simulation shown in Figure 4.9, the maximum temperature of the battery pack is in the range of 60°C to 70°C at the end of the tests. The temperature variation is larger for varying SOC than for varying capacity.

Chapter 5. State of Charge Estimation

To prevent thermal runaway and to enhance cell longevity, it is necessary to respect the operating conditions of the cells. Accurate measurement of SOC can help to prevent overcharge and over-discharge which could accelerate cell ageing. Also, the battery performance is improved by minimising conservativeness in the operating range of the cell with a reliable confidence interval. In addition, a consistent and dependable estimation model is developed and validated with dynamic profiles, and over-design can be avoided by permitting aggressive usage within the design limit. The SPKF analysed in this section is developed with the cell model that was discussed in Chapter 4.

The nonlinear SPKF is equipped with an update or feedback mechanism to minimise the effect of measurement noise and model deviation in SOC estimation. This feedback mechanism is however limited by cell ageing. Our goal in this chapter is to enhance SOC estimation by integrating the benefits of the adaptive mechanism of SPKF and the time-independent ANN-based SOH estimator. This approach improves the accuracy of SOC estimation across the cycle life of the cells. The model is validated experimentally under dynamic load conditions using the dataset from LG MJI 18650 lithium-ion cells.

5.1. Methodology

The SOC has been computed so far by Coulomb counting. This procedure however has some drawbacks. Since Coulomb counting is not equipped with any feedback, it integrates all the errors that corrupt the true current value. The true current I_{true} can be corrupted by the error due to sensor bias I_{bias}, sensor noise I_{noise}, sensor nonlinearity I_{nonlin}, self-discharge current I_{sd}, and leakage current I_{leak} [8]. These contributions make up the measured current I_{meas} as in Equation 5.1.

$$I_{meas}(t) = I_{true}(t) + I_{bias}(t) + I_{noise}(t) + \dots + I_{nonlin}(t) + I_{sd}(t) + I_{leak} \quad (5.1)$$

It is desired to accurately estimate the SOC of cells in the battery over the cycle life. The cell SOC is estimated with high accuracy with SPKF giving measured current input and terminal voltage output at ambient room temperature. However, as the battery ages, the parameters changes, the model error increases and the SPKF lose its performance. Based on the knowledge of the SOH, these parameters are updated and SOC can be estimated with SPKF over the battery cycle life.

5.1.1 SOC Estimation with SPKF

To design an SPKF, some sigma points $\mathcal{X}$ are deterministically defined such that the weighted mean and covariance of these points are exactly equal to the mean $\bar{x}$ and covariance $\sum \tilde{x}$ of the input random variable to nonlinear system function. These points are then individually passed through the nonlinear function, resulting in a transformed set of output sigma points У. The mean $\bar{y}$ and the covariance $\sum \tilde{y}$ of the output's random variables are then approximated by the weighted mean and covariance of these transformed sigma points У. In general, the input randomness is represented by sigma points, these sigma points are propagated through the nonlinear function, and then the predicted state $\hat{x}_k^-$ is computed as the average of the output sigma points. The sources of the randomness include the state, the process noise and the measurement noise. An augmented state x_k^a and the covariance is then defined to capture the randomness at k time instant as in Equation 5.2.

$$x_k^a = \begin{bmatrix} x_k \\ w_k \\ v_{k+1} \end{bmatrix} \qquad \Sigma_{\tilde{x}_k}^a = \begin{bmatrix} \Sigma_{\tilde{x}_k} & 0 & 0 \\ 0 & \Sigma_w & 0 \\ 0 & 0 & \Sigma_v \end{bmatrix} \tag{5.2}$$

Where x_k are the states of the electrical components of the battery model described in Equations 4.1, 4.2 and 4.3 with the input current i_k replaced with $u_k + w_k$. The current input noise is modelled as the process noise denoted by w_k. The noise distribution of the current input is shown in Figure 4.8b with an SD of ±0.0057 A and the frequency is in the range of 4.3×10^{-5} to 3.1 rad/s. For conservativeness, however, the model input noise has been set to an SD of 0.1414 A to guarantee the stability of the model over wider noise variation. The output of the cell model is the measured cell terminal voltage measured by the cell board which has a maximum accuracy of 15mA. The output noise is modelled with v_k and the estimation uncertainty is shown in Figure 4.8c. The SPKF assumes a noise with normal distribution and a zero mean. The noise distribution in Figures 2.7 and 4.8a-c are good approximations of normal distributions. To guarantee the

performance of SPKF across different noise frequencies, white noise can be assumed at the input. This can be achieved by applying a shaping filter with white noise input to shape the model input noise. This procedure is demonstrated in [8]. However, it has not been applied in this work.

The augmented sigma-point is defined as in Equation 5.3.

$$\mathcal{X} = \{\bar{x},\ \bar{x} + \gamma\sqrt{\Sigma_{\tilde{x}}},\ \bar{x} - \gamma\sqrt{\Sigma_{\tilde{x}}}\} \tag{5.3}$$

where γ is a weighting constant for tuning the performance of SPKF.

The design of SPKF for SOC estimation using the battery model is described in the following steps. The first step is the state prediction is defined in Equation 5.4.

$$\hat{x}_k^- = \sum_{i=0}^{p} \alpha_i^{(m)} f(\mathcal{X}_{k-1,i}^{x,+}, u_{k-1}, \mathcal{X}_{k-1,i}^{w,+}) = \sum_{i=0}^{p} \alpha_i^{(m)} \mathcal{X}_{k,i}^{x,-} \tag{5.4}$$

where $\alpha_i^{(m)}$ is the weighting factor defined according to the central-difference strategy [83,84]. The $f()$ is a function of the input and the posterior sigma points of the respective states and the sensor noise, all in the previous time step. $\mathcal{X}_{k,i}^{x,-}$ is the predicted sigma point in the current time step.

The second step is the error covariance prediction step which is expressed in Equation 5.5.

$$\Sigma_{\tilde{x},k}^- = \left(\widetilde{\mathcal{X}}_k^{x,-}\right) diag\left(\alpha^{(c)}\right) \left(\widetilde{\mathcal{X}}_k^{x,-}\right)^T \tag{5.5}$$

where $\alpha_i^{(c)}$ is the weighting factor defined according to the central-difference strategy. The sigma point error $\widetilde{\mathcal{X}}_k^{x,-}$ is computed as the difference between the predicted sigma point of the state and the predicted state.

The last prediction step is the system output prediction $\hat{y}_k$. The output prediction is computed according to Equation 5.6

$$\hat{y}_k^- = \sum_{i=0}^{p} \alpha_i^{(m)} h(\mathcal{X}_{k,i}^{x,-}, u_k, \mathcal{X}_{k,i}^{v,+}) = \sum_{i=0}^{p} \alpha_i^{(m)} \mathrm{y}_{k,i} \tag{5.6}$$

The $h()$ is a function of the input, the predicted sigma points of the states and the sensor noise, all in the current time step.

The remaining steps of the SPKF are applied to update the model states. First, a time-varying Kalman gain matrix L_k is derived according to Equation 5.7

$$L_k = \Sigma_{\tilde{x}\tilde{y},k}^{-} \Sigma_{\tilde{y},k}^{-1} \tag{5.7}$$

The $\Sigma_{\tilde{x}\tilde{y},k}^{-}$ is the covariance associated with the state error and output error while $\Sigma_{\tilde{y},k}^{-1}$ is the covariance of the output error. Using L_k, the state estimate is updated thus:

$$\hat{x}_k^{+} = \hat{x}_k^{-} + L_k(y_k - \hat{y}_k) \tag{5.8}$$

where y_k is the true output voltage and $\hat{y}_k$ is the predicted output voltage.

The final step of the SPKF is to update the covariance. The step is computed by optimal formulation such that the error variance should be reduced as in Equation 5.9. This is because the second part of the equation on the right-hand side is positive-semi-definite.

$$\Sigma_{\tilde{x},k}^{+} = \Sigma_{\tilde{x},k}^{-} - L_k \Sigma_{\tilde{y},k} {L_k}^T \tag{5.9}$$

For more details on the implementation of SPKF, readers are advised to refer to [8,83,84].

5.1.2 Improving SOC Estimation with SOH

At the BOL of the cell, the performance of SPKF for SOC estimation is optimum. The battery model is designed with the parameters of Class 1 SOH as given in Table 5.1. As the battery ages, the parameters of the battery also change. To maintain the performance of SPKF, the parameters of the battery model should be updated as the battery ages. The parameters are estimated using the ESC procedure described in Section 4. These parameters are defined for each class of the battery SOH such that on estimation of the SOH, the parameters are updated accordingly. The Classes 1-5 are the SOH classes defined in Section 3.1.2.

Table 5.1: Estimated cell (LG MJI 18650 lithium-ion cells) parameters over different SOH classes

Parameter	Class 1 100%-95%	Class 2 95%-90%	Class 3 90%-85%	Class 4 85%-80%	Class 5 < 80%
Cell Capacity, C_{max} [Ah]	3.09	2.92	2.76	2.65	2.38
Max absolute analog hysteresis voltage at ambient temperature, M_a	1×10^{-8}	0.029	0.031	0.034	0.078
Instantaneous hysteresis voltage, M_0 [V]	1×10^{-8}	1×10^{-8}	1×10^{-8}	1×10^{-8}	0.002
Instantaneous series resistor, R_0 [Ohm]	0.042	0.044	0.047	0.05	0.06
Parallel branch resistance, R_i [Ohm]	0.032	0.024	0.033	0.037	0.027
RC time constant, τ_{RC} [seconds]	42.08	37.82	40.74	24.98	49.86

It can be observed from Table 5.1 that as expected, the cell SOH shows some correlations with C_{max} and R_0. This justifies the reason why these parameters are often used for the prediction of SOH. While C_{max} decreases as SOH decreases, R_0 increases. The M_a parameter also increases consistently with SOH although it is not commonly used as an SOH predictor.

The SOH estimated with the ANN classifier is explained in Section 3. Figure 5.1 shows the scheme of the SOC estimation model. Due to the slow dynamic of SOH, the SOH algorithm is triggered on an hourly basis and the class of the estimated SOH is maintained until the next time step. The SOC estimation algorithm, on the other hand, is triggered every second-time step. The parameters of the battery model that corresponds to the SOH class are applied for the SOC estimation.

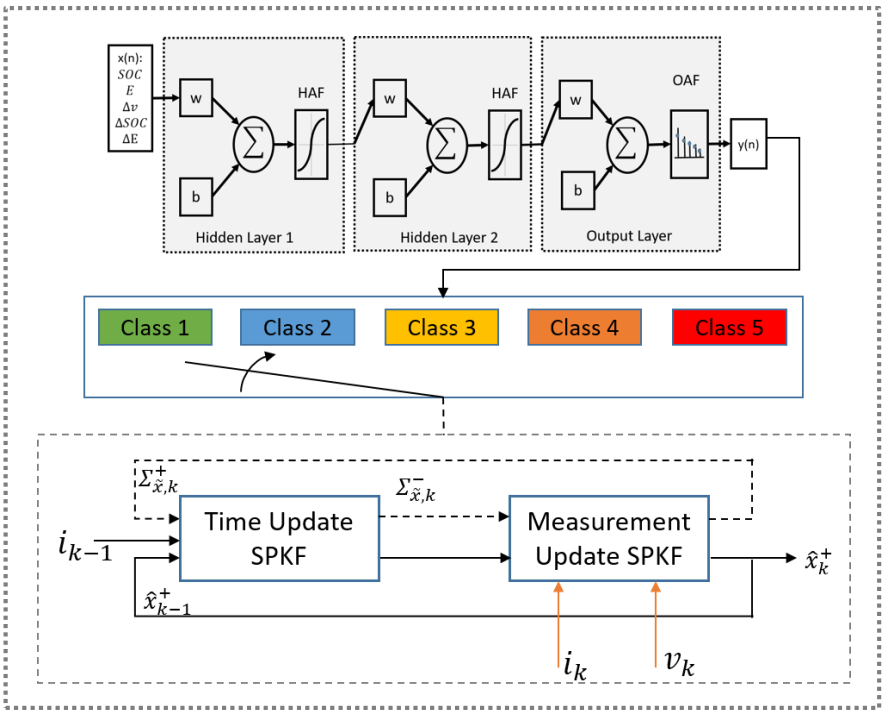

Figure 5.1: Applying SOH estimation to enhance SOC estimation with SPKF as battery ages.

5.2. Results

In this section, the result of SOC estimation with SPKF will be analysed. First, the SOC estimation is analysed without the influence of the SOH, and secondly, it is analysed considering the influence of SOH.

5.2.1 The SOC estimation with no SOH Correction

In this case, the parameters of a single class in Table 5.1 are used on the cell model for the estimation of SOC. This demonstrates the performance degradation of SPKF as the cell parameters change while the cell ages. Figure 5.2 shows the SOC estimation that is computed with the parameters of the battery from Class 1. Figure 5.2b shows the RMSE at every time step in a discharge phase.

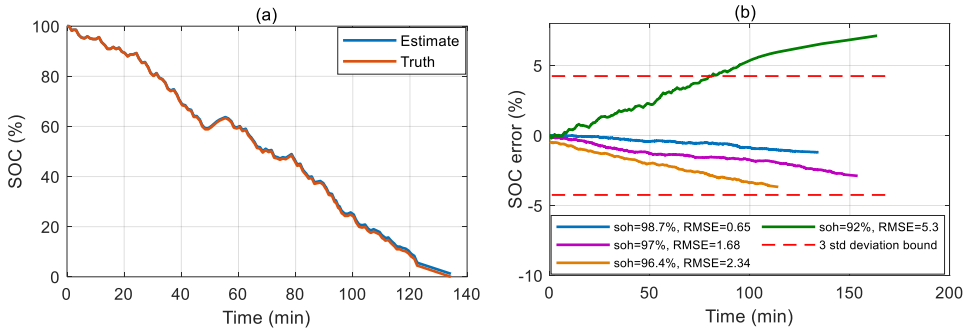

Figure 5.2: The SOC estimation using SPKF for the cell model designed with the parameters of Class 1. a: the estimated and true SOC in discharge phase when SOH is 98.7%. b: the RMSE of estimation for different SOH.

Figure 5.2a shows the estimated and true values of SOC in the discharge phase when the SOH of the cell is equal to 98.7%. Similar plots are obtainable for the rest of SOH but are not shown to avoid over-clustering. The RMSE of 0.65% at this value of SOH of the cell is the least. It can be seen from Figure 5.2b that as the cell ages, the RMSE increases. The RMSE increases to 1.69% at 97% SOH, and to 2.34% at 96.4% SOH. Until this point, the RMSE is within the acceptable range of ± 4% designed for a 99.7% confidence interval. As the battery ages beyond the SOH of class 1 (i.e. below 95%), the RMSE becomes more pronounced. This is because, as the cell ages, the parameters change significantly. If the parameters are not updated, there is a high tendency for model drift. In this case, the RMSE of the cycle is found to deviate beyond the confidence bound when the SOH decreases to 92%.

5.2.2 The SOC estimation considering the influence of SOH

To enhance SOC estimation by putting cell ageing into consideration, the parameters of the cell model that is used for the estimation of SOC is updated based on the cell SOH. The performance of SPKF is analysed across the entire cycle life of the cell. Figure 5.3 shows the SOC estimation when the cell SOH is 83.5% and the RMSE error over the cell cycle life.

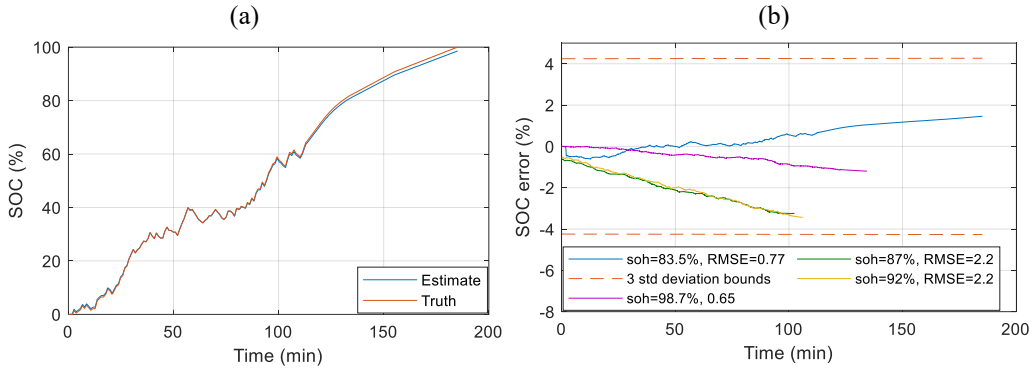

Figure 5.3: The SOC estimation using SPKF for the battery model parameters updated with the SOH. a: the estimated and true SOC in the charging phase when the SOH is 83.5%; b: the RMSE of estimation over the cell cycle life.

Figure 5.3a: shows the estimated and true values of SOC in the charge phase when the SOH of the cell is equal to 83.5%. The RMSE of the estimation over the cell cycle life is shown in Figure 5.3b: By updating the parameters of the cells, the RMSE of the estimation is maintained within the acceptable error bound over the cell cycle life.

Chapter 6. Adaptive MPC including Battery Thermal Limitations for Fuel Consumption Reduction in P2 HEV

This chapter is dedicated to demonstrating a strategy for energy optimization in HEV. Figure 6.1 shows the scheme of a parallel P2 configuration of HEV that is adopted for this analysis. A P2 configuration can be On-axis or Off-axis depending on the position of the EM. In the Off-axis P2 HEVs as in the figure, the ICE shaft can be linked to the EM shaft through the axis gear, chain or belt. A generic case with a P2 off-axis configuration has been analysed putting into consideration the additional variables, such as the transmission ratio and efficiency of belt drive. However, an off-axis can be converted to an on-axis configuration by setting the aforementioned parameters to unity. When C0 is open, the vehicle runs on pure electric mode with an efficient regeneration of the braking energy. The presence of a clutch C1 creates the possibility to use the EM as a starter to crank the ICE and for gear shifting.

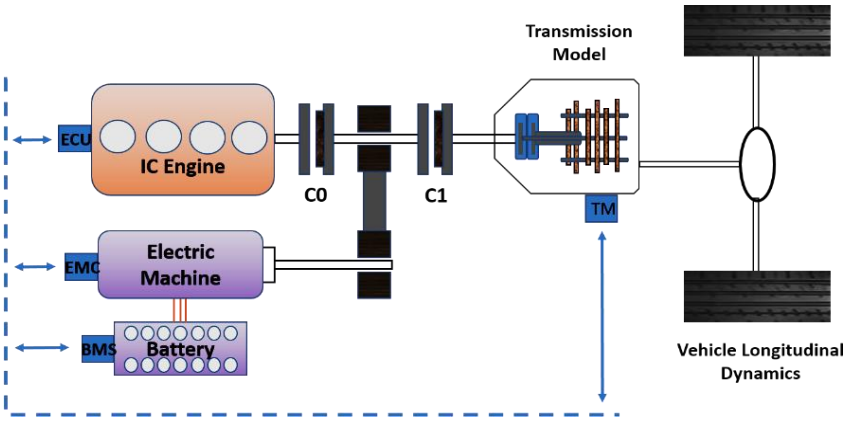

Figure 6.1: P2 Off-axis Configuration HEV powertrain integrated with an energy management system (EMS).

For energy optimization and control based on a backward model, the powertrain torque request at the transmission model (TM) is satisfied with the combination of torques provided by the ICE and EM. The battery pack serves as an energy reservoir to store and release energy to the EM. The EMS interfaces with the ICE, the EM and the battery pack through the engine control unit (ECU), the

electric machine control (EMC) and the battery management system (BMS), respectively.

The present section aims to investigate the influence of the battery pack capacity on the thermal behaviour and the fuel consumption of the HEV using an adaptive MPC strategy. The analysis is conducted, observing the influence of predictability with a practically implementable prediction horizon. Hence, the minimum battery capacity, which allows its operation without thermal implications is defined. The information from the prediction horizon helps to minimise overdesign by lowering the minimum battery capacity that the battery can be operated without thermal runaway. Moreover, there is an overall improvement in fuel consumption and battery thermal behaviour.

6.1. Methodology

6.1.1 The Hybrid Electric Vehicle (HEV)

Energy consumption optimisation through power splitting is the major goal of HEVs. The strategy for this optimisation is developed considering the necessary constraints to stay consistent with the physical limitations coming from the vehicle systems. This paper focuses on the P2 HEV powertrain that is shown in Figure 6.1. The vehicle is modelled using a backward approach that computes the wheel torque and speed to follow a given drive cycle. The wheel torque and speed are then propagated to the power sources through the powertrain [85].

The power request that corresponds to a given drive condition is acquired for a given gear combination from the transmission control. Applying MPC strategy, the torque values of EM, T_{em} and ICE, T_{ice} are decided for the optimum energy consumption, considering the operating constraints of the ICE and the EM. The subsystems of the backward model are addressed in the following sections, and the parameters of the vehicle model are defined in Table 6.1.

Table 6.1: The vehicle specifications for Mazda CX9 2016 [86]

	Parameter	Unit	Variable	Value
Vehicle Description	Nominal mass	kg	M	2041
	Frontal Area	m^2	A_f	2.4207
	Aerodynamic drag coefficient	-	c_x	0.316
	Gear ratios	-	i_g	6-speed gear shift
	Final Drive Ratio	-	i_{final}	4.41
	Tire size	-		P255/50VR20
	Passenger Capacity			7
Internal Combustion Engine	SAE Net Torque @ rpm	Nm		310 @ 2000
	Fuel System	-		Gasoline Direct Injection
	SAE net power @ rpm	kW		169 @ 5000
	Displacement	L		2.5

Electric Motor	Maximum power	kW		27
	Maximum torque @ rpm	Nm	$T_{em.max}$	65 @ 4000
Battery (Sanyo NCR 18650 GA Lithium-ion cell)	Single-cell nominal voltage	V	v_{nom}	3.6
	Single-cell nominal capacity	Ah	C_{nom}	3.2
	Minimum battery SOC	%	SOC_{min}	0
	Maximum battery SOC	%	SOC_{max}	100
	Operating temperature	°C	θ_{surf}	−20~60
	Ambient temperature	°C	θ_{amb}	20
	Battery Pack Configurations	-		14s6p and 14s10p

The detailed description of the backward model and its experimental validation for the case with a conventional powertrain (Mazda CX9 2016) is illustrated in [4]. Furthermore, the experimental design and validation of the battery electro-thermal model described here are illustrated in Chapter 4. Both the model and the control strategy are designed and simulated in MATLAB and Simulink platform with a sampling time, T_s of 0.5 seconds. Figure 6.2 shows the backward model simulation scheme that is discussed in detail in the subsequent sections.

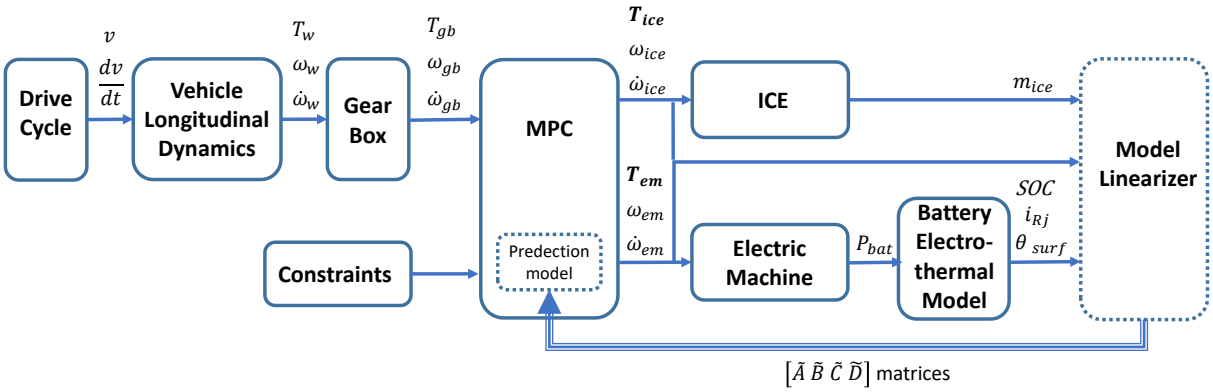

Figure 6.2: The backward model simulation scheme for HEV with integrated MPC.

6.1.2 Vehicle Longitudinal Dynamic Model

The power request on the axle P_w is computed considering the drag losses on the axle bearings T_{loss} and the contribution of the wheels' inertia J_w according to Equation 6.1. The required longitudinal traction force F_w is transmitted to the wheels to overcome the aerodynamic resistance, the rolling resistance and the vehicle inertia as expressed in Equation 6.2. Since homologation cycles assume flat road and simulations in this work are performed based on these homologation cycles, the resistive force due to road inclination is neglected.

$$P_w = T_w \cdot \omega_w = \left(F_w \cdot R_w + 4 \cdot J_w \cdot \frac{dv}{dt} \cdot \frac{1}{R_w} + T_{loss}\right) \cdot \omega_w \quad (6.1)$$

$$F_w = \frac{1}{2} \cdot \rho_{air} \cdot C_x \cdot A_f \cdot v^2 + M \cdot g \cdot f_r + M \cdot \frac{dv}{dt} \quad (6.2)$$

where M is the vehicle mass; v and dv/dt are the longitudinal speed and acceleration; f_r is the coefficient of rolling resistance; C_x is the aerodynamic drag coefficient; ρ_{air} is the air density; A_f is the vehicle's frontal area; R_w is the wheel rolling radius; T_w is the torque request on the axle; and ω_w is the angular speed of the wheel shaft.

6.1.3 Vehicle Transmission Model (Gearbox)

The transmission model converts T_w and ω_w to the corresponding gearbox torque T_g and gearbox angular speed ω_g based on the selected gear ratio i_g and the final gear ratio i_f. T_g is computed according to Equation 6.3. A speed-based gearshift strategy of the 6-speed gearbox is implemented in the model accounting for the constraint of ICE maximum speed. The gearshift applied in this work is given in [4] by analysing the gearshift experimental data from Argonne National Laboratory (ANL) [86,87].

$$\begin{cases} T_g = \dfrac{T_w}{i_f \cdot \eta_f \cdot i_g \cdot \eta_g} & if \quad T_w > 0 \\ T_g = \dfrac{T_w \cdot \eta_f \cdot \eta_g}{i_f \cdot i_g} & if \quad T_w \leq 0 \end{cases} \quad (6.3)$$

where the efficiencies of the final gear and the gearbox are considered as $\eta_f = \eta_g = 0.98$. The ω_g is computed accordingly from Equation 6.4.

$$\omega_g = \omega_w \cdot i_f \cdot i_g \quad (6.4)$$

6.1.4 The Internal Combustion Engine

Conventional vehicles rely solely on the ICE as the traction source. It is a common practice to model the fuel consumption of the ICE with static maps. The fuel consumption map for Mazda CX9 2016 ICE is used for analysis in this work [87]. The map is shown in Figure 6.3 where the fuel consumption rate $\dot{m}_{ice}$ is defined as a two-dimensional function of engine torque T_{ice} and speed ω_{ice}. The maximum operating torque $T_{ice,max}$ of the ICE is limited by the engine wide open throttle (WOT) characteristics. The steady-state map was obtained without loads of

alternator and water pump. The oil pump load was included in the experimental tests [87].

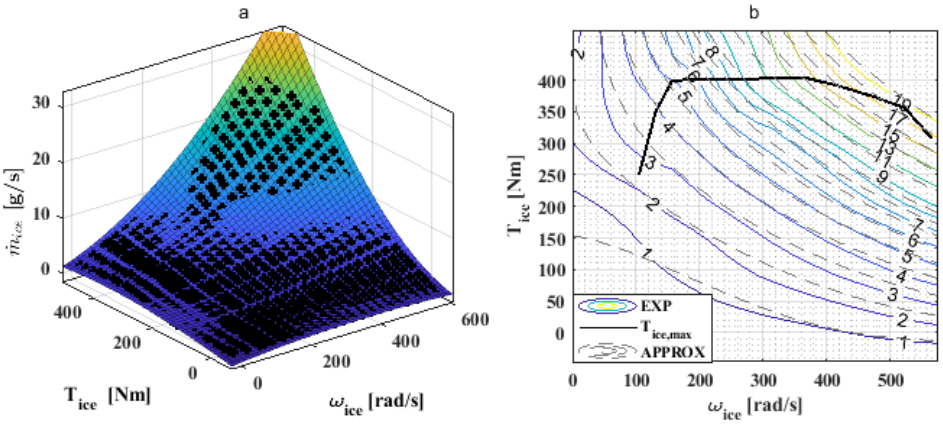

Figure 6.3: a: Fuel consumption map of Mazda CX9 2016 ICE as a function of engine torque and speed. The dots are the estimated values. b: The maximum operating engine torque as a function of engine speed.

The analytical model of the fuel consumption rate $\dot{m}_{ice}$ was derived using polynomial curve fitting as described in Equation 6.5. The regression coefficients of the polynomial function were estimated with a fit goodness indicator R-square = 0.91. Figure 6.3b shows the maximum engine torque and visualizes the goodness of fit of the two fuel consumption rates: experimentally obtained (solid lines–EXP) and approximated from Equation 6.5 (dashed lines–APPROX).

$$\dot{m}_{ice}(T_{ice},\omega_{ice}) = p_{00} + p_{10}\cdot T_{ice} + p_{01}\cdot \omega_{ice} + p_{20}\cdot T_{ice}^2 + p_{11}\cdot \omega_{ice}\cdot T_{ice} + p_{02}\cdot \omega_{ice}^2 + p_{30}\cdot T_{ice}^3 + p_{21}\cdot T_{ice}^2\cdot \omega_{ice} + p_{12}\cdot T_{ice}\cdot \omega_{ice}^2 + p_{03}\cdot \omega_{ice}^3 \quad (6.5)$$

6.1.5 Electric Machine (EM)

The presence of the EM provides an alternative or supporting power source for the powertrain of the HEV. The electric machine can either act as an electric motor or as a generator. When the vehicle is accelerated, the EM acts as an electric motor, drawing energy from the battery to lower or eliminate the ICE fuel consumption. If the vehicle is decelerated, the EM acts as a brake, and the generated energy is stored in the battery. Equation 6.6 computes the power requested from the battery in charge and discharge modes. Similar to the ICE, the maximum operating torque of the EM is limited by maximum motor torque $T_{mo,max}$ and maximum generator torque $T_{gen,max}$ defined as functions of ω_{em} as shown on the efficiency map in Figure 6.4.

$$P_{bat} = \begin{cases} T_{em} \cdot \omega_{em} \cdot \eta_{gen}, \ charge \\ T_{em} \cdot \omega_{em} / \eta_{mot}, \ discharge \end{cases} \tag{6.6}$$

η_{gen} and η_{mot} are the respective generator and motor efficiencies.

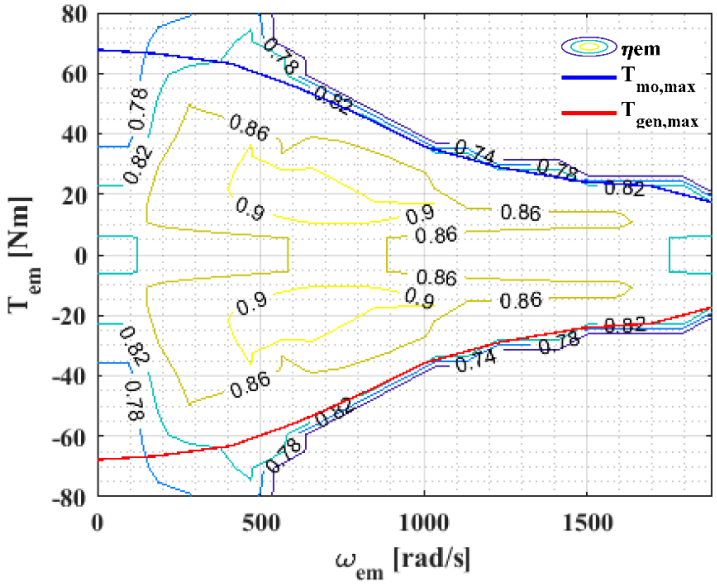

Figure 6.4: Efficiency map of the electric machine in both motor and generator operating modes. The maximum motor torque and maximum generator torque, defined as functions of electric machine speed.

6.1.6 Battery and Electro-Thermal Model

The battery pack serves as the energy reservoir for the storage of electrical energy. The electro-thermal model is incorporated in the vehicle model to provide the state information to the controller for optimization of fuel consumption and to prevent thermal runaway. At each time instant k, the adopted controller requires the battery state information. This information is the output of the battery pack electro-thermal model that takes the power request P_{bat} as input.

Two battery packs of 0.9 and 1.5 kWh capacities are designed using 14s6p and 14s10p configurations, respectively. These capacities correspond to the range of commercially available HEV batteries [2]. The configuration indicates the series and parallel combination of cells. 14s6p means 14 modules of six parallel cells connected in series. The battery packs are built from the electro-thermal model developed in Section 4.1 with Sanyo NCR 18650 GA lithium-ion cells that have a capacity of 3.3 Ah and a nominal voltage of 3.6 V [80]. The difference in the capacities of these two batteries is useful to analyse the influence of battery sizing on thermal behaviour and fuel consumption. Refer to Table 6.1 for the cell specification.

6.2. Energy Management System (EMS) Strategy with Adaptive MPC

The EMS in HEVs is responsible for minimising energy consumption without violating the operating limitations of the vehicle system. Using an MPC, this task is defined as the objective or cost function that is minimised across a defined prediction horizon while respecting the defined constraints. A prediction horizon $p = 20$ is applied in the final design. This corresponds to a prediction distance of 80–90 m at an average driving speed of 31.5 km/h for the UDDS cycle considering a sampling time of 0.5 seconds.

6.2.1 Design of an MPC Internal Prediction Model

The MPC is equipped with a linearized internal plant model for making predictions across a defined horizon. The MPC internal prediction model and the constraints are derived as the linear approximation of the model of the internal combustion engine and the battery electro-thermal model. The model has three (3) inputs, four (4) states and three (3) outputs as highlighted in Table 6.2. The inputs include the torque of EM, torque of ICE and speed of ICE. The torque of EM and torque of ICE are the manipulated variables while the speed of ICE is assumed to be a measured disturbance to the model. The speed of the EM is derived by scaling the speed of the ICE with the off-axis gear ratio of 2.7. The states include: the SOC, diffusion-resistor current i_{Rj}, battery surface temperature θ_{surf} and fuel consumed m_{ice}, which is an integration of $\dot{m}_{ice}$. The outputs of the model are the SOC, θ_{surf} and m_{ice}.

For the MPC prediction model design, $P_{loss,k}$ is computed neglecting the hysteresis components and the model is evaluated at a single operating point. This simplifies the model without significant deviation from the true model. Furthermore, the presence of feedback in the control strategy compensates for such deviation.

Table 6.2: Inputs, states, eigenvalues and output variables of the linearized nominal internal plant model.

Input	States Variable	Nominal Eigenvalue	Output
Torque of EM ($\boldsymbol{T_{em}}$)	State of charge (SOC)	0	SOC
Torque of ICE ($\boldsymbol{T_{ice}}$)	Diffusion-resistant current (i_{Rj})	−0.002s	θ_{surf}
	Battery temperature (θ_{surf})	−0.0282	
Speed of ICE ($\boldsymbol{\omega_{ice}}$)	Fuel consumed (m_{ice})	0	m_{ice}

From Table 6.2, the presence of zero eigenvalues resulting from the presence of the integrators in SOC and m_{ICE} contributes to the marginal stability of the nominal plant model. The small magnitude of the non-zero eigenvalues is an indication of the slow dynamics of the model.

6.2.2 Design of Standard MPC

The adaptive MPC is built on the standard MPC [88,89]. In general form, the MPC optimisation problem is formulated in discrete time as an argument that minimises the cost function $J(u_k)$ subject to the states of the model and the constraints as in Equation 6.7. $J(u_k)$ is a contribution of the cost due to output reference error (e) minimisation, J_y; the cost due to input variation minimisation, $J_{\Delta u}$; and the cost due to constraint violation (ε) minimisation J_ε; $\varepsilon = 0$ implies a hard constraint. The constraint is softened with an increase in non-negative ε.

$$\arg\min_{u_k} \Big(J(u_k) = J_y(u_k) + J_{\Delta u}(u_k) + J_\varepsilon(u_k) \Big); \quad u_k = [T_{em}, T_{ice}]$$

subject to

$$\begin{aligned} SOC &= f_1(T_{em}, \omega_{em}) \\ i_{Rj} &= f_2(T_{em}, \omega_{em}) \\ \theta_{surf} &= f_3(T_{em}, \omega_{em}) \\ m_{ice} &= f_4(T_{ice}, \omega_{ice}) \end{aligned}$$

and the constraints

$$\begin{aligned} T_{em,min} \le\ & T_{em} \le T_{em,max} \\ T_{ice,min} \le\ & T_{ice} \le T_{ice,max} \\ SOC_{min} \le\ & SOC \le SOC_{max} \\ \theta_{surf,min} \le\ & \theta_{surf} \le \theta_{surf,max} \\ & T_{req} = T_{em} + T_{ice} + T_{brake} \end{aligned} \tag{6.7}$$

where $J_y(u_k) = \sum_{i=1}^{p} w_e\, e_{k+i}^2$; $J_u(u_k) = \sum_{i=1}^{p-1} w_{\Delta u}\, \Delta u_{k+i}^2$; and $J_\varepsilon(u_k) = w_\varepsilon \varepsilon_k^2$, w_e, $w_{\Delta u}$ and w_ε are the penalising weights on the respective costs. Increasing the weight increases the importance of the corresponding component whose cost is desired to be minimised. w_e is set to 0.0001 for all the outputs since our goal is not to track the reference. $w_{\Delta u}$ is set to 0.01 for all the inputs to give some importance to minimising the input variation. w_ε is set to 100,000 to minimise violation of constraints. $T_{req} = T_g$ is the torque request computed from the transmission control. The subscripts min and max indicate the minimum and maximum values

of the variables. Table 6.3 lists the minimum and maximum limits of the input and output constraints.

Table 6.3: The minimum and maximum limits of the input and output constraints.

	T_{mo} (Nm)	T_{gen} (Nm)	T_{ICE} (Nm)	SOC	θ_{surf} (°C)
min	0	$-T_{EM,max}$	0	0.1	0
max	$T_{EM,max}$	0	$T_{ICE,max}$	0.9	50

The MPC problem is solved for the prediction horizon to compute the control sequence such that Equation 6.8 holds. The first element of the optimum control sequence is applied, and the control procedure is repeated.

$$T_{req} = T_{EM} + T_{ICE} + T_{brake} \tag{6.8}$$

The mechanical brake T_{brake} is applied to augment the T_{req} in the charge phase when T_{EM} cannot provide the required torque. It is desired to minimise T_{brake} as much as possible to use the maximum power of the electric machine.

6.2.3 Adaptive MPC

Adaptive MPC provides an intuitive approach for handling nonlinear control problems with linear controllers. A linearizer is developed to linearize the plant model at every time step. Since the HEV model is highly nonlinear both on the states and on the constraints, the standard MPC is suitable for controlling the model only at a single operating point. The main nonlinearity of the plant model comes from P_{loss}, θ_{surf} as well as the $\dot{m}_{ice}$. Furthermore, $T_{EM,max}$ and the $T_{ICE,max}$ introduce nonlinear constraint functions. These constraints are shown in Figure 6.4 and Figure 6.3b, respectively. They are in polynomial form in Equations 6.9 and 6.10 as suitable for applying in an MPC.

$$T_{EM,max} = 1.6838\times10^{-8}\omega_{em}^3 - 4.4193\times10^{-5}\omega_{em}^2 - 0.0023\omega_{em} + 68.4266 \tag{6.9}$$

$$T_{ICE,max} = \begin{cases} 2.569\omega_{\text{ice}} + 2.699 \; if \; \omega_{ice} < 154 \; rad/s \\ -3.687 \times 10^{-6}\omega_{ice}^3 + 0.002866\omega_{ice}^2 - 0.6857\omega_{ice} + \ldots \\ 450.3 \; elseif \; \omega_{ice} > 154 \; rad/s \end{cases} \tag{6.10}$$

The Adaptive MPC controls the nonlinear HEV model with a standard linear MPC whose prediction model is updated at every time step k. To update the linear MPC, the HEV model is linearized at every time step and the linear parameters are used to update the parameters of the MPC prediction model. The linearized model is obtained by computing the Jacobian matrix at each time step. The stability and

disturbance rejection properties for this approach are addressed in the literature in [90,91]. The linearized model is computed according to Equation 6.11.

$$\begin{aligned} x_{k+1} &= \tilde{A}x_k + \tilde{B}u_{i,k} + \tilde{K}u_{d,k} \\ y_{k+1} &= \tilde{C}x_k + \tilde{D}u_{i,k} + \tilde{E}u_{d,k} \end{aligned} \tag{6.11}$$

where $\tilde{A} = \left(\frac{df}{dx}\right)_{(x_k,u_{i,k},u_{d,k})}$, $\tilde{B} = \left(\frac{df}{du_i}\right)_{(x_k,u_{i,k},u_{d,k})}$, $\widetilde{K} = \left(\frac{df}{du_d}\right)_{(x_k,u_{i,k},u_{d,k})}$,

$\tilde{C} = \left(\frac{dy}{dx}\right)_{(x_k,u_{i,k},u_{d,k})}$, $\widetilde{D} = \left(\frac{dy}{du_i}\right)_{(x_k,u_{i,k},u_{d,k})}$, $\tilde{E} = \left(\frac{dy}{du_d}\right)_{(x_k,u_{i,k},u_{d,k})}$;

x_k, $u_{i,k}$ and $u_{d,k}$ are the current values of the states, the manipulated inputs and the disturbances of the system, respectively.

For the HEV fuel consumption minimisation problem, at each time step, assuming that the velocity of the vehicle is known for a defined prediction horizon, the states of the model can be predicted within this horizon, and the MPC problem is solved to compute the control sequence. The prediction information helps the return optimum results within the prediction horizon. The energy consumption is minimised, and the thermal behaviour is enhanced as reported in Section 6.3. The presence of prediction information helps to avoid overdesign by reducing the minimum battery capacity that is needed to avoid thermal runaway. This can be verified by comparing the adaptive MPC results with that of ECMS [4].

6.3. Results and Discussion

The HEV model performance is first analysed under an optimized On/Off condition (without MPC) to define a reference for comparing the optimized results when a temperature limit is imposed. The analysis is conducted with the 0.9 kWh battery of configuration 14s6p. Second, the model performance is analysed with the adaptive MPC, first, with no limit on temperature. The prediction horizon is set to $p = 2$. The energy consumption and CO_2 emission are computed under these conditions. To understand the influence of the prediction horizon, the MPC is set to $p = 20$, and the model performance is analysed with no temperature limits. Furthermore, a thermal constraint is imposed, and the influence of temperature on energy consumption is evaluated. Finally, battery sizing is demonstrated as a means to efficiently enhance the thermal behaviour of the battery pack while improving energy savings. The battery capacity is gradually increased to determine the minimum battery capacity suitable to avoid thermal runaway. A minimum capacity of 1.5 kWh with the configuration 14s10p is determined for the performance analysis. The results of the analyses are summarized in Table 6.4.

6.3.1 Fuel Consumption Computation Based on On/Off Model

The first attempt in imposing battery temperature limitations in fuel consumption optimization is to define a reference based on an optimized model upon which the optimized results can be compared. The HEV model is run in this mode without the MPC. To obtain the temperature limitation in the On/Off mode, the electric machine is allowed to work only when the battery surface temperature is less than the maximum operating temperature of the battery. When the battery temperature approaches the maximum, the system runs on pure ICE mode. In other words, the electric-assist mode is activated only when the battery temperature is below the maximum operating temperature. Considering the temperature operating range of the battery, a maximum battery surface temperature of 55 °C is defined in this work. This scenario is considered the worst-case fuel consumption case since the EM is utilized with no optimization. The analysis is carried out considering the 14s6p battery configuration and an ambient temperature of 20 °C. The main results are shown in Figure 6.5.

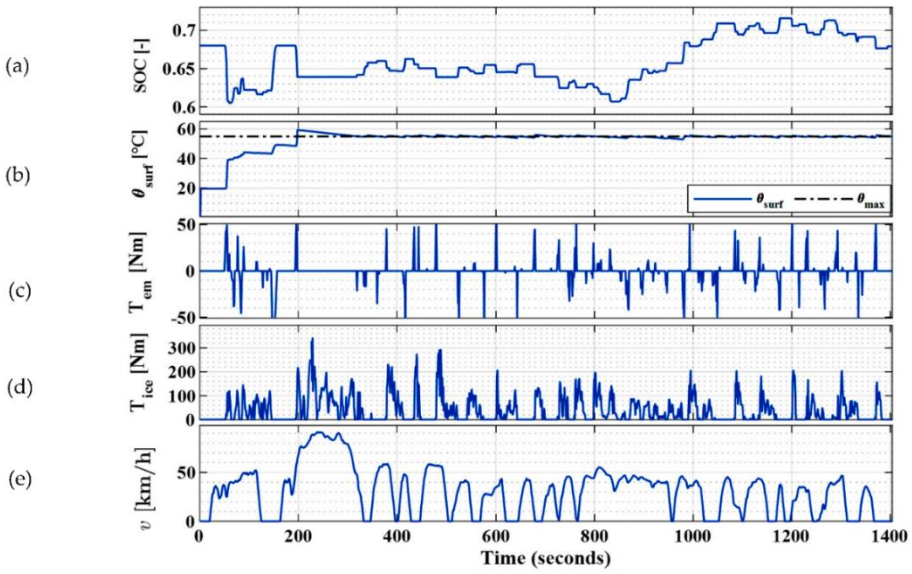

Figure 6.5: On/off model evaluated with 14s6p battery configuration. a: the state of charge; b: the battery surface temperature; c: the EM torque; d: the ICE torque; and e: the velocity of the UDDS drive cycle.

The acceleration phase of the drive cycle velocity profile in Figure 6.5e corresponds to a positive torque request, while the deceleration corresponds to a negative torque request. Although the maximum battery temperature is defined as 55 °C, there is a slight overshoot at 200 s. The reason for this overshoot is that, in one simulation step, the temperature raised fast and the action to turn off the use of electric traction was performed with a delay at the next simulation step.

This can be avoided by using smaller simulation step size. However, this does not impact the results of the analysis significantly. To realize a charge sustaining

mode, the SOC starts and ends at approximately equal values. In this on/off mode, the computed fuel consumption is equal to 672 g corresponding to CO_2 emission values of 175.7 g/km [92] as reported in Table 6.4. The CO_2 emission is computed from gasoline by multiplying fuel consumption in litre with a gain of 2330 [g/L] value according to the EU technical guidelines (Regulation (EU) No 510/2011).

6.3.2 Adaptive MPC Strategy Results

6.3.2.1. No Thermal Limitation Constraint:

The MPC is analysed here applying no limits on the battery surface temperature to optimize fuel consumption and the corresponding CO_2 emission for the 14s6p battery pack configuration. The results of this analysis will be used as a benchmark to evaluate the model performance when thermal constraints are imposed. The adaptive MPC in this section is set to $p = 2$.

This is a good approximation of an ECMS implementation where the computation is instantaneous or non-predictive. Under this condition, the simulation of the plant dynamics (especially the electro-thermal model) is within a very limited horizon. This results in a low adaptation of the controller. The minimum value of $p = 2$ (against $p = 1$ as in the case of ECMS) is due to the structural limitation of MPC. This is because the input constraint u_{min} operates in the range of $k\ to\ k + p - 1$. The results are shown in Figure 6.6.

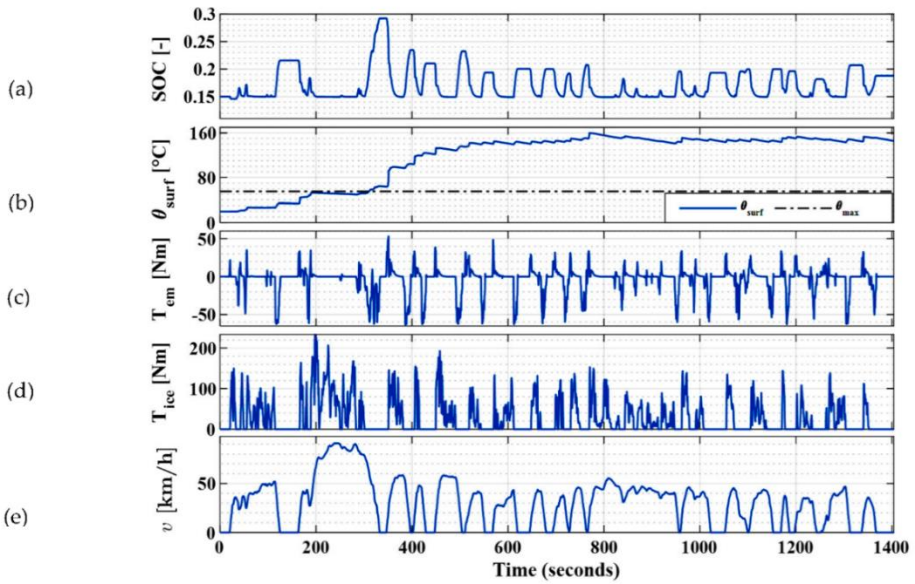

Figure 6.6: MPC evaluated with $p = 2$ using 14s6p battery configuration, no thermal limitations. a: is the state of charge; b: is the battery surface temperature; c: is the EM torque; d: is the ICE torque; e: is the velocity of the UDDS drive cycle.

With no constraint applied to limit the temperature of the battery, the fuel consumed is 618.5 g while the CO_2 emissions are 161.8 g/km. This corresponds to

an energy saving of 11.6% relative to the conventional vehicle and 8% relative to the On/off model. However, it can be seen from Figure 6.6b that the surface temperature of the battery can reach as high as 160 °C. This is way beyond the maximum operating temperature $\theta_{max} = 55$ °C of the battery that is shown with a dotted line.

6.3.2.2. Increased Prediction Horizon with No Thermal Limitation Constraint:

Increasing the prediction horizon of the adaptive MPC enhances its thermal handling capability. In this case, the model is simulated with an increased prediction horizon. By increasing the prediction horizon, MPC can predict a possible disturbance in advance and act accordingly to minimise the effect. Thermal shock can also be minimised in the process. The analysis is repeated as in Section 6.3.2.1 but with the prediction horizon set to $p = 20$. Figure 6.7 shows the results of the analysis.

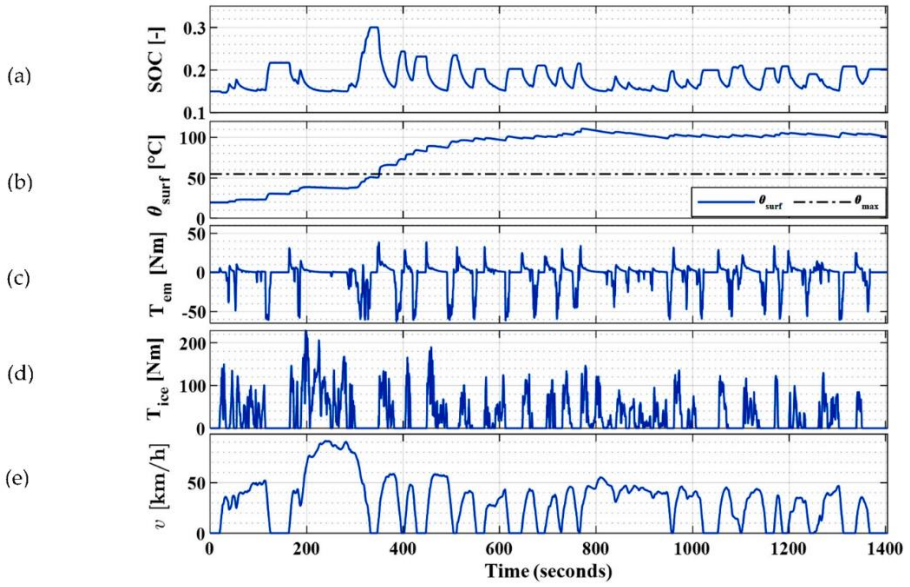

Figure 6.7: MPC evaluated with $p = 20$ using 14s6p battery configuration, no thermal limitations; a: is the state of charge; b: is the battery surface temperature; c: is the EM torque; d: is the ICE torque; e: is the velocity of the UDDS drive cycle.

By increasing the prediction horizon from 2 to 20, the battery surface temperature is reduced from 160 to 111 °C and thermal shock is minimised as shown in Figure 6.7b. In this case, 610 g of fuel is consumed. This corresponds to 159.5 g/km CO_2 emission, hence, an improvement relative to a low prediction horizon of 2. This corresponds to an energy saving of 12.8% relative to the conventional vehicle and 9.2% relative to the On/Off mode.

6.3.2.3. Introducing Thermal Limitation Constraint:

The adaptive MPC is desired to maintain the temperature of the battery below the maximum temperature of 55 °C while minimising the energy consumption. It is possible to achieve this temperature limit using the 0.9 kWh (14s6p configuration) battery with a reduced maximum EM torque output, however. The classical approach for temperature limitation with MPC is to impose a boundary constraint on the maximum temperatures. However, due to the high nonlinearity that is associated with the temperature variable, the boundary constraint is violated occasionally in this case. An alternative approach is to impose a constraint on the range variation of the battery SOC. This limits the magnitude of energy that can be delivered by the battery.

The T_{req} is satisfied with the increase in the use of the T_{brake} in the vehicle deceleration mode to dissipate the surplus energy produced. In acceleration mode, however, there is an increase in the use of the T_{ice} and consequently, an increased fuel consumption. Figure 6.8 shows the results of this analysis for $p = 20$.

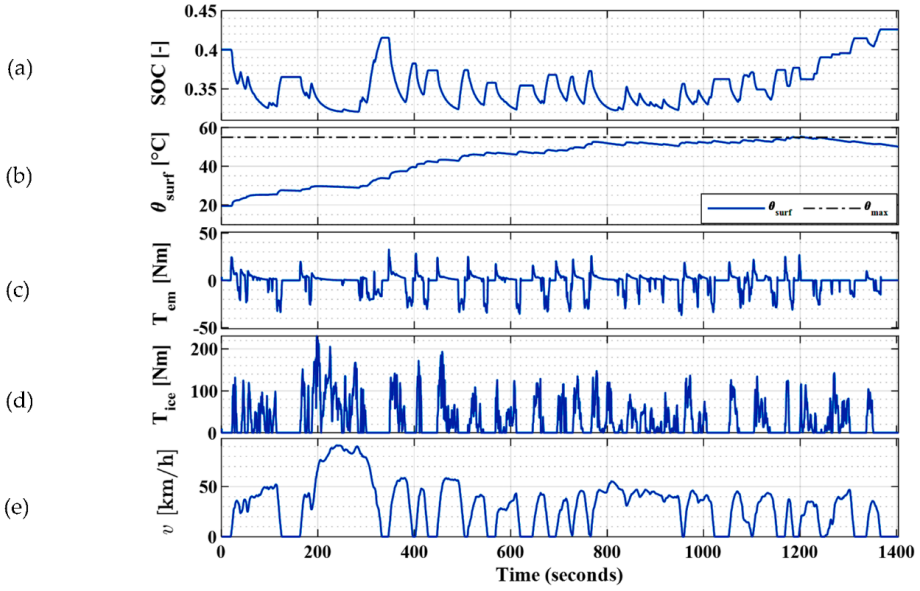

Figure 6.8: MPC evaluated with $p = 20$ using 14s6p battery configuration, applied thermal limitation; a: is the state of charge; b: is the battery surface temperature; c: is the EM torque; d: is the ICE torque; e: is the velocity of the UDDS drive cycle.

The thermal limitation is achieved by limiting the SOC of the battery to vary in the range of 0.3 to 4.5. The fuel consumed in the process is 621.5 g and the CO_2 emissions are 162.6 g/km. This corresponds to about 11.3% energy saving when compared to the conventional vehicle and about 7.6% when compared to the On/Off model. The results in Figure 6.8 show that the adaptive MPC can maintain the battery surface temperature below the defined maximum limit of 55 °C. However, this is possible with a compromise on the limit of the operating EM torque output and on the fuel consumption. Figure 6.9 compares the torques in this case with the

cases when there are no thermal limitations in the operating point efficiency map of EM and ICE.

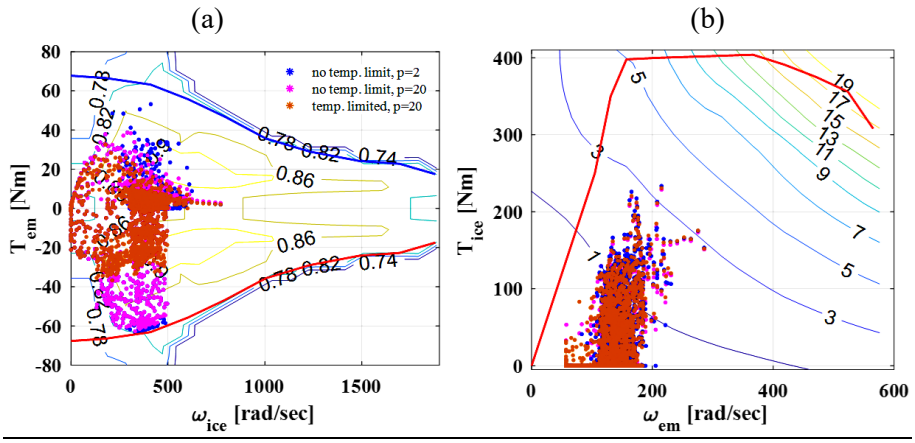

Figure 6.9: Operating torque comparison between the case with thermal limitation and without thermal limitations in the efficiency map. a: The electric machine torque comparison; and b: the ICE torque comparison.

It can be seen from Figure 6.9b that the operating torque of the electric machine is reduced in the case of a thermal limitation compared to the cases when there are no thermal limitations.

6.3.2.4. Battery Thermal Enhancement with Battery Sizing:

From Section 6.3.2.3, it is possible to maintain the temperature of the battery below 55 °C but at a cost of increased fuel consumption resulting from the underutilization of the EM power. Optimum use of EM in presence of the defined thermal constraint is possible by increasing the battery capacity. The battery capacity can be increased by increasing the number of cells connected in parallel. By doing this, the maximum current that passes through each of the parallel cells is reduced by an approximate product factor of $1/N_p$, where N_p is the number of cells in parallel. Increasing the capacity of the battery permits softening the constraint imposed on the variation of SOC and the battery can deliver more energy. Maintaining the prediction horizon of 20, the experiment is repeated varying N_p in the fuel consumption optimization process. Without overdesigning, a suitable battery pack configuration of 14s10p (1.5 kWh) was chosen to satisfy the desired requirements. Figure 6.10 shows the results.

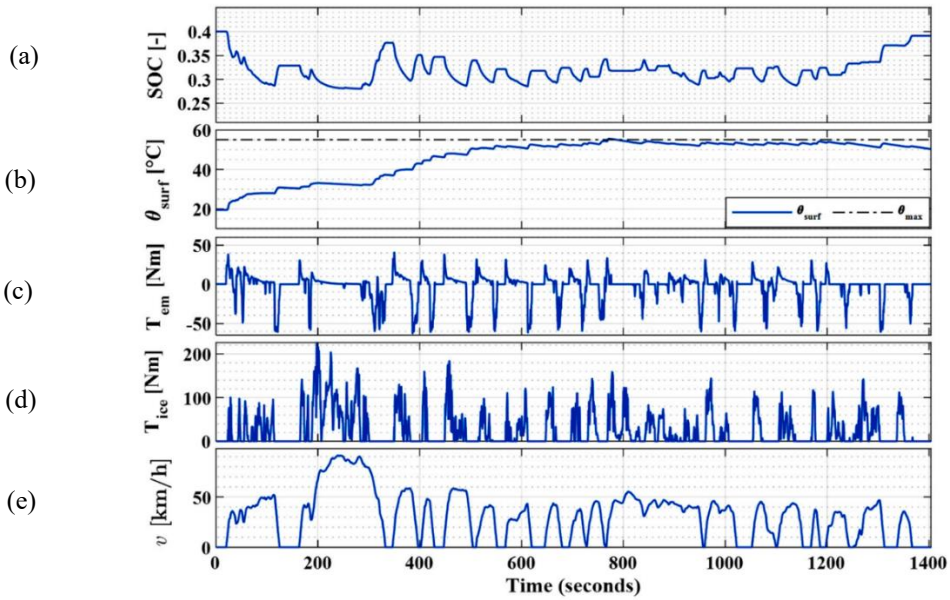

Figure 6.10: MPC evaluated with $p = 20$ using 14s10p battery configuration, a: is the state of charge; b: is the battery surface temperature; c: is the EM torque; d: is the ICE torque; e: is the velocity of the UDDS drive cycle.

By increasing the battery capacity from 0.9 to 1.5 kWh, the fuel consumed computed is 590.4 g while the CO_2 emissions are equal to 154.4 g/km. This corresponds to the energy saving of 15.7% relative to the conventional vehicle and 12.1% relative to the On/Off model. The battery operating temperature is maintained as desired with a maximum value of 55 °C while satisfying the torque request across the drive cycle.

The results of all the cases analysed here are summarised in Table 6.4.

Table 6.4: Result summary for different prediction horizons, battery pack configurations and operating conditions.

Operating Condition	Prediction Horizon	Pack Configuration	Maximum Temperature [°C]	Fuel Consumption [L/100 km]	Fuel Consumed [g]	Fuel Saving [%]	CO_2 Consumption [g/km]
Conventional vehicle	-	-	-	8.03	699.9	0	187.1
On/Off	-	14s6p	55	7.54	672	4	175.7
No. Temp Limit	2		160	6.94	618.5	11.6	161.8
No. Temp Limit	20		111	6.85	610	12.8	159.5
Temp. Limited	20		55	6.98	621.5	11.3	162.6
Increased battery capacity	20	14s10p	55	6.63	590.4	15.7	154.4

The percentage fuel savings computed in Table 6.4 is with respect to the conventional vehicle. The results shown in this work addressed the influence of MPC prediction capability and battery capacity on the thermal behaviour and fuel consumption of P2 HEV. By comparing the results of Sections 6.3.2.1 and 6.3.2.2, there is clear evidence that the future prediction capability of the MPC helps to improve the battery thermal behaviour. The battery temperature reduced from 160 to 111 °C when the prediction horizon was changed from 2 to 20. Section 3.2.3 demonstrates that the desired battery temperature range cannot be achieved using a 0.9 kWh battery while reducing fuel consumption. An optimum battery size with a capacity of 1.5 kWh was therefore chosen in Section 6.3.2.4 to achieve the desired temperature with an overall reduction in fuel consumption.

As a limitation of this model, the electro-thermal model used in this analysis was validated without considering battery ageing.

6.4. Summary and Conclusions

This work demonstrated the application of adaptive MPC for energy optimisation of P2 HEV considering battery pack thermal limitations. Two battery pack configurations, 14s6p and 14s10p with 0.9 and 1.5 kWh capacities, respectively, were considered. The developed electro-thermal model of the cell was used for predicting the electrical and thermal states of the battery pack.

The adaptive MPC strategy offer solutions to the nonlinear HEV energy management problem. The proposed solution is obtained respecting the system constraints over a defined prediction horizon of 20. This prediction horizon corresponds to about 80–90 m of prediction distance at an average driving speed of 31.5 km/h for the UDDS cycle. This prediction horizon can be realized by means of modern onboard ADAS systems.

The system was analysed with and without the thermal limitations of the battery pack using two different pack configurations and two prediction horizons (2 and 20). Based on this analysis, the reduction of CO_2 emission and fuel consumption was obtained by increasing the battery capacity and the prediction capability of the MPC model. High battery temperature and thermal shock were also minimised in the process. Minimum CO_2 emissions and fuel consumption were obtained using the prediction horizon of 20 and with the 14s10p battery configuration pack. The battery surface temperature was approximately 55 °C with the relatively lowest maximum temperature and with the least thermal shock.

It can be seen from the analysis that the prediction capability of the MPC can help to improve the thermal behaviour of the battery pack. However, to fully exploit the benefits of the MPC in minimising fuel consumption, an increase of the battery pack to 1.5 kWh is required. This minimum battery capacity is comparably smaller than that of non-predictive ECMS where the minimum capacity is 1.9 kWh [4].

In this work, a realistic prediction horizon realizable with onboard vehicle systems was considered. However, in future research, it would be interesting to see the potential of fuel consumption and thermal control improvement using MPC with

an optimal prediction horizon to obtain comparable results with dynamic programming-based optimization. The results shown in this paper were obtained without considering the influence of battery ageing. Therefore, such analysis could be of interest for future research.

References:

1. Iclodean, C.; Varga, B.; Burnete, N.; Cimerdean, D.; Jurchiș, B. Comparison of Different Battery Types for Electric Vehicles. *IOP Conf. Ser. Mater. Sci. Eng.* **2017**, *252*, 012058, doi:10.1088/1757-899X/252/1/012058.
2. Sanjarbek, R.; Mavlonov, J.; Mukhitdinov, A. Analysis of the Powertrain Component Size of Electrified Vehicles Commercially Available on the Market: *Commun. - Sci. Lett. Univ. Zilina* **2022**, *24*, B74–B86, doi:10.26552/com.C.2022.1.B74-B86.
3. Liu, R.; Zhang, C. An Active Balancing Method Based on SOC and Capacitance for Lithium-Ion Batteries in Electric Vehicles. *Front. Energy Res.* **2021**, *9*, 662, doi:10.3389/fenrg.2021.773838.
4. Yakhshilikova, G.; Ezemobi, E.; Ruzimov, S.; Tonoli, A. Battery Sizing for Mild P2 HEVs Considering the Battery Pack Thermal Limitations. *Appl. Sci.* **2022**, *12*, 226, doi:10.3390/app12010226.
5. Li, N.; Zhang, Y.; He, F.; Zhu, L.; Zhang, X.; Ma, Y.; Wang, S. Review of Lithium-Ion Battery State of Charge Estimation. *Glob. Energy Interconnect.* **2021**, *4*, 619–630, doi:10.1016/j.gloei.2022.01.003.
6. Liu, Y.; He, Y.; Bian, H.; Guo, W.; Zhang, X. A Review of Lithium-Ion Battery State of Charge Estimation Based on Deep Learning: Directions for Improvement and Future Trends. *J. Energy Storage* **2022**, *52*, 104664, doi:10.1016/j.est.2022.104664.
7. Jonny Dambrowski Review on Methods of State-of-Charge Estimation with Viewpoint to the Modern LiFePO4/Li4Ti5O12 Lithium-Ion Systems. In Proceedings of the INTELEC 2013; HAMBURG, GERMANY, October 13 2013.
8. Battery Management Systems, Volume 2: Equivalent-Circuit Methods Available online: http://mocha-java.uccs.edu/BMS2/ (accessed on 8 January 2022).
9. Peroutka, Z.; Smidl, V.; Vosmik, D. *Challenges and Limits of Extended Kalman Filter Based Sensorless Control of Permanent Magnet Synchronous Machine Drives*; 2009; p. 11;.
10. Agarwal, M.; Bonvin, D. Limitations of the Extended Kalman Filter for Batch Reactors. *IFAC Proc. Vol.* **1989**, *22*, 299–306, doi:10.1016/S1474-6670(17)53371-6.
11. Plett, G.L. Sigma-Point Kalman Filtering for Battery Management Systems of LiPB-Based HEV Battery Packs: Part 2: Simultaneous State and Parameter Estimation. *J. Power Sources* **2006**, *161*, 1369–1384, doi:10.1016/j.jpowsour.2006.06.004.

12. Sun, C.; Lin, H.; Cai, H.; Gao, M.; Zhu, C.; He, Z. Improved Parameter Identification and State-of-Charge Estimation for Lithium-Ion Battery with Fixed Memory Recursive Least Squares and Sigma-Point Kalman Filter. *Electrochimica Acta* **2021**, *387*, 138501, doi:10.1016/j.electacta.2021.138501.

13. Bonfitto, A. A Method for the Combined Estimation of Battery State of Charge and State of Health Based on Artificial Neural Networks. *Energies* **2020**, *13*, 2548, doi:10.3390/en13102548.

14. Tan, X.; Tan, Y.; Zhan, D.; Yu, Z.; Fan, Y.; Qiu, J.; Li, J. Real-Time State-of-Health Estimation of Lithium-Ion Batteries Based on the Equivalent Internal Resistance. *IEEE Access* **2020**, *8*, 56811–56822, doi:10.1109/ACCESS.2020.2979570.

15. Singh, P.; Kaneria, S.; Broadhead, J.; Wang, X.; Burdick, J. Fuzzy Logic Estimation of SOH of 125Ah VRLA Batteries. In Proceedings of the IN^{TEL}EC 2004. 26th Annual International Telecommunications Energy Conference; September 2004; pp. 524–531.

16. Bian, X.; Wei, Z.; Li, W.; Pou, J.; Sauer, D.U.; Liu, L. State-of-Health Estimation of Lithium-Ion Batteries by Fusing an Open Circuit Voltage Model and Incremental Capacity Analysis. *IEEE Trans. Power Electron.* **2022**, *37*, 2226–2236, doi:10.1109/TPEL.2021.3104723.

17. Diao, W.; Jiang, J.; Zhang, C.; Liang, H.; Pecht, M. Energy State of Health Estimation for Battery Packs Based on the Degradation and Inconsistency. *Energy Procedia* **2017**, *142*, 3578–3583, doi:10.1016/j.egypro.2017.12.248.

18. Ruan, H.; He, H.; Wei, Z.; Quan, Z.; Li, Y. State of Health Estimation of Lithium-Ion Battery Based on Constant-Voltage Charging Reconstruction. *IEEE J. Emerg. Sel. Top. Power Electron.* **2021**, 1–1, doi:10.1109/JESTPE.2021.3098836.

19. Jia, B.; Guan, Y.; Wu, L. A State of Health Estimation Framework for Lithium-Ion Batteries Using Transfer Components Analysis. *Energies* **2019**, *12*, 2524, doi:10.3390/en12132524.

20. He, J.; Wei, Z.; Bian, X.; Yan, F. State-of-Health Estimation of Lithium-Ion Batteries Using Incremental Capacity Analysis Based on Voltage–Capacity Model. *IEEE Trans. Transp. Electrification* **2020**, *6*, 417–426, doi:10.1109/TTE.2020.2994543.

21. Synchronous Estimation of State of Health and Remaining Useful Lifetime for Lithium-Ion Battery Using the Incremental Capacity and Artificial Neural Networks - ScienceDirect Available online: https://www.sciencedirect.com/science/article/pii/S2352152X19307340?via%3Dihub (accessed on 3 January 2022).

22. Bian, X.; Wei, Z.; He, J.; Yan, F.; Liu, L. A Novel Model-Based Voltage Construction Method for Robust State-of-Health Estimation of Lithium-Ion Batteries. *IEEE Trans. Ind. Electron.* **2021**, *68*, 12173–12184, doi:10.1109/TIE.2020.3044779.

23. Capacity-Fading Prediction of Lithium-Ion Batteries Based on Discharge Curves Analysis - ScienceDirect Available online: https://www.sciencedirect.com/science/article/pii/S0378775311015199?via%3Dihub (accessed on 3 January 2022).

24. Estimation of Battery State of Health Using Back Propagation Neural Network--《Computer Aided Drafting,Design and Manufacturing》2014. Available online: https://www.cnki.com.cn/Article/CJFDTotal-CADD201401011.htm (accessed on 3 January 2022).

25. Quantifying Cell-to-Cell Variations in Lithium Ion Batteries Available online: https://www.hindawi.com/journals/ijelc/2012/395838/ (accessed on 25 February 2022).

26. Pan, S.J.; Tsang, I.W.; Kwok, J.T.; Yang, Q. Domain Adaptation via Transfer Component Analysis. *IEEE Trans. Neural Netw.* **2011**, *22*, 199–210, doi:10.1109/TNN.2010.2091281.

27. Tang, X.; Zou, C.; Yao, K.; Chen, G.; Liu, B.; He, Z.; Gao, F. A Fast Estimation Algorithm for Lithium-Ion Battery State of Health. *J. Power Sources* **2018**, *396*, 453–458, doi:10.1016/j.jpowsour.2018.06.036.

28. Noura, N.; Boulon, L.; Jemeï, S. A Review of Battery State of Health Estimation Methods: Hybrid Electric Vehicle Challenges. *World Electr. Veh. J.* **2020**, *11*, 66, doi:10.3390/wevj11040066.

29. Wang, Z.; Feng, G.; Zhen, D.; Gu, F.; Ball, A. A Review on Online State of Charge and State of Health Estimation for Lithium-Ion Batteries in Electric Vehicles. *Energy Rep.* **2021**, *7*, 5141–5161, doi:10.1016/j.egyr.2021.08.113.

30. Sarmah, S.B.; Kalita, P.; Garg, A.; Niu, X.; Zhang, X.-W.; Peng, X.; Bhattacharjee, D. A Review of State of Health Estimation of Energy Storage Systems: Challenges and Possible Solutions for Futuristic Applications of Li-Ion Battery Packs in Electric Vehicles. *J. Electrochem. Energy Convers. Storage* **2019**, *16*, doi:10.1115/1.4042987.

31. Venugopal, P.; T., V. State-of-Health Estimation of Li-Ion Batteries in Electric Vehicle Using IndRNN under Variable Load Condition. *Energies* **2019**, *12*, 4338, doi:10.3390/en12224338.

32. Bonfitto, A.; Ezemobi, E.; Amati, N.; Feraco, S.; Tonoli, A.; Hegde, S. State of Health Estimation of Lithium Batteries for Automotive Applications with Artificial Neural Networks. In Proceedings of the 2019 AEIT International

Conference of Electrical and Electronic Technologies for Automotive (AEIT AUTOMOTIVE); July 2019; pp. 1–5.

33. Barcellona, S.; Piegari, L. Integrated Electro-Thermal Model for Pouch Lithium Ion Batteries. *Math. Comput. Simul.* **2021**, *183*, 5–19, doi:10.1016/j.matcom.2020.03.010.
34. Madani, S.S.; Schaltz, E.; Knudsen Kær, S. Review of Parameter Determination for Thermal Modeling of Lithium Ion Batteries. *Batteries* **2018**, *4*, 20, doi:10.3390/batteries4020020.
35. Forgez, C.; Vinh Do, D.; Friedrich, G.; Morcrette, M.; Delacourt, C. Thermal Modeling of a Cylindrical LiFePO4/Graphite Lithium-Ion Battery. *J. Power Sources* **2010**, *195*, 2961–2968, doi:10.1016/j.jpowsour.2009.10.105.
36. Wang, Q.; Jiang, B.; Li, B.; Yan, Y. A Critical Review of Thermal Management Models and Solutions of Lithium-Ion Batteries for the Development of Pure Electric Vehicles. *Renew. Sustain. Energy Rev.* **2016**, *64*, 106–128, doi:10.1016/j.rser.2016.05.033.
37. An, Z.; Jia, L.; Ding, Y.; Dang, C.; Li, X. A Review on Lithium-Ion Power Battery Thermal Management Technologies and Thermal Safety. *J. Therm. Sci.* **2017**, *26*, 391–412, doi:10.1007/s11630-017-0955-2.
38. *Modern Electric, Hybrid Electric, and Fuel Cell Vehicles: Fundamentals, Theory, and Design*; Ehsani, M., Gao, Y., Emadi, A., Eds.; 2nd ed.; CRC Press: Boca Raton, 2017; ISBN 978-1-315-21940-0.
39. *Advanced Electric Drive Vehicles*; Emadi, A., Ed.; CRC Press: Boca Raton, 2014; ISBN 978-1-315-21557-0.
40. Sieg, C.; Küçükay, F. Benchmarking of Dedicated Hybrid Transmissions. *Vehicles* **2020**, *2*, 100–125, doi:10.3390/vehicles2010006.
41. Sundström, O.; Guzzella, L.; Soltic, P. Optimal Hybridization in Two Parallel Hybrid Electric Vehicles Using Dynamic Programming. *IFAC Proc. Vol.* **2008**, *41*, 4642–4647, doi:10.3182/20080706-5-KR-1001.00781.
42. Neffati, A. *Fuzzy Switching of Fuzzy Rules for Energy Management in HEV*; 2012; p. 668; ISBN 978-3-902823-24-3.
43. Tie, S.F.; Tan, C.W. A Review of Energy Sources and Energy Management System in Electric Vehicles. *Renew. Sustain. Energy Rev.* **2013**, *20*, 82–102, doi:10.1016/j.rser.2012.11.077.
44. Ahmadi, S.; Hosseinpour, A.; Bathaee, S.M. Improving Fuel Economy and Performance of a Fuel-Cell Hybrid Electric Vehicle (Fuel-Cell, Battery, and Ultra-Capacitor) Using Optimized Energy Management Strategy. *Energy Convers. Manag.* **2018**, *160*, 74–84, doi:10.1016/j.enconman.2018.01.020.

45. Geng, B.; Mills, J.K.; Sun, D. Energy Management Control of Microturbine-Powered Plug-In Hybrid Electric Vehicles Using the Telemetry Equivalent Consumption Minimization Strategy. *IEEE Trans. Veh. Technol.* **2011**, *60*, 4238–4248, doi:10.1109/TVT.2011.2172646.

46. Rezaei, A.; Burl, J.B.; Zhou, B. Estimation of the ECMS Equivalent Factor Bounds for Hybrid Electric Vehicles. *IEEE Trans. Control Syst. Technol.* **2018**, *26*, 2198–2205, doi:10.1109/TCST.2017.2740836.

47. Sciarretta, A.; Back, M.; Guzzella, L. Optimal Control of Parallel Hybrid Electric Vehicles. *IEEE Trans. Control Syst. Technol.* **2004**, *12*, 352–363, doi:10.1109/TCST.2004.824312.

48. Musardo, C.; Rizzoni, G.; Guezennec, Y.; Staccia, B. A-ECMS: An Adaptive Algorithm for Hybrid Electric Vehicle Energy Management. *Eur. J. Control* **2005**, *11*, 509–524, doi:10.3166/ejc.11.509-524.

49. Rahmeh, H.; Bonfitto, A.; Ruzimov, S. Fuzzy Logic vs Equivalent Consumption Minimization Strategy for Energy Management in P2 Hybrid Electric Vehicles.; American Society of Mechanical Engineers Digital Collection, November 3 2020.

50. Zhou, B.; Rezaei, A.; Burl, J. Effect of Battery Temperature on Fuel Economy and Battery Ageing When Using the Equivalent Consumption Minimization Strategy for Hybrid Electric Vehicles.; April 14 2020; pp. 2020-01–1188.

51. Paganelli, G.; Delprat, S.; Guerra, T.M.; Rimaux, J.; Santin, J.J. Equivalent Consumption Minimization Strategy for Parallel Hybrid Powertrains. In Proceedings of the Vehicular Technology Conference. IEEE 55th Vehicular Technology Conference. VTC Spring 2002 (Cat. No.02CH37367); May 2002; Vol. 4, pp. 2076–2081 vol.4.

52. Xie, S.; Sun, F.; He, H.; Peng, J. Plug-In Hybrid Electric Bus Energy Management Based on Dynamic Programming. *Energy Procedia* **2016**, *C*, 378–383, doi:10.1016/j.egypro.2016.12.064.

53. Tribioli, L.; Cozzolino, R.; Chiappini, D.; Iora, P. Energy Management of a Plug-in Fuel Cell/Battery Hybrid Vehicle with on-Board Fuel Processing. *Appl. Energy* **2016**, *184*, 140–154.

54. Chen, Z.; Mi, C.C.; Xiong, R.; Xu, J.; You, C. Energy Management of a Power-Split Plug-in Hybrid Electric Vehicle Based on Genetic Algorithm and Quadratic Programming. *J. Power Sources* **2014**, *248*, 416–426, doi:10.1016/j.jpowsour.2013.09.085.

55. He, H.; Zhang, J.; Li, G. Model Predictive Control for Energy Management of a Plug-in Hybrid Electric Bus. *Energy Procedia* **2016**, *C*, 901–907, doi:10.1016/j.egypro.2016.06.109.

56. Borhan, H.; Vahidi, A.; Phillips, A.M.; Kuang, M.L.; Kolmanovsky, I.V.; Di Cairano, S. MPC-Based Energy Management of a Power-Split Hybrid Electric Vehicle. *IEEE Trans. Control Syst. Technol.* **2012**, *20*, 593–603, doi:10.1109/TCST.2011.2134852.

57. He, H.; Wang, Y.; Han, R.; Han, M.; Bai, Y.; Liu, Q. An Improved MPC-Based Energy Management Strategy for Hybrid Vehicles Using V2V and V2I Communications. *Energy* **2021**, *225*, 120273, doi:10.1016/j.energy.2021.120273.

58. Borhan, H.A.; Zhang, C.; Vahidi, A.; Phillips, A.M.; Kuang, M.L.; Di Cairano, S. Nonlinear Model Predictive Control for Power-Split Hybrid Electric Vehicles. In Proceedings of the 49th IEEE Conference on Decision and Control (CDC); December 2010; pp. 4890–4895.

59. Non-Linear Model Predictive Control of a Power-Split Hybrid Electric Vehicle Influence of Conclusion of Powertrain Dynamics Available online: https://www.esteco.com/modefrontier/non-linear-model-predictive-control-power-split-hybrid-electric-vehicle-influence-concl (accessed on 25 November 2021).

60. Dhar, A.; Bhasin, S. Adaptive MPC for Uncertain Discrete-Time LTI MIMO Systems with Incremental Input Constraints. *IFAC-Pap.* **2018**, *51*, 329–334, doi:10.1016/j.ifacol.2018.05.040.

61. Bujarbaruah, M.; Zhang, X.; Rosolia, U.; Borrelli, F. Adaptive MPC for Iterative Tasks. In Proceedings of the 2018 IEEE Conference on Decision and Control (CDC); December 2018; pp. 6322–6327.

62. Extreme Learning Machine: Theory and Applications - ScienceDirect Available online: https://www.sciencedirect.com/science/article/pii/S0925231206000385?via%3Dihub (accessed on 25 February 2022).

63. Huang, G.-B.; Zhu, Q.-Y.; Siew, C.-K. Extreme Learning Machine: A New Learning Scheme of Feedforward Neural Networks. In Proceedings of the 2004 IEEE International Joint Conference on Neural Networks (IEEE Cat. No.04CH37541); July 2004; Vol. 2, pp. 985–990 vol.2.

64. Ertugrul, Ö.F.; Kaya, Y. A Detailed Analysis on Extreme Learning Machine and Novel Approaches Based on ELM. *undefined* **2015**.

65. Extreme Learning Machine with a Deterministic Assignment of Hidden Weights in Two Parallel Layers - ScienceDirect Available online: https://www.sciencedirect.com/science/article/pii/S0925231216314412?via%3Dihub (accessed on 28 February 2022).

66. Extreme Learning Machine with Parallel Layer Perceptrons - ScienceDirect Available online:

https://www.sciencedirect.com/science/article/pii/S0925231215004622?via%3Dihub (accessed on 28 February 2022).

67. Li, G.; Zou, J. Multi-Parallel Extreme Learning Machine with Excitatory and Inhibitory Neurons for Regression. *Neural Process. Lett.* **2020**, *51*, 1579–1597, doi:10.1007/s11063-019-10160-3.

68. Qu, B.Y.; Lang, B.F.; Liang, J.J.; Qin, A.K.; Crisalle, O.D. Two-Hidden-Layer Extreme Learning Machine for Regression and Classification. *Neurocomputing* **2016**, *175*, 826–834, doi:10.1016/j.neucom.2015.11.009.

69. Krömer, P.; Platoš, J.; Snášel, V. Differential Evolution for the Optimization of Low-Discrepancy Generalized Halton Sequences. *Swarm Evol. Comput.* **2020**, *54*, 100649, doi:10.1016/j.swevo.2020.100649.

70. Prognostics Center of Excellence - Data Repository Available online: https://ti.arc.nasa.gov/tech/dash/groups/pcoe/prognostic-data-repository/ (accessed on 28 February 2022).

71. Murnane, M.; Ghazel, A. A Closer Look at State of Charge (SOC) and State of Health (SOH) Estimation Techniques for Batteries Available online: https://www.semanticscholar.org/paper/A-Closer-Look-at-State-of-Charge-(-SOC-)-and-State-Murnane-Ghazel/964c93c82bf2ee272c6491b3cb85a06529e935d2 (accessed on 28 February 2022).

72. Wang, W.; Wei, X.; Choi, D.; Lu, X.; Yang, G.; Sun, C. Chapter 1 - Electrochemical Cells for Medium- and Large-Scale Energy Storage: Fundamentals. In *Advances in Batteries for Medium and Large-Scale Energy Storage*; Menictas, C., Skyllas-Kazacos, M., Lim, T.M., Eds.; Woodhead Publishing Series in Energy; Woodhead Publishing: Sawston, UK, 2015; pp. 3–28 ISBN 978-1-78242-013-2.

73. Dahbi, M.; Komaba, S. Chapter 16 - Fluorine Chemistry for Negative Electrode in Sodium and Lithium Ion Batteries. In *Advanced Fluoride-Based Materials for Energy Conversion*; Nakajima, T., Groult, H., Eds.; Elsevier, 2015; pp. 387–414 ISBN 978-0-12-800679-5.

74. Youngdungpo-Gu, Y.-D. Specification for LG 18650 MJ1 Available online: https://www.nkon.nl/sk/k/Specification%20INR18650MJ1%2022.08.2014.pdf (accessed on 14 January 2022).

75. D6.7 – Battery Management System Standard. Available Online: Https://Everlasting-Project.Eu/Wp-Content/Uploads/2019/10/EVERLASTING_D6.7_final_20191001.Pdf (Accessed on 14 January 2022).

76. Sapna, S. Backpropagation Learning Algorithm Based on Levenberg Marquardt Algorithm. In Proceedings of the Computer Science & Information

Technology (CS & IT); Academy & Industry Research Collaboration Center (AIRCC): chennai, India, October 31 2012; pp. 393–398.

77. Khan, N.; Gaurav, D.; Kandl, T. Performance Evaluation of Levenberg-Marquardt Technique in Error Reduction for Diabetes Condition Classification. *Procedia Comput. Sci.* **2013**, *18*, 2629–2637, doi:10.1016/j.procs.2013.05.455.

78. Datasheet Specs for Panasonic Sanyo 18650 Battery Available online: https://www.orbtronic.com/content/Datasheet-specs-Sanyo-Panasonic-NCR18650GA-3500mah.pdf (accessed on 14 January 2022).

79. Ezemobi, E.; Tonoli, A.; Silvagni, M. Battery State of Health Estimation with Improved Generalization Using Parallel Layer Extreme Learning Machine. *Energies* **2021**, *14*, 2243, doi:10.3390/en14082243.

80. Specifications for NCR18650 GA Sanyo Lithium-Ion Battery Available online: https://www.hurt.com.pl/prods/bat/_li_ion/ncr18650ga.pdf (accessed on 5 January 2022).

81. Zhang, J.; Wang, P.; Liu, Y.; Cheng, Z. Variable-Order Equivalent Circuit Modeling and State of Charge Estimation of Lithium-Ion Battery Based on Electrochemical Impedance Spectroscopy. *Energies* **2021**, *14*, 769, doi:10.3390/en14030769.

82. Zhang, X.; Klein, R.; Subbaraman, A.; Chumakov, S.; Li, X.; Christensen, J.; Linder, C.; Kim, S.U. Evaluation of Convective Heat Transfer Coefficient and Specific Heat Capacity of a Lithium-Ion Battery Using Infrared Camera and Lumped Capacitance Method. *J. Power Sources* **2019**, *412*, 552–558, doi:10.1016/j.jpowsour.2018.11.064.

83. Ebrahimi, F.; Abedi, M. Design of a Robust Central Difference Kalman Filter in the Presence of Uncertainties and Unknown Measurement Errors. *Signal Process.* **2020**, *172*, 107533, doi:10.1016/j.sigpro.2020.107533.

84. Feng, K.; Li, J.; Zhang, D.; Wei, X.; Yin, J. Robust Central Difference Kalman Filter With Mixture Correntropy: A Case Study for Integrated Navigation. *IEEE Access* **2021**, *PP*, 1–1, doi:10.1109/ACCESS.2021.3083963.

85. Wipke, K.B.; Cuddy, M.R.; Burch, S.D. ADVISOR 2.1: A User-Friendly Advanced Powertrain Simulation Using a Combined Backward/Forward Approach. *IEEE Trans. Veh. Technol.* **1999**, *48*, 1751–1761, doi:10.1109/25.806767.

86. Energy Systems D3 2016 Mazda CX9 | Argonne National Laboratory Available online: https://www.anl.gov/es/energy-systems-d3-2016-mazda-cx9 (accessed on 5 January 2022).

87. US EPA, O. Combining Data into Complete Engine ALPHA Maps Available online: https://www.epa.gov/vehicle-and-fuel-emissions-testing/combining-data-complete-engine-alpha-maps (accessed on 5 January 2022).

88. Moradi, M.H. Predictive Control with Constraints, J.M. Maciejowski; Pearson Education Limited, Prentice Hall, London, 2002, Pp. IX+331, Price £35.99, ISBN 0-201-39823-0. *Int. J. Adapt. Control Signal Process.* **2003**, *17*, 261–262, doi:10.1002/acs.736.

89. Camacho, E.F. Constrained Control and Estimation: An Optimization Approach, G. C. Goodwin, M. M. Seron and J. A. de Dona, Springer, Berlin. No. of Pages: 411. ISBN: 1852335483. *Int. J. Robust Nonlinear Control* **2007**, *17*, 347–348, doi:10.1002/rnc.1151.

90. Falcone, P.; Borrelli, F.; Tseng, H.E.; Asgari, J.; Hrovat, D. Linear Time-Varying Model Predictive Control and Its Application to Active Steering Systems: Stability Analysis and Experimental Validation. *Int. J. Robust Nonlinear Control* **2008**, *18*, 862–875, doi:10.1002/rnc.1245.

91. Wan, Z.; Kothare, M.V. Efficient Scheduled Stabilizing Output Feedback Model Predictive Control for Constrained Nonlinear Systems. *IEEE Trans. Autom. Control* **2004**, *49*, 1172–1177, doi:10.1109/TAC.2004.831122.

92. Technical Guidelines for the Preparation of Applications for the Approval of Innovative Technologies Pursuant to Regulation (EC) No 443/2009 of The European Parliament and of the Council. European Commission, Brussels, February 2013 Available online: https://circabc.europa.eu/sd/a/a19b42c8-8e87-4b24-a78b-9b70760f82a9/July%202018%20Technical%20Guidelines.pdf (accessed on 5 January 2022).